ASTRONOMICAL INSTITUTE
SLOVAK ACADEMY OF SCIENCES

CONTRIBUTIONS OF THE ASTRONOMICAL OBSERVATORY SKALNATÉ PLESO

• VOLUME LVI •

Number 2

April 2026

Editorial Board

Editor-in-Chief
Augustín Skopal, *Tatranská Lomnica, The Slovak Republic*

Managing Editor
Richard Komžík, *Tatranská Lomnica, The Slovak Republic*

Editors
Július Koza, *Tatranská Lomnica, The Slovak Republic*
Aleš Kučera, *Tatranská Lomnica, The Slovak Republic*
Luboš Neslušan, *Tatranská Lomnica, The Slovak Republic*
Vladimír Porubčan, *Bratislava, The Slovak Republic*
Theodor Pribulla, *Tatranská Lomnica, The Slovak Republic*

Advisory Board
Bernhard Fleck, *Greenbelt, USA*
Arnold Hanslmeier, *Graz, Austria*
Marian Karlický, *Ondřejov, The Czech Republic*
Jan Vondrák, *Prague, The Czech Republic*

©
Astronomical Institute of the Slovak Academy of Sciences
2026

ISSN: 1336–0337 (on-line version)

CODEN: CAOPF8

Editorial Office: Astronomical Institute of the Slovak Academy of Sciences
SK - 059 60 Tatranská Lomnica, The Slovak Republic

CONTENTS

EDITORIAL

STARS

The Contributions of the Astronomical Observatory Skalnaté Pleso
are available in the full version
in the frame of ADS Abstract Service
and can be downloaded in a usual way from the URL address:

https://ui.adsabs.harvard.edu/

as well as from the website of
the Astronomical Institute of the Slovak Academy of Sciences
on the URL address:

https://www.astro.sk/caosp/caosp.php

The journal is covered/indexed by:

Web of Science (WoS)
WoS Core Collection: Science Citation Index Expanded

SCOPUS

Index Copernicus International

EDITORIAL

In the 55th edition of the journal Contributions of the Astronomical Observatory Skalnaté Pleso (CAOSP), four regular articles on 68 pages in the first issue, and 81 articles on 609 pages in two special issues were published in 2025. The publication of only one issue of regular articles were due to five submitted manuscripts not meeting the basic requirements for publication in our journal (mainly the corresponding level of scientific results and strict adherence to publication ethics). According to the *Journal Citation Reports* database, the articles published in 2024 received 164 citations.

Volume 55/1 published regular articles on various topics. The first article introduces the instrumentation of the new 50-cm multi-purpose telescope and its role in the Russian-Cuban global telescope network. The second article was devoted to the first light curve analysis for two detached eccentric eclipsing Algol-type binaries V869 Car and V2184 Sgr, using the PHOEBE code. In the third one, based on the kinematics of 1197 high-velocity stars utilizing LAMOST and Gaia DR3 archives within 100 kpc, the authors determined their kinematics parameters and calculated the corresponding Oort constants. The last paper deals with ultraviolet photometry of 105 galactic open clusters, which focuses on observing unstudied Galactic open clusters with the main aim of determining their reddening.

Volume 55/2 introduces 11 selected papers based on lectures presented in the International Meeting on Data for Atomic and Molecular Processes in Plasmas: "Astrophysical Spectroscopy: A&M DATA - Modelling". The conference was held from November 12 to 15, 2024, at a venue near Lake Palić, in northern Serbia. The meeting covered a wide range of topics, including various aspects of astrophysical spectroscopy, plasma physics, atomic and molecular data, databases, and Earth observation.

Volume 55/3 is dedicated to 70 papers presented at the international conference "Binary and Multiple Stars in the Era of Big Sky Surveys", which took place in the Czech historical town Litomyšl, during September 9–13, 2024. The conference focused on the lives of binary stars and multiple star systems, followed by modern instruments for large-scale surveys. The conference was the third of the specialized astrophysical conferences from 2004, 2014, and 2024, commemorating the legacy of the outstanding Czech astrophysicist, Zdeněk Kopal.

Tatranská Lomnica, February, 2026

Augustín Skopal, Editor-in-Chief

Richard Komžík, Managing Editor

Contrib. Astron. Obs. Skalnaté Pleso **56/2**, 7 – 35, (2026)
https://doi.org/10.31577/caosp.2026.56.2.7

Formation of Al II lines and photospheric aluminium abundances in B-type stars

Y. Takeda

11-2 Enomachi, Naka-ku, Hiroshima-shi, 730-0851, Japan (E-mail: ytakeda@js2.so-net.ne.jp)

Received: April 14, 2025; Accepted: May 7, 2025

Abstract. The aluminium abundances of early-to-late B-type main-sequence stars in the effective temperature range of $10000\,\mathrm{K} \lesssim T_{\rm eff} \lesssim 22000\,\mathrm{K}$ (comprising normal stars as well as chemically peculiar HgMn stars) were spectroscopically determined, with an aim of getting information about the galactic gas composition at the time of their formation from their photospheric abundances. For this purpose, two Al II lines at 6243 and 4663 Å were employed, for which the non-LTE effect was taken into account based on detailed statistical-equilibrium calculations. The non-LTE effect of these Al II lines generally acts in the direction of weakening (i.e., profile becomes shallower) caused by a decrease of line opacity (due to overionization) along with an enhanced line source function (overexcitation), and this effect tends to become progressively larger with an increase in $T_{\rm eff}$ as well as with a decrease in $\log g$ (surface gravity). Regarding the Al II 6243 line, while the non-LTE calculation qualitatively reproduces its overall behavior (e.g., transition from absorption to emission at early B-type), some $T_{\rm eff}$-dependent systematic trend remains unremoved in the non-LTE abundances of normal stars, which means that non-LTE corrections evaluated for this line are quantitatively insufficient. Meanwhile, for the case of the Al II 4663 line, which is more advantageous than the 6243 line in the sense that it is stronger without showing any emission, the resulting non-LTE abundances of ordinary B stars are almost constant at the solar abundance ($A \simeq 6.5$) over the wide $T_{\rm eff}$ range ($\sim$ 10000–20000 K), suggesting that the abundances derived from this line are successfully non-LTE-corrected and trustable. Therefore, according to the results from the Al II 4663 line, we may conclude that the Al abundance of the galactic gas in the recent past (several times $\sim 10^7$–10^8 yr ago) is almost consistent with the solar composition. As to the Al abundances of HgMn stars ($T_{\rm eff} \lesssim 15000\,\mathrm{K}$), our analysis confirmed that this element is conspicuously deficient (by $\sim$ 0.5–2 dex in comparison with the Sun) in the photosphere of these chemically peculiar stars, as already reported in previous studies.

Key words: line: formation – stars: abundances – stars: atmospheres – stars: chemically peculiar – stars: early-type

1. Introduction

Aluminium (Al; $Z = 13$) is one of the intermediate elements of astrophysical importance, which is considered to be synthesized mainly during the hydrostatic carbon and neon burning within massive stars and expelled outwards by type II supernovae explosion. While its chemical abundances have been rather well determined for a number of late-type (F–G–K) stars in a wide range of metallicity (e.g., Baumüller & Gehren (1997); Andrievsky et al. (2008); and the references therein), the situation is still insufficient in the field of early-type (A–B) stars. Unlike the case of cool solar-type stars where lines common to solar abundance determination may be used for deriving [Al/H] (differential abundance relative to the Sun), what matters more seriously in the case of hot stars is the reliability of absolute abundances which are not easy to establish precisely. Especially, since most of the previous studies have been done under the conventional assumption of LTE (Local Thermodynamic Equilibrium), an inadequacy of this presumption (neglect of the non-LTE effect) may be counted as a possible source of systematic error.

Given this situation, Takeda (2023) (hereinafter referred to as Paper I) tried to determine Al abundances of A-type stars ($7000\,\mathrm{K} \lesssim T_{\rm eff} \lesssim 10000\,\mathrm{K}$) based on the Al I 3944/3961 resonance lines by taking into account the non-LTE effect, because LTE abundances derived by past investigators were suspected to be considerably underestimated. It revealed in Paper I that this doublet suffers an appreciable non-LTE line-weakening and the serious zero-point discrepancy could be successfully removed ($[\mathrm{Al/H}] \sim 0$ for $[\mathrm{Fe/H}] \sim 0$ stars) by applying the significant (positive) non-LTE corrections amounting to up to $\lesssim 1\,\mathrm{dex}$.

As the follow-up of Paper I, the present study focuses on B-type stars ($10000\,\mathrm{K} \lesssim T_{\rm eff} \lesssim 22000\,\mathrm{K}$), but the intended scope is somewhat different. Most comparatively sharp-lined A-type stars (for which spectroscopic abundance determinations are feasible) more or less show some kind of chemical peculiarity (CP), and thus "normal" A stars are difficult to find in practice. In contrast, B-type main-sequence stars are divided rather clearly into non-CP (normal) stars and CP stars (mainly HgMn stars of late B-type), and we may expect the former "ordinary B stars" to retain the original gas at the time of star formation. Therefore, it may be possible to get the compositional information of the galactic gas in the recent past ($\sim 10^{7-8}\,\mathrm{yr}$ ago when these B-type stars of ~ 3–$9\,M_\odot$ were formed) from the the photospheric abundances of normal B stars.

However, Al abundance determinations of B-type stars seem to have been more focused on chemically peculiar HgMn stars because of their anomalous aspects, for which considerable Al-deficiency has been almost established (see the compilation of Ghazaryan & Alecian (2016)). Meanwhile, our understanding on the abundances of this element for normal B stars in comparison with the Sun (are they consistent with the solar abundance?) is still unsatisfactory, because published results (all derived with the assumption of LTE) tend to be diversified

depending upon the adopted lines (UV or optical; Al I or Al II or Al III), as summarized below (though this literature survey may not be complete).

- Al abundance determinations for the well-studied benchmark sharp-lined star ι Her (B3 IV) have been reported by several authors, as compiled by Golriz & Landstreet (2017) (cf. Table 1 therein). While most of them are around A[1]$\sim$ 6.5 and consistent with the solar abundance ($A_\odot$ = 6.47),[2] Pintado & Adelman (1993) derived an appreciably discrepant result (A = 5.97) from the Al II 4663 line (though they obtained a near-solar averaged abundance of $\langle A \rangle \sim 6.5$ from four Al III lines).

- Pintado & Adelman (1993) also determined the Al abundance of γ Peg (B2 IV) and found that both Al II and Al III lines yielded a consistent abundance of $\langle A \rangle \sim 6.0$–6.1 (subsolar by several tenths dex).

- In Allen (1998)'s abundance studies on early A and late B stars, attempts of Al abundance determinations for normal late B-type stars (21 Peg, ζ Dra, 21 Aql, τ Her) based on Al I 3944/3961 and Al II 4663 lines yielded $A \sim 6.3$–6.4 (almost solar or slightly subsolar), while five HgMn stars were confirmed to be considerably Al-deficient (by $\sim$ 1 dex or even more).

- Fossati et al. (2009) determined Al abundances of two normal late B-type stars (21 Peg and π Cet) and obtained [Al/H][3] $\sim$ 0 dex (almost solar) for both, though the abundance from Al III lines (measured only for π Cet) turned out appreciably higher by $\sim$ 0.4 dex.

- Niemczura et al. (2009) conducted an extensive abundance study on a number of late B-type stars (including chemically peculiar stars). Although distinction of normal and peculiar stars is not clear in their sample and the adopted lines are not explicitly described, the Al abundances they obtained range widely from $A \sim 5.1$ to ~ 6.8.

- The Al abundances of the B-type supergiant β Ori (B8 Iae) derived by Przybilla et al. (2006) show an appreciable discrepancy between Al II (6.14$\pm$0.08) and Al III (7.00 $\pm$ 0.38) lines.

- Monier (2022) carried out an Al abundance analysis for HD 209459 (whether it is normal or peculiar is still controversial) based on the Al II 4663 line in the optical region and the Al III 1854/1862 resonance lines in the ultraviolet

[1] A is the logarithmic number abundance of the element relative to that of hydrogen (H) with the usual normalization of A(H) = 12.

[2] In this article, Anders & Grevesse (1989)'s solar photospheric Al abundance of $A_\odot = 6.47$ is adopted as the reference, in order to keep consistency with Kurucz (1993)'s ATLAS9/WIDTH9 program. This is fairly close to values given in Asplund et al. (2009)'s Table 1 (6.45 $\pm$ 0.03 for the solar photosphere, 6.43 $\pm$ 0.01 for the meteorites).

[3] As usual, [X/H] is the differential abundance of element X relative to the Sun; i.e., [X/H] $\equiv A_{\rm star}$(X) $- A_\odot$(X).

region. He found that, while the the strength of the former optical line is consistent with the solar Al abundance, a significantly reduced Al abundance ($\sim$30% of the solar composition) is needed to reproduce the strength of the latter UV lines.

Recently, Takeda (2024) (hereinafter referred to as Paper II) determined the phosphorus abundances of B-type stars by using the P II 6043 line while taking into account the non-LTE effect, and found that the non-LTE P abundances of superficially normal early-to-late B-type stars (formed several times $\sim 10^7$–10^8 yr ago) are systematically lower than the abundance of the Sun (its age is $\sim 4.6\times10^9$ yr) by $\sim$0.2–0.3 dex. This is a significant conclusion, because it means that the galactic gas composition of P has decreased with time, in contradiction to the general concept of chemical evolution.

It is, therefore, worthwhile to examine how the abundances of Al (intermediate element similar to P) in normal B-type stars are compared with that of the Sun (near-solar as usually expected? or subsolar like the case of P?), since published determinations are too insufficient to answer this question as mentioned above.

This situation motivated the author to contend with the task of Al abundance determinations for the same sample of B-type stars as investigated in Paper II. This is the purpose of the present study. Towards this aim, special attention is paid to the following points in context of the unsatisfactory results of past publications.

– One of the reasons for the confusingly diversified literature results may be the mixed use of various kinds of Al lines for abundance determination. In order to make things simple, we restrict ourselves in this investigation to two Al II lines in the optical region at 6243 and 4663 Å, both of which are observable from early- through late-B stars of wide $T_{\rm eff}$ range and of sufficiently high quality (e.g., neither too strong nor too weak, almost free from blending).

– The non-LTE effect is taken into account in deriving the abundances from these Al II lines. This may be significant, because previous Al abundance determinations for B stars mentioned above were done under the assumption of LTE. Of course, there is no guarantee that computed non-LTE corrections are reliable, since statistical-equilibrium calculations may often be imperfect due to uncertainties in the adopted atomic model. Yet, the validity of the non-LTE calculation can be checked by examining whether the resulting non-LTE Al abundances of normal B-type stars do not show any systematic dependence upon $T_{\rm eff}$ (most important parameter), which actually makes a useful touchstone.

Table 1. Atomic data of important lines.

Species	Mult. No.	Transition	λ (Å)	$\chi_{\rm low}$ (eV)	$\log gf$ (dex)	Gammar (dex)	Gammas (dex)	Gammaw (dex)
Ti II	34	$a^2G_{9/2}$–$z^2G^o_{9/2}$	3900.539	1.131	−0.290	8.31	−6.49	−7.82
Al II	1	$^1P^o_1$–$^1D_2$	3900.675	7.421	−2.26*	9.22	(−5.95)	(−7.77)
Al II	2	$^1D_2$–$^1P^o_1$	4663.046	10.598	−0.284	7.99	(−5.53)	(−7.64)
Si II	–	$^2F^o_{7/2}$–$^2G_{7/2}$	6239.614	12.840	−1.359	8.59	−3.54	−7.25
		$^2F^o_{7/2}$–$^2G_{9/2}$	6239.614		+0.185			
		$^2F^o_{5/2}$–$^2G_{7/2}$	6239.665		+0.072			
Al II	10	$^3P^o_2$–$^3D_1$	6243.073	13.077	−1.250	(7.76)	−4.76	(−7.50)
		$^3P^o_2$–$^3D_2$	6243.203		−0.080			
		$^3P^o_2$–$^3D_3$	6243.367		+0.670			

All these data are taken from the VALD database (Ryabchikova et al., 2015), except for the $\log gf$ value of the Al II 3900.675 line, for which the NIST data was adopted instead (because the VALD value is likely to be unreliable; cf. Sect. 5.2.3). Note that the Al II 6243 line comprises three components belonging to the same multiplet. The data of the Ti II 3900.539 line (contaminating Al II 3900) and the Si II 6239 line (high-excitation line similar to Al II 6243) are also shown. After the first six self-explanatory columns, damping parameters are given in the last three columns, where the parenthesized values are calculated by Kurucz (1993)'s WIDTH9 program (by following the default treatment) because the data are not given in VALD:
Gammar is the radiation damping width (s^{-1}), $\log \gamma_{\rm rad}$.
Gammas is the Stark damping width (s^{-1}) per electron density (cm^{-3}) at 10^4 K, $\log(\gamma_{\rm e}/N_{\rm e})$.
Gammaw is the van der Waals damping width (s^{-1}) per hydrogen density (cm^{-3}) at 10^4 K, $\log(\gamma_{\rm w}/N_{\rm H})$.
*Taken from the NIST database.

2. Line-formation of Al II lines

2.1. Non-LTE calculations

Statistical-equilibrium calculations for Al II were carried out by using the model atom of 68 terms (up to $10p\,^3P^o$ at 146602 cm^{-1}) with 601 radiative transitions (cf. Sect. 2.1 in Paper I for more details). While the contribution of Al I was neglected because it is negligible in the atmosphere of B-type stars, that of Al III (32 terms) and Al IV (only the ground term) was taken into account in the number conservation of total Al atoms. As done in Paper I, the data of photoionization cross sections were taken from TOPbase (Cunto & Mendoza, 1992) for the lowest 10 Al II terms (while the hydrogenic approximation was applied for the remaining terms), and the collisional rates were evaluated by following the recipe described in Sect. 3.1.3 of Takeda (1991).

The non-LTE departure coefficients were calculated on a grid of 56 ($= 14 \times 4$) solar-metallicity model atmospheres resulting from combinations of fourteen $T_{\rm eff}$ values (9000, 10000, 11000, 12000, 13000, 14000, 15000, 16000, 17000, 18000, 19000, 20000, 22000, and 24000 K) and four $\log g$ values (3.0, 3.5, 4.0, and 4.5), while assuming $v_{\rm t} = 2\,{\rm km\,s^{-1}}$ (microturbulence) and the solar abundance of $A({\rm Al}) = 6.47$ ([Al/H] = 0) as the input Al abundance.[4]

[4]The effect of assigned Al abundance on departure coefficients is discussed in Sect. 5.1.

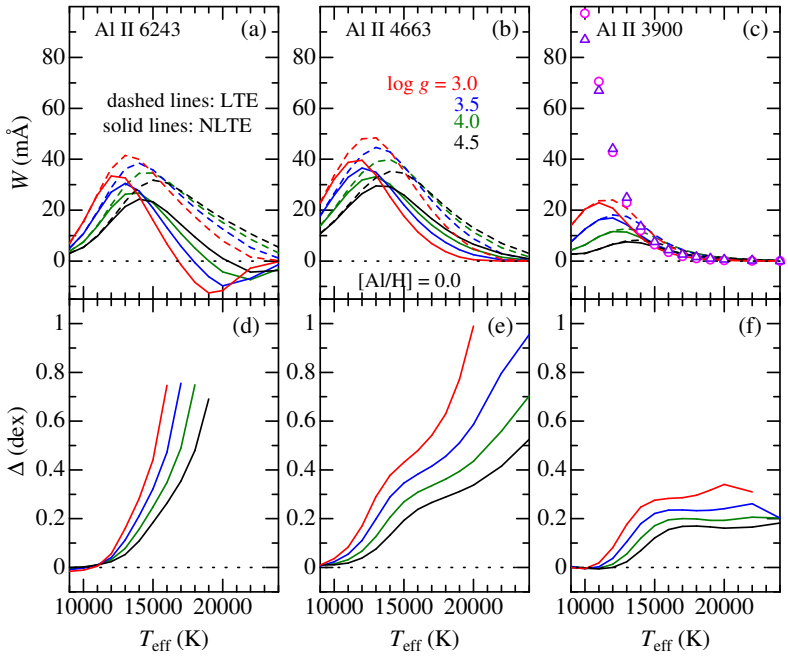

Figure 1. Non-LTE and LTE equivalent widths ($W^{\rm N}$ and $W^{\rm L}$ depicted in solid and dashed lines; upper panels (a)–(c)) and the corresponding non-LTE corrections (Δ; lower panels (d)–(f)), which were computed with the solar Al abundance on the non-LTE grid of models described in Sect 2.1, are plotted against $T_{\rm eff}$. Left ((a), (d)), center ((b), (e)), and right ((c), (f)) panels are for the Al II 6243, 4663, and 3900 lines, respectively. Results for different $\log g$ are distinguished by line colors (red, blue, green, black for 3.0, 3.5, 4.0, and 4.5). Note that Δ can not be calculated for the case of $W^{\rm N} \leq 0$ (because LTE abundance is unable to determine). In panel (c), the expected strengths of the Ti II 3900.539 line (contaminating the Al II 3900 line), which were calculated with the solar Ti abundance ($A_{\odot}$(Ti) = 4.99) for $\log g$ = 3.0 (pink open circles) and 4.0 (violet open triangles) models, are also plotted against $T_{\rm eff}$ for comparison.

2.2. Theoretical profiles and strengths of Al II lines

Now that the departure coefficients have been computed, the profile and strength of any line can be computed. Here, attention is paid to three representative Al II lines at 6243, 4663, and 3900 Å. The former two (6243 and 4663) are the lines used for abundance determination, while the latter 3900 line was originally considered as a candidate of abundance indicator but eventually abandoned (cf. Sect. 5.2.3). The atomic data of these lines are summarized in Table 1.

Fig. 1 illustrates how the theoretical equivalent widths of these lines calculated in LTE ($W^{\rm L}$; dashed line) as well as in non-LTE ($W^{\rm N}$; solid line) and

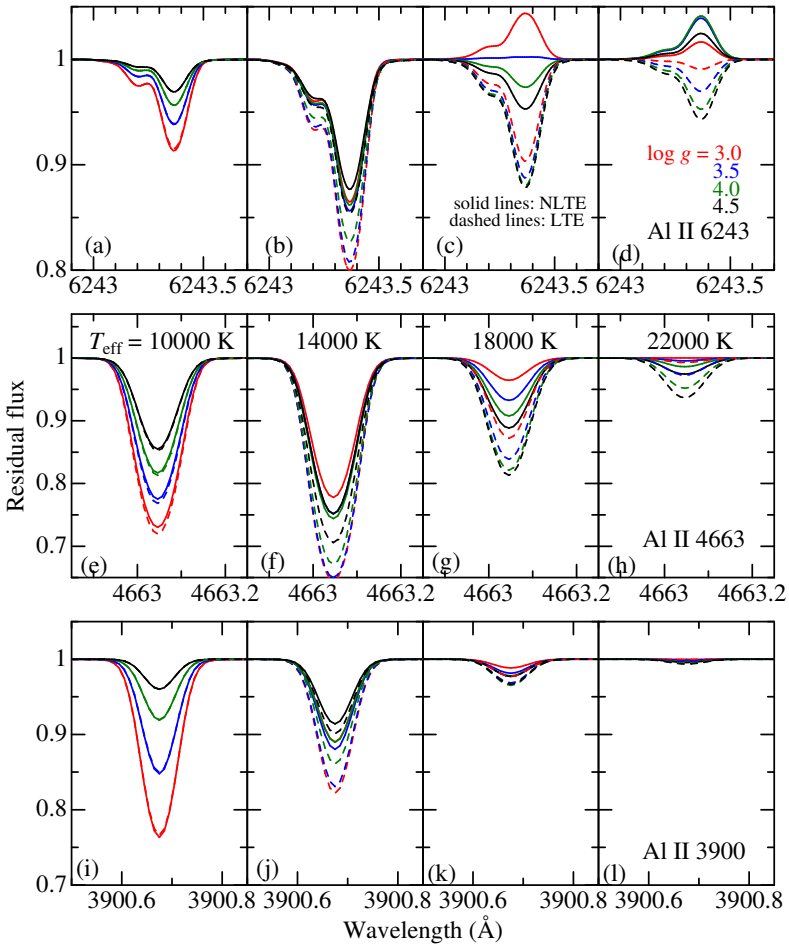

Figure 2. Theoretical line profiles computed for the Al II 6243 (top panels (a)–(d)), 4663 (middle panels (e)–(h)), and 3900 (bottom panels (i)–(l)) lines, each corresponding to $T_{\rm eff}$ = 10000 K, 14000 K, 18000 K, and 22000 K (from left to right). The same meanings of the line types and line colors as in Fig. 1.

the non-LTE corrections ($\Delta \equiv A^{\rm N} - A^{\rm L}$, where $A^{\rm L}$ and $A^{\rm N}$ are the abundances derived from $W^{\rm N}$ with LTE and non-LTE) depend upon $T_{\rm eff}$ and $\log g$. Likewise, the non-LTE and LTE profiles of these lines for the models of different $T_{\rm eff}$ values (10000, 14000, 18000, and 22000 K) are shown in Fig. 2.

The following characteristics are observed from these figures.

- The non-LTE effect acts as a line-weakening mechanism ($W^{\rm N} < W^{\rm L}$; Fig.1 and 2), which results in positive non-LTE corrections ($\Delta > 0$).

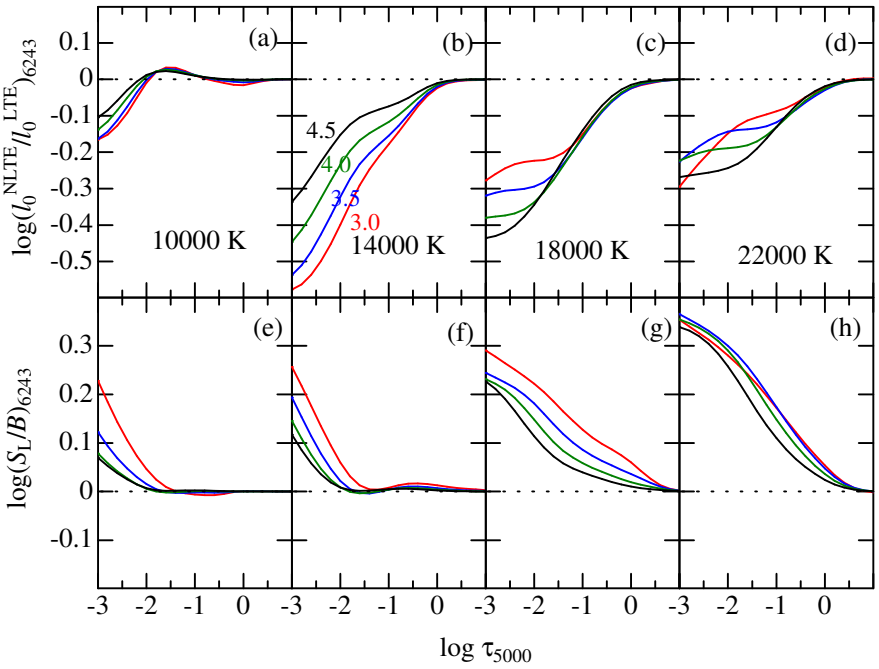

Figure 3. The non-LTE-to-LTE line-center opacity ratio (upper panels (a)–(d)) and the ratio of the line source function ($S_{\rm L}$) to the local Planck function (B) (lower panels (e)–(h)) for the Al II ^{3}P$^{\rm o}$–^{3}D transition (corresponding to Al II 6243) of multiplet 10, plotted against the continuum optical depth at 5000 Å. Shown here are the calculations done with $v_{\rm t} = 2\,{\rm km\,s^{-1}}$ and the solar Al abundance ([Al/H] = 0) for four representative $T_{\rm eff}$ values (from left to right): 10000 K (panels (a), (e)), 14000 K (panels (b), (f)), 18000 K (panels (c), (g)), and 22000 K (panels (d), (h)). The same meanings of the line colors as in Fig. 1.

- The non-LTE corrections (Δ) tend to increase towards higher $T_{\rm eff}$ and with a decrease in $\log g$ (Fig. 1).

- The overall behavior of W is qualitatively rather similar to each other with a peak around $T_{\rm eff} \sim 12000$–14000 K (though quantitatively $W_{3900} < W_{6243} < W_{4663}$).

- However, an emission feature emerges in the non-LTE profile of Al II 6243 line at $T_{\rm eff} \gtrsim 17000$ K (leading to $W^{\rm N}_{6243} < 0$), despite that the other two 4663 and 3900 lines retain ordinary absorption profiles.

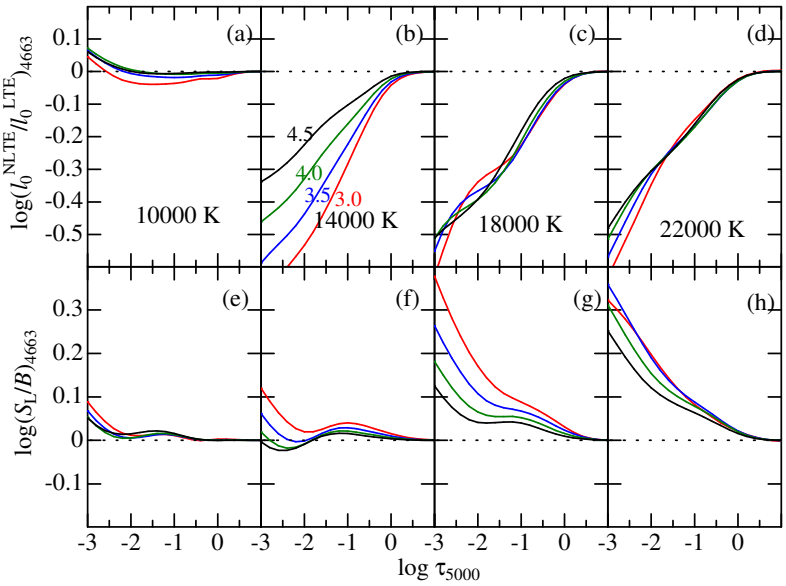

Figure 4. The non-LTE-to-LTE line-center opacity ratio and the ratio of the line source function ($S_{\rm L}$) to the local Planck function (B) for the Al II ^{1}D–^{1}P$^{\rm o}$ transition (corresponding to Al II 4663) of multiplet 2, plotted against the continuum optical depth at 5000 Å. Otherwise, the same as in Fig. 3.

2.3. Physical mechanism of the non-LTE effect

In order to understand the behaviors of the non-LTE effect described in Sect. 2.2, the non-LTE-to-LTE line-center opacity ratio $l_0^{\rm NLTE}/l_0^{\rm LTE}$ ($\simeq b_{\rm l}$) and the ratio of the line source function to the Planck function $S_{\rm L}/B$ ($\simeq b_{\rm u}/b_{\rm l}$,[5] where $b_{\rm l}$ and $b_{\rm u}$ are the departure coefficients of lower and upper levels) for the transitions relevant to Al II 6243, 4663, and 3900 lines are plotted against the optical depth in Fig. 3, 4, and 5, respectively.

We can see from these figures that $l_0^{\rm NLTE}/l_0^{\rm LTE} < 1$ (overionization) and $S_{\rm L}/B > 1$ (overexcitation) in the line-forming region. This explains why the strengths of these lines are generally decreased by the non-LTE effect in B-type stars ($W^{\rm N} < W^{\rm L}$), because both conditions act in the direction of weakening the absorption profile.

Especially, the latter effect ($S_{\rm L}/B > 1$) plays a comparatively more significant role in this line weakening, which becomes more conspicuous with an increase in $T_{\rm eff}$. Actually, the value of $S_{\rm L}/B$ in the line-forming region (e.g., at $\tau_{5000} \sim 0.1$) tends to be progressively larger towards higher $T_{\rm eff}$ (see pan-

[5]This relation holds under the condition that the photon energy $h\nu$ (h: Planck constant, ν: frequency) is not small in comparison with kT (k: Boltzmann constant). See also footnote 6.

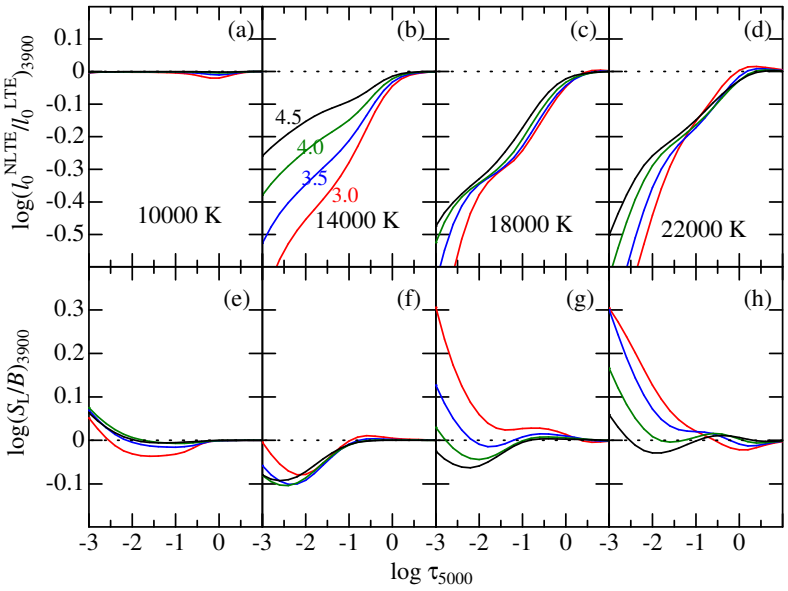

Figure 5. The non-LTE-to-LTE line-center opacity ratio and the ratio of the line source function ($S_{\rm L}$) to the local Planck function (B) for the Al II ^{1}P$^{\rm o}$–^{1}D transition (corresponding to Al II 3900) of multiplet 1, plotted against the continuum optical depth at 5000 Å. Otherwise, the same as in Fig. 3.

els (f)→(g)→(h) in Fig. 3 or Fig. 4), which eventually results in the trend of increasing Δ with $T_{\rm eff}$.

The cause of such an overexcitation ($S_{\rm L}/B > 1$) may be interpreted as that the lower level is more overionized than the upper level. Generally, overionization takes place when the photoionization rate ($\propto J_\lambda \sim W_{\rm D}B_\lambda(T_{\rm R})$) outweighs the recombination rate ($\propto B_\lambda(T_{\rm e})$) as $W_{\rm D}B_\lambda(T_{\rm R}) > B_\lambda(T_{\rm e})$, where $T_{\rm R}$ is the radiation temperature ($\simeq$ temperature of the continuum forming region), $W_{\rm D}$ is the dilution factor, and $T_{\rm e}$ is the electron temperature of the line-forming region. Since this inequality critically depends upon the T-sensitivity of B_λ, overionization is more enhanced at shorter wavelength regions (where B_λ is more sensitive to T). Accordingly, the fact that the wavelength of the photoionization edge for the lower level of a line is shorter than that for the upper level leads to $b_{\rm l} < b_{\rm u} (< 1)$; i.e., $S_{\rm L} > B$.

The appearance of an emission feature in the Al II 6243 line at the high $T_{\rm eff}$ range ($\gtrsim$ 17000 K) resulting from our non-LTE calculation (Fig. 2c and 2d) is also due to this effect of appreciably larger $S_{\rm L}$ over B, as recognized from Fig. 3g and 3h. The reason why this line shows an emission in the regime of early B-type may presumably be related to its longer wavelength than the other two, because the departure of $S_{\rm L}$ from B tends to be further enhanced in the Rayleigh–Jeans

region ($h\nu/kT < 1$).[6] It is worth noting that the Si II 6239.6 line (which is a similar high-excitation line with $\chi_{\rm low} \simeq 13\,{\rm eV}$ like Al II 6243; cf. Table 1) also shows an emission in early-to-mid B-type stars (see Sect. 4.3 and Fig. 6).

3. Observational data

3.1. Program stars

The target stars adopted in this investigation for Al abundance determinations are the same as in Paper II, which are 85 early-to-late B-type (near-)main-sequence stars (comprising normal as well as HgMn peculiar stars) in the solar neighborhood. They are comparatively sharp-lined ($v_{\rm e} \sin i \lesssim 60\,{\rm km\,s^{-1}}$) and have masses in the range of $2.5 M_\odot \lesssim M \lesssim 9 M_\odot$. The list of these 85 program stars is given in Table 2.

3.2. Adopted spectra

Since the sample stars in Paper II are targeted unchanged in this study, it is natural to use the same observational data (high-dispersion spectra obtained at Okayama Astrophysical Observatory) as adopted therein (see Sect. 2 in Paper II for the details). However, since the wavelength range covered by these spectra are limited to visible–red (or near-IR) region ($\lambda \gtrsim 5000$ Å), they can be employed only for the analysis of Al II 6243 line in the orange region.

Accordingly, blue-region spectra necessary for the analysis of Al II 4663 line (or Al II 3900 line) had to be obtained from the public-open data of stellar spectra. After searching the databases of ESO, CFHT, and ELODIE, spectra of 51 stars (out of 85 program stars) were found to be available and thus downloaded. The details of these data (file names, etc.) are summarized in Table 3.

Table 2. Program stars and the results of analysis.

No.	HD#	HR#	$T_{\rm eff}$	$\log g$	$v_{\rm e} \sin i$	W_{6243}	$A^{\rm N}_{6243}$	Δ_{6243}	W_{4663}	$A^{\rm N}_{4663}$	Δ_{4663}	Remark
(1)	(2)	(3)	(4)	(5)	(6)	(7)	(8)	(9)	(10)	(11)	(12)	(13)
1	029248	1463	22651	3.58	46	[0.0]	···	···	(no obs. data)			(ii)
2	000886	0039	21667	3.83	9	−7.0	···	···	3.9	6.92	0.58	(i)
3	035708	1810	21082	4.09	26	−13.2	···	···	5.6	6.77	0.47	(i)
4	035039	1765	20059	3.69	10	−8.7	···	···	(no obs. data)			(i)
5	042690	2205	19299	3.81	12	−8.3	···	···	6.0	6.53	0.45	(i)
6	032249	1617	18890	4.13	40	[0.0]	···	···	(no obs. data)			(ii)
7	034447	1731	18480	4.10	9	[0.0]	···	···	8.6	6.44	0.36	(ii)
8	196035	7862	17499	4.36	35	[0.0]	···	···	(no obs. data)			(ii)

[6] Let us define a parameter β ($\equiv 1 - b_{\rm l}/b_{\rm u}$) in order to indicate the degree of non-LTE overexcitation (i.e., difference between $b_{\rm l}$ and $b_{\rm u}$), by which $S_{\rm L}/B$ is expressed as $\simeq 1/(1-\beta)$ in the often encountered case of $h\nu/kT > 1$ (cf. footnote 5). However, in the high T and low ν case of $h\nu/kT < 1$, an alternative relation $S_{\rm L}/B \simeq 1/(1-\beta/\delta)$ holds, where $\delta \equiv h\nu/kT (< 1)$. That is, the extent of non-LTE departure (β) is further exaggerated by a factor of $1/\delta (> 1)$. See Sect. 12-4 in Mihalas (1978) for more details.

Table 2. (continued)

No.	HD#	HR#	$T_{\rm eff}$	$\log g$	$v_{\rm e}\sin i$	W_{6243}	$A^{\rm N}_{6243}$	Δ_{6243}	W_{4663}	$A^{\rm N}_{4663}$	Δ_{4663}	Remark
(1)	(2)	(3)	(4)	(5)	(6)	(7)	(8)	(9)	(10)	(11)	(12)	(13)
9	043157	2224	17486	4.12	37	1.6	5.64	0.49	14.7	6.55	0.34	
10	160762	6588	17440	3.91	7	1.1	5.57	0.58	12.9	6.52	0.36	
11	223229	9011	17327	4.20	31	[0.0]	···	···	(no obs. data)			(ii)
12	176502	7179	16821	3.89	8	7.2	6.25	0.48	(no obs. data)			
13	041753	2159	16761	3.90	28	[0.0]	···	···	(no obs. data)			(ii)
14	025558	1253	16707	4.29	41	3.4	5.74	0.33	16.6	6.45	0.28	
15	044700	2292	16551	4.21	5	5.3	5.94	0.34	15.6	6.41	0.29	
16	186660	7516	16494	3.57	9	4.3	6.05	0.53	(no obs. data)			
17	181858	7347	16384	4.19	17	7.0	6.05	0.33	15.8	6.40	0.29	
18	023793	1174	16264	4.15	46	6.8	6.02	0.32	(no obs. data)			
19	185330	7467	16167	3.77	4	[0.0]	···	···	1.3	5.23	0.31	(ii)
20	027396	1350	16028	3.91	15	7.3	6.05	0.34	(no obs. data)			
21	034798	1753	15943	4.27	37	8.8	6.07	0.27	20.6	6.49	0.27	
22	184171	7426	15858	3.54	27	4.6	5.89	0.40	(no obs. data)			
23	198820	7996	15852	3.86	32	9.7	6.18	0.34	22.6	6.60	0.34	
24	030122	1512	15765	3.72	15	[0.0]	···	···	(no obs. data)			(ii)
25	020756	1005	15705	4.43	18	7.7	5.96	0.23	(no obs. data)			
26	037971	1962	15532	3.63	9	2.5	5.51	0.33	11.6	6.18	0.33	
27	026739	1312	15490	3.92	31	10.8	6.15	0.29	22.3	6.51	0.31	
28	209008	8385	15353	3.50	20	7.0	5.98	0.34	20.5	6.51	0.37	
29	028375	1415	15278	4.30	19	14.7	6.25	0.22	24.0	6.49	0.24	
30	011415	0542	15174	3.54	42	10.9	6.16	0.32	22.0	6.52	0.35	
31	147394	6092	14898	4.01	30	13.0	6.15	0.22	(no obs. data)			
32	019268	0930	14866	4.24	17	12.8	6.13	0.19	(no obs. data)			
33	189944	7656	14793	4.01	35	14.8	6.21	0.22	27.0	6.53	0.27	
34	181558	7339	14721	4.15	14	13.6	6.15	0.19	22.7	6.38	0.22	
35	224990	9091	14569	3.99	35	5.0	5.64	0.19	14.4	6.09	0.22	
36	175156	7119	14561	2.79	12	8.9	6.10	0.38	26.7	6.76	0.49	
37	199578	8022	14480	4.02	27	16.2	6.23	0.19	(no obs. data)			
38	209419	8403	14404	3.82	16	16.0	6.21	0.21	(no obs. data)			
39	202753	8141	14318	3.84	40	9.6	5.93	0.19	21.7	6.32	0.24	
40	023300	1141	14207	3.84	19	16.3	6.20	0.19	(no obs. data)			
41	182255	7358	14190	4.29	28	12.4	6.08	0.13	28.1	6.48	0.18	
42	041692	2154	14157	3.19	28	16.1	6.22	0.26	27.5	6.55	0.37	
43	049606	2519	14121	3.82	19	(<1.7)	(<5.1)	0.16	0.7	4.62	0.20	(iii)
44	212986	8554	14121	4.27	20	13.9	6.14	0.13	(no obs. data)			
45	016219	0760	14113	4.06	23	17.1	6.23	0.15	(no obs. data)			
46	188892	7613	14008	3.38	30	13.7	6.09	0.22	(no obs. data)			
47	206540	8292	13981	4.01	13	15.7	6.18	0.15	27.3	6.43	0.21	
48	191243	7699	13923	2.50	28	[0.0]	···	···	(no obs. data)			(ii)
49	210424	8452	13740	3.99	12	14.1	6.11	0.13	28.3	6.44	0.19	
50	201888	8109	13689	4.01	5	15.6	6.16	0.12	(no obs. data)			
51	011857	0561	13600	3.88	20	17.3	6.21	0.13	(no obs. data)			
52	053244	2657	13467	3.42	36	(<2.2)	(<5.2)	0.15	2.4	5.09	0.21	(iii)
53	155763	6396	13397	4.24	41	21.8	6.40	0.09	34.3	6.59	0.14	
54	173117	7035	13267	3.63	22	12.7	6.00	0.12	23.3	6.24	0.19	
55	017081	0811	13063	3.72	20	19.6	6.26	0.10	33.8	6.52	0.18	
56	023408	1149	12917	3.36	30	(<1.7)	(<5.0)	0.11	5.5	5.41	0.18	(iii)
57	196426	7878	12899	3.89	6	13.8	6.10	0.08	30.3	6.43	0.14	
58	179761	7287	12895	3.46	16	17.8	6.16	0.11	30.4	6.40	0.19	
59	011529	0548	12858	3.43	30	20.2	6.23	0.10	(no obs. data)			

Table 2. (continued)

No.	HD#	HR#	$T_{\rm eff}$	$\log g$	$v_{\rm e}\sin i$	W_{6243}	$A^{\rm N}_{6243}$	Δ_{6243}	W_{4663}	$A^{\rm N}_{4663}$	Δ_{4663}	Remark
(1)	(2)	(3)	(4)	(5)	(6)	(7)	(8)	(9)	(10)	(11)	(12)	(13)
60	178065	7245	12243	3.49	4	(< 0.6)	(< 4.6)	0.06	0.8	4.49	0.10	(iii)
61	038899	2010	10774	4.02	26	10.7	6.43	0.01	24.3	6.49	0.03	
62	043247	2229	10301	2.39	33	4.3	5.45	0.00	15.2	5.75	0.06	
63	209459	8404	10204	3.53	3	7.7	6.25	0.00	23.4	6.41	0.03	
64	181470	7338	10085	3.92	2	6.3	6.34	0.00	(no obs. data)			
65	098664	4386	10194	3.75	62	(< 5.0)	(< 6.1)	0.00	24.5	6.53	0.03	(iii)
66	130557	5522	10142	3.85	55	(< 6.2)	(< 6.3)	0.00	16.6	6.29	0.02	(iii)
67	079158	3652	13535	3.72	46	8.1	5.79	0.13	(no obs. data)			
68	106625	4662	11902	3.36	37	(< 1.3)	(< 4.9)	0.05	(no obs. data)			(iii)
69	150100	6184	10542	3.84	36	(< 3.1)	(< 5.8)	0.01	8.9	5.82	0.02	(iii)
70	197392	7926	13166	3.46	30	19.0	6.20	0.13	(no obs. data)			
71	198667	7985	11125	3.42	26	14.2	6.25	0.01	(no obs. data)			
72	202671	8137	13566	3.36	25	(< 3.5)	(< 5.4)	0.17	3.8	5.32	0.23	(iii)
73	193432	7773	10180	3.91	24	5.9	6.27	0.00	22.7	6.53	0.02	
74	161701	6620	12692	4.04	20	13.6	6.15	0.06	(no obs. data)			
75	077350	3595	10141	3.68	20	4.9	6.10	0.00	18.7	6.31	0.02	
76	129174	5475	12929	4.02	16	(< 1.5)	(< 5.1)	0.07	(no obs. data)			(iii)
77	201433	8094	12193	4.24	15	17.9	6.44	0.04	(no obs. data)			
78	144206	5982	11925	3.79	12	(< 0.8)	(< 4.8)	0.04	3.2	5.16	0.06	(iii)
79	145389	6023	11714	4.02	11	(< 0.9)	(< 5.0)	0.03	7.9	5.66	0.05	(iii)
80	190229	7664	13102	3.46	10	(< 1.1)	(< 4.8)	0.12	1.5	4.84	0.17	(iii)
81	149121	6158	10748	3.89	10	(< 1.0)	(< 5.2)	0.01	0.7	4.60	0.02	(iii)
82	078316	3623	13513	3.85	8	(< 0.9)	(< 4.8)	0.11	0.5	4.40	0.15	(iii)
83	089822	4072	10307	3.89	5	(< 0.4)	(< 5.0)	0.00	1.7	5.07	0.02	(iii)
84	143807	5971	10828	4.06	4	3.3	5.82	0.01	9.0	5.85	0.02	
85	193452	7775	10543	4.15	3	2.9	5.89	0.01	(no obs. data)			

(1) Star number (tentatively assigned). (2) Henry Draper Catalogue number. (3) Bright Star Catalogue number. (4) Effective temperature (in K). (5) Logarithmic surface gravity (in $\mathrm{cm\,s^{-2}}$/dex). (6) Projected rotational velocity (in $\mathrm{km\,s^{-1}}$). (7) Equivalent width of Al II 6243 line (in mÅ). (8) Non-LTE Al abundance derived from Al II 6243 (in dex). (9) Non-LTE correction for Al II 6243 (in dex). (10) Equivalent width of Al II 4663 line (in mÅ). (11) Non-LTE Al abundance derived from Al II 4663 (in dex). (12) Non-LTE correction for Al II 4663 (in dex). (13) Remarks for the unmeasurable cases of Al II 6243.
Since this table is so arranged as to be consistent with Table 1 of Paper II (which should be consulted for more details of the program stars), the first part (#1–#64) present the data of 64 early-to-late B stars (in the descending order of $T_{\rm eff}$) followed by the second part (#65–#85) for 21 late B-type stars (in the descending order of $v_{\rm e}\sin i$). Column (13) indicates the cases where Al abundances could not be established from the Al II 6243 line, which are divided into three types (cf. Sect. 4.3 and 4.4): (i) Line profiles show an appreciable emission feature (early-to-mid B-type stars). (ii) Lines are too weak because of filled-in emissions (early-to-mid B-type stars). (iii) Lines are too weak but considered to be due to very low Al abundance (late B-type HgMn stars).

Table 3. Public-open data additionally employed in this study.

Star No.	HD#	*Data/Instrument	File name	Remark
2	000886	ELODIE	elodie_19981123_0019.fits	
3	035708	CFHT/ESPaDOnS	1288837i.fits-1288844i.fits	8 files co-added
5	042690	ESO/FERROS	ADP.2016-09-27T09_50_43.972.fits	
7	034447	ESO/XSHOOTER	ADP.2017-08-11T08_26_08.731.fits	
9	043157	ESO/XSHOOTER	ADP.2017-08-10T15_20_15.958.fits	$R = 3250$
10	160762	CFHT/ESPaDOnS	1216549i.fits-1216568i.fits	20 files co-added
14	025558	CFHT/ESPaDOnS	1977059i.fits-1977070i.fits	12 files co-added
15	044700	ESO/XSHOOTER	ADP.2017-08-11T21_07_09.955.fits	
17	181858	ESO/XSHOOTER	ADP.2017-08-18T07_38_30.899.fits	$R = 5400$
19	185330	CFHT/ESPaDOnS	1266787i.fits-1266790i.fits	4 files co-added
21	034798	ESO/FERROS	ADP.2016-09-27T09_50_43.812.fits	
23	198820	ELODIE	elodie_20041110_0019.fits	
26	037971	ELODIE	elodie_20030113_0020.fits	
27	026739	ESO/FERROS	ADP.2016-09-23T06_51_12.898.fits	
28	209008	ESO/UVES	ADP.2020-07-20T14_03_10.973.fits	
29	028375	ESO/XSHOOTER	ADP.2017-08-11T22_53_23.592.fits	$R = 5400$
30	011415	CFHT/ESPaDOnS	1168487i.fits-1168490i.fits	4 files co-added
33	189944	ESO/XSHOOTER	ADP.2017-08-11T18_51_15.004.fits	
34	181558	ESO/HARPS	ADP.2014-09-17T11_21_34.070.fits	
35	224990	ESO/FERROS	ADP.2016-09-27T09_50_42.585.fits	
36	175156	ESO/UVES	ADP.2020-06-30T13_28_27.894.fits	
39	202753	ESO/HARPS	ADP.2014-09-23T11_05_18.230.fits	
41	182255	ELODIE	elodie_20031106_0018.fits	
42	041692	ESO/HARPS	ADP.2016-09-05T01_02_13.863.fits	
43	049606	CFHT/ESPaDOnS	2787264i.fits-2787267i.fits	4 files co-added
47	206540	ESO/XSHOOTER	ADP.2017-08-11T04_40_12.486.fits	
49	210424	ESO/UVES	ADP.2021-09-01T05_49_03.769.fits	
52	053244	ESO/FERROS	ADP.2016-09-21T07_46_52.316.fits	
53	155763	ELODIE	elodie_20010809_0017.fits	
54	173117	ESO/XSHOOTER	ADP.2018-09-13T17_16_55.500.fits	$R = 5400$
55	017081	ESO/UVES	ADP.2020-07-10T21_52_27.364.fits	
56	023408	ESO/FERROS	ADP.2016-09-27T09_50_43.630.fits	
57	196426	ESO/UVES	ADP.2020-08-04T20_45_41.082.fits	
58	179761	ESO/UVES	ADP.2020-08-04T15_46_04.184.fits	
60	178065	ESO/UVES	ADP.2020-08-14T10_13_40.490.fits	
61	038899	ESO/HARPS	ADP.2016-09-04T01_02_02.711.fits	
62	043247	ESO/FERROS	ADP.2016-09-27T09_50_43.636.fits	
63	209459	CFHT/ESPaDOnS	1649409i.fits-1649412i.fits	4 files co-added
65	098664	ESO/FERROS	ADP.2016-09-27T09_50_43.696.fits	
66	130557	ESO/UVES	ADP.2020-06-09T07_11_28.785.fits	
69	150100	ELODIE	elodie_19980704_0017.fits	
72	202671	ESO/FERROS	ADP.2016-09-27T09_50_43.826.fits	
73	193432	ESO/UVES	ADP.2020-08-14T10_35_52.467.fits	
75	077350	ELODIE	elodie_20050203_0013.fits	
78	144206	ELODIE	elodie_20000818_0006.fits	
79	145389	ELODIE	elodie_20040512_0019.fits	
80	190229	CFHT/ESPaDOnS	2770404i.fits-2770407i.fits	4 files co-added
81	149121	ESO/UVES	ADP.2020-06-12T15_23_23.451.fits	
82	078316	ESO/FERROS	ADP.2016-09-27T07_02_43.215.fits	
83	089822	CFHT/ESPaDOnS	2948464i.fits-2948467i.fits	4 files co-added
84	143807	ELODIE	elodie_20040510_0015.fits	

These are the data adopted for the analysis of the Al II 4663 line (also for checking the Al II 3900 line in HD 160762, HD 209008, and HD 209459; cf. Sect. 5.2.3). Although most of these spectra are of sufficiently high resolving power ($R \gtrsim 10000$), some are of medium spectral resolution (R is only several thousands) as remarked in the last column.
ESO $\cdots$ ESO Science Archive Facility (`https://archive.eso.org/cms.html`).
CFHT $\cdots$ Canada-France-Hawaii Telescope; data available from the Canadian Astronomy Data Centre (`https://www.cadc.hia.nrc.gc.ca/`).
ELODIE $\cdots$ The ELODIE Archive (`https://atlas.obs-hp.fr/elodie/`).

4. Abundance determination

4.1. Procedures

The abundances of Al for the program stars are determined by almost the same procedures as adopted in Paper I or Paper II, which consist of four steps. (1) First, the spectrum-fitting analysis is applied to two spectral regions comprising Al II 6243 and Al II 4663 lines, and the best fit parameter solutions are determined. (2) Based on such established abundance solutions, the equivalent widths of these two Al lines (W) are inversely calculated. (3) Then the non-LTE abundance ($A^{\rm N}$) is derived from W by taking into account the non-LTE effect. (4) Finally, uncertainties in the abundance results are estimated, while considering the errors in W along with the sensitivities to parameter changes.

4.2. Atmospheric parameters

Regarding the atmospheric parameters assigned to each star, the same values as used in Paper II (see Sect. 3 therein for the details) are adopted in this study. In Table 1 are shown the values of $T_{\rm eff}$ and $\log g$, which were originally determined from colors of the Strömgren system. As to the microturbulence, $v_{\rm t} = 1\,{\rm km\,s^{-1}}$ ($T_{\rm eff} < 16500\,{\rm K}$) and $2\,{\rm km\,s^{-1}}$ ($T_{\rm eff} > 16500\,{\rm K}$) are tentatively assumed as done in Paper II, which is sufficient because this parameter is practically insignificant in the present case (cf. Sect. 4.5). Likewise, the model atmospheres for each of the targets are the solar-metallicity models generated by interpolating Kurucz (1993)'s ATLAS9 model grid in terms of $T_{\rm eff}$ and $\log g$.

4.3. Synthetic spectrum fitting

The spectrum-fitting analysis (Takeda, 1995) by assuming LTE was applied to two wavelength regions (6230–6250 Å and 4656–4668 Å, each comprising Al II 6243 and 4663, respectively), in order to accomplish the best fit between theoretical and observed spectra. Here, the parameters varied are the chemical abundances (of Al and other elements showing appreciable lines), rotational broadening velocity ($v_{\rm e} \sin i$), and radial velocity ($V_{\rm rad}$). The data of all atomic lines (including those of Al lines given in Table 1) in each region were taken from the VALD database (Ryabchikova et al., 2015).

It then revealed that, while Al abundances could be successfully established for all 51 stars in the fitting analysis of the 4656–4668 Å region, its determination had to be abandoned for 29 stars (out of 85 stars) in the 6230–6250 Å region analysis since the Al II 6243 line did not exhibit any detectable absorption profile. This is due to the fact that this line begins to show an emission feature in the high $T_{\rm eff}$ regime of early-to-mid B-type stars, which is actually predicted in the non-LTE calculations (cf. Fig. 2c and 2d). In order to illustrate this situation, the spectral portions in the neighborhood of the Al II 6243 and 4663 lines for stars with $T_{\rm eff} \gtrsim 16000\,{\rm K}$ are displayed in Fig. 6, where we can see that the Al II

6243 line is not usable for a large fraction of stars at $T_{\rm eff} \gtrsim 17000$ K (because of being emission or very weak due to filled-in emission). Meanwhile, this 6243 line is too weak to be measurable in chemically peculiar HgMn stars (mostly late B-type) because Al is considerably deficient in their atmospheres.

Accordingly, those 29 stars for which Al abundance could not be derived from the 6243 line are divided into three categories: (i) emission line (early- or mid-B stars), (ii) very weak line due to the effect of filled-in emission (mid-B stars), and (iii) very weak line due to considerable Al-deficiency (late-B HgMn stars), as indicated in column 13 of Table 2. In such cases, the fitting was tentatively done either by masking the 6243 line region or by fixing the Al abundance at an arbitrary value. The cases (ii) and (iii) can be clearly distinguished from each other by checking the neighboring Si II 6239.6 line, because this Si II line also shows an emission (or filled-in emission) in the former case (ii), while not in the latter case (iii).

The comparison of theoretical spectrum (for the solutions with converged parameters) with the observed spectrum (for the selected wavelength region in the neighborhood of the relevant Al lines) is shown in Fig. 7 (6243 line region) and Fig. 8 (4663 line region) for each star.

4.4. Evaluation of equivalent widths

Next, the equivalent widths (W_{6243} and W_{4663}) of the Al II 6243 and 4663 lines were inversely evaluated from the Al abundance solution derived from the spectrum-fitting analysis (cf. Sect. 4.3) with the same model and atmospheric parameters, where Kurucz (1993)'s WIDTH9 program[7] was employed for this purpose. The errors involved in such obtained W values (δW) were further estimated from the line-center depth and the S/N ratio by applying Eq. (1) in Paper II, which are typically on the order of $\lesssim$1–2 mÅ in most cases (though up to several mÅ or more in exceptionally shallow/broad-line cases)

The resulting W_{6243} and W_{4663} for each star are presented in Table 2. Regarding 29 stars for which abundances could not be determined from the 6243 line (cf. Sect. 4.3), following values are assigned to W_{6243} in this table for each of the three cases (i, ii, iii). (i) W_{6243} (negative) was directly measured from the emission-line profile by the Gaussian fitting. (ii) Zero value (0) is tentatively given. (iii) An upper-limit value ($W^{\rm ul}_{6243}$) is presented, which was estimated from the line width and the S/N ratio by using Eq. (1) of Takeda (2025).

4.5. Non-LTE abundances and their uncertainties

Then, the non-LTE abundances ($A^{\rm N}_{6243}$ and $A^{\rm N}_{4663}$) were determined from W_{6243} and W_{4663} for each star by taking into account the departure from LTE, where

[7]The original WIDTH9 program was considerably modified by the author in various respects; for example, enabling the treatment of multi-component lines (such as the Al II 6243 line), inclusion of the non-LTE effect, etc.

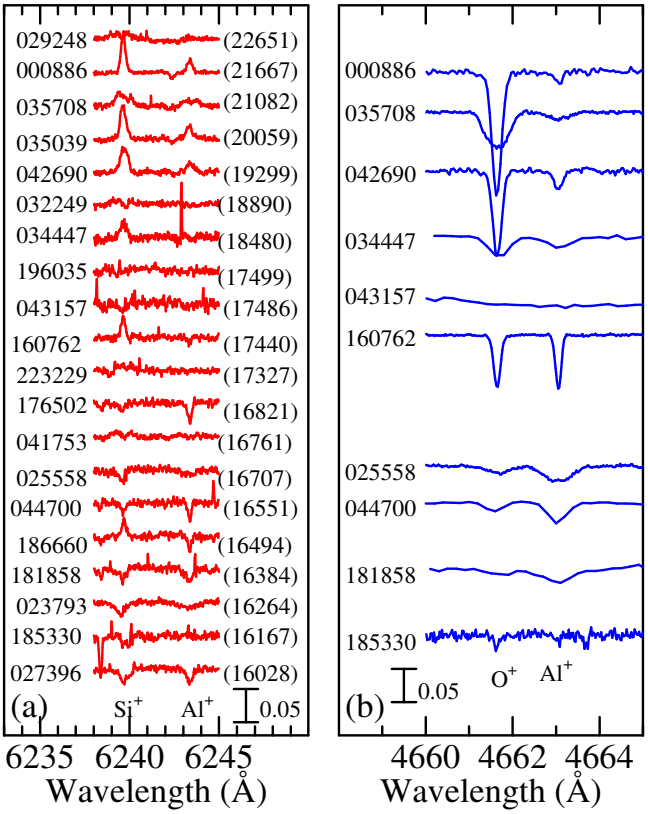

Figure 6. Observed spectra of the early-to-mid B-type stars with $T_{\rm eff} \gtrsim 16000\,{\rm K}$ in the neighborhood of (a) Al II 6243 line and (b) Al II 4663 line, which are designated by the HD number on the left and arranged in the descending order of $T_{\rm eff}$ (indicated by parenthesized values). Note that the Al II 6243 line (along with the neighboring Si II 6239 line) shows an emission or a very weak strength due to filled-in emission at $T_{\rm eff} \gtrsim 17000\,{\rm K}$, whereas the Al II 4663 line ever keeps an absorption profile.

the departure coefficients calculated on the grid of 56 models (cf. Sect. 2.1) were interpolated in terms of $T_{\rm eff}$ and $\log g$, from which the non-LTE corrections (Δ; difference of $A^{\rm N}$ from the LTE abundance $A^{\rm L}$) were also obtained. The resulting values of W, $A^{\rm N}$, and Δ for each line are given in Table 2. Likewise, W, $A^{\rm L}$, Δ and $A^{\rm N}$ are plotted against $T_{\rm eff}$ in panels ((a)–(d)) of Fig. 9 (6243) and Fig. 10 (4663), where the error bars attached in W (panel (a)) are $\pm\delta W$ (Sect. 4.4)

The abundance sensitivities to typical ambiguities in atmospheric parameters [$\delta_{T\pm}$ (abundance changes for $T_{\rm eff}$ perturbations by $\pm 3\%$), $\delta_{g\pm}$ (abundance changes for $\log g$ perturbations by $\pm 0.2\,{\rm dex}$), and $\delta_{v\pm}$ (abundance changes for $v_{\rm t}$

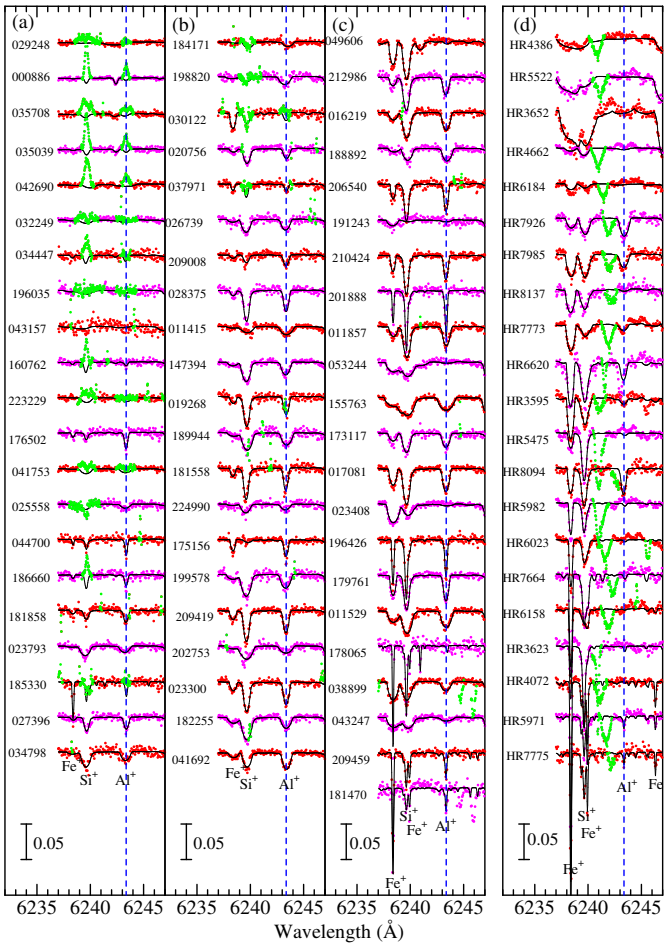

Figure 7. Synthetic spectrum-fitting in the neighborhood of the Al II 6243 line done for each of the 85 program stars. Shown here is the selected wavelength region of 6237–6247 Å. The best-fit theoretical spectra are depicted by black solid lines, while the observed data are plotted by colored dots (outlier data points rejected in calculating χ^2 are highlighted in light green). The spectra are arranged in the same manner as Fig. 3 of Paper II to keep consistency with that paper: Panels (a), (b), and (c) are for the 64 early-to-late B stars (indicated by the HD number) in the descending order of $T_{\rm eff}$ (from top to bottom; from left to right). while the rightmost panel (d) is for 21 late-B stars (indicated by the HR number) in the descending order of $v_{\rm e} \sin i$. An offset of 0.05 (in unit of the continuum) is applied to each spectrum relative to the adjacent one. The position of 6243.367 Å (wavelength of the strongest component of Al II 6243 triplet) is shown by the vertical dashed line. The wavelength scale is in the laboratory frame after correcting the radial velocity shift.

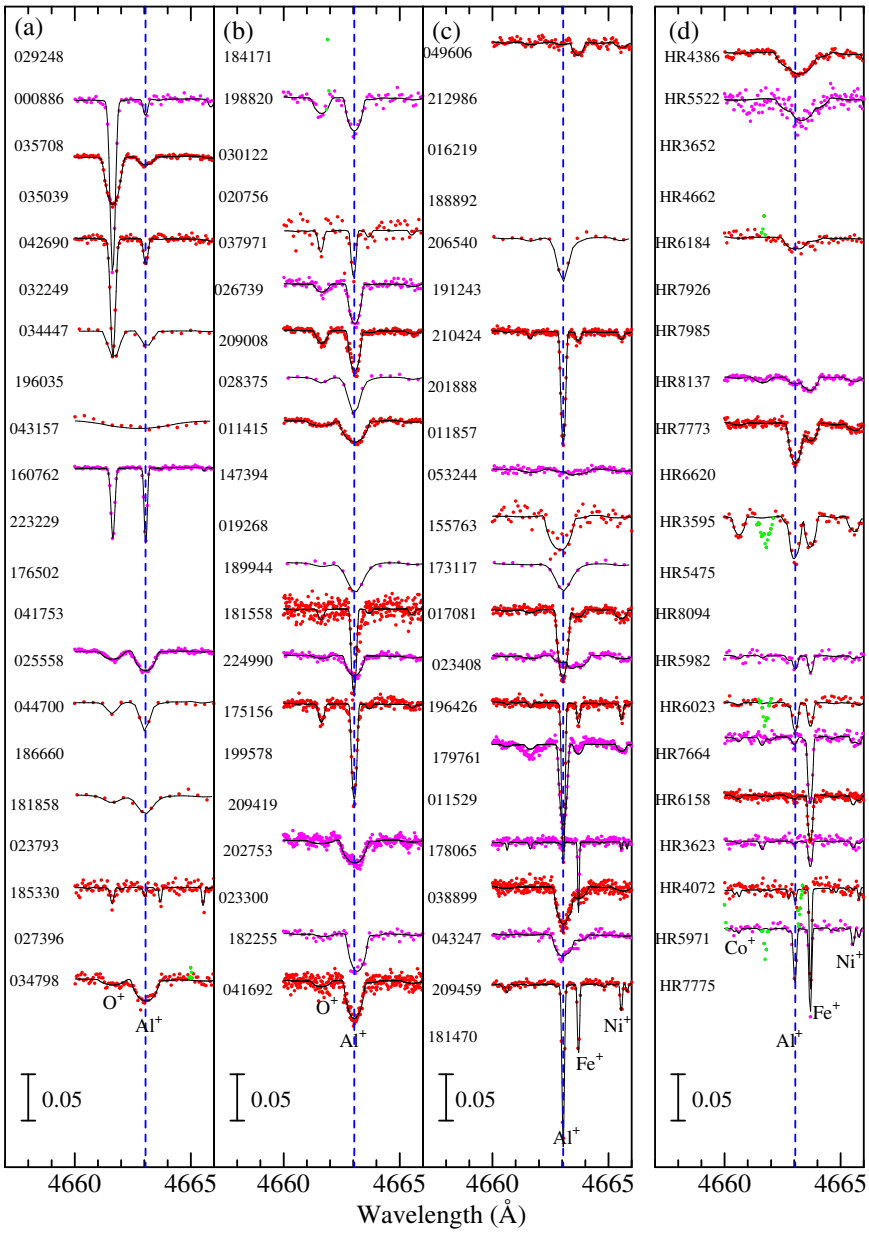

Figure 8. Synthetic spectrum-fitting in the neighborhood of the Al II 4663 line done for 51 stars, for which public-open data are available (cf. Table 3). Shown here is the selected wavelength region of 4660–4666 Å. The position of 4663.046 Å (wavelength of the Al II 4663 line) is shown by the vertical dashed line. Otherwise, the same as in Fig. 7.

perturbations by $\pm 1\,\mathrm{km\,s^{-1}}$)] are plotted against $T_{\rm eff}$ in panels (e)–(g) of Fig. 9 and Fig. 10. We can see from these figures that combined impacts of parameter uncertainties upon the abundances (due mainly to $T_{\rm eff}$ and partly to $\log g$, while the response to $v_{\rm t}$ change is negligibly small) are $\pm \lesssim 0.1$–0.2 dex at most. The error bars attached in $A^{\rm N}$ (panel (d)) are the root-sum-square of δA (abundance error due to W perturbation of $\pm\delta W$), δ_T, δ_g, and δ_v.

5. Discussion

5.1. Impact of assigned abundance in non-LTE calculations

Before discussing the results obtained in Sect. 4, some comments may be in order regarding the Al abundance adopted in non-LTE calculations (Sect. 2.1), which we assumed the solar abundance ([Al/H] = 0). Since the departure coefficients resulting from statistical-equilibrium calculations more or less depend upon the input abundance, its validity in an application to actual stars needs to be checked.

Originally, it was intended to derive several non-LTE abundances for a star corresponding to different sets of departure coefficients calculated with various [Al/H] values, and obtain the consistent abundance solution by interpolation as done in Paper II (cf. Sect. 6.2 therein). Unfortunately, this approach did not work well in the present case, because $A^{\rm N}_{6243}$ determination (for a given W_{6243}) was found to be not always successful if [Al/H] is changed.

This situation is illustrated in Fig. 11, where the non-LTE corrections (Δ_0, $\Delta_{-0.5}$, Δ_{-1}) for each star derived by applying three sets of departure coefficients (corresponding to [Al/H] = 0.0, −0.5, and −1.0) are plotted against $T_{\rm eff}$. An inspection of this figure reveals that, while Δ_{4663} is insensitive to a change in [Al/H] (Fig. 11b), Δ_{6243} is appreciably [Al/H]-dependent (i.e., increasing with a decrease in [Al/H]; cf. Fig. 11a). More seriously, Δ_{6243} tends to be indeterminable as [Al/H] is decreased, especially at higher $T_{\rm eff}$ (note that the number of Δ_{6243} plotted in Fig. 11a becomes progressively fewer with a decrease in [Al/H]). This stems from the fact that the non-LTE line-weakening effect (due to the growth of filled-in emission caused by an increase of $S_{\rm L}$) becomes more important with a decrease in [Al/H], particularly in the higher $T_{\rm eff}$ regime. In such cases, non-LTE $W^{\rm N}_{6243}$ may not necessarily be a monotonically increasing function of A any more, since even an increase of the abundance can "weaken" the line strength by the effect of filled-in emission as the line-forming region shifts towards higher. Therefore, the solution of $A^{\rm N}_{6243}$ corresponding to a given W_{6243} tends to be undetermined at higher $T_{\rm eff}$ if departure coefficients for lower [Al/H] are used.

However, our choice of applying the non-LTE departure coefficients calculated with [Al/H] = 0 to all stars is reasonably sufficient from a practical point of view for the following reasons.

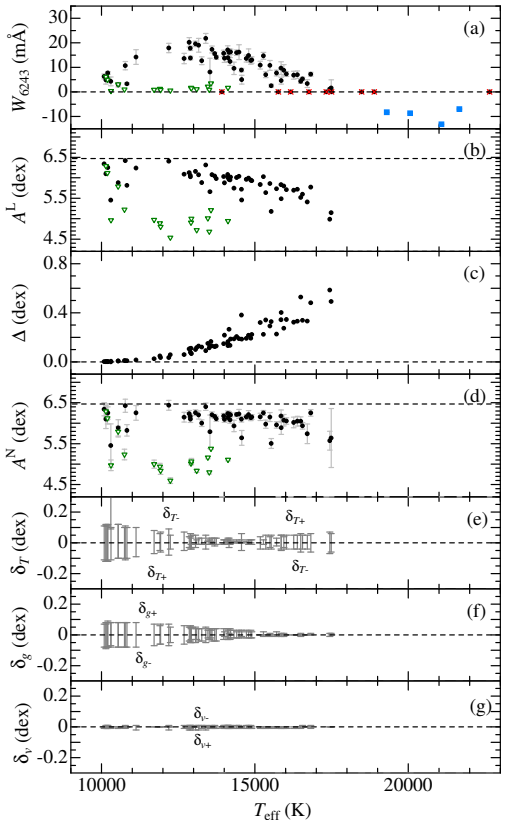

Figure 9. Abundance-related quantities for the Al II 6243 line are plotted against $T_{\rm eff}$. (a) W_{6243} (equivalent width), where the indicated error bars ($\pm\delta W$) are their uncertainties (see Sect. 4.4). (b) $A^{\rm L}$ (LTE aluminium abundance). (c) Δ ($\equiv A^{\rm N} - A^{\rm L}$; non-LTE correction). (d) $A^{\rm N}$ (non-LTE aluminium abundance). Here, the attached error bars are the root-sum-squares of δ_W (abundance ambiguities corresponding to δW), δ_T, δ_g, and δ_v. (e) δ_{T+} and δ_{T-} (abundance variations in response to $T_{\rm eff}$ changes of +3% and −3%). (f) δ_{g+} and δ_{g-} (abundance variations in response to $\log g$ changes of +0.2 dex and −0.2 dex). (g) δ_{v+} and δ_{v-} (abundance variations in response to perturbing the standard $v_{\rm t}$ value by $\pm 1\,{\rm km\,s^{-1}}$). Note that the signs of δ_T and δ_g are reversed on both sides of $T_{\rm eff}$ around ~ 15000 K. In panels (a), (b), and (d), the three cases where W or A values could not orderly be established (cf. Sect. 4.3 and 4.4) are distinguished by differently colored symbols: blue squares ⋯ (negative) W values directly measured by Gaussian fitting (appreciable emission-line case (i)); overplotted red crosses ⋯ tentatively assigned zero values (too weak line case (ii) due to filled-in emission in mid- to early-B stars); green open downward triangle ⋯ upper limit values (too weak line case (iii) due to Al deficiency in late B-type HgMn stars).

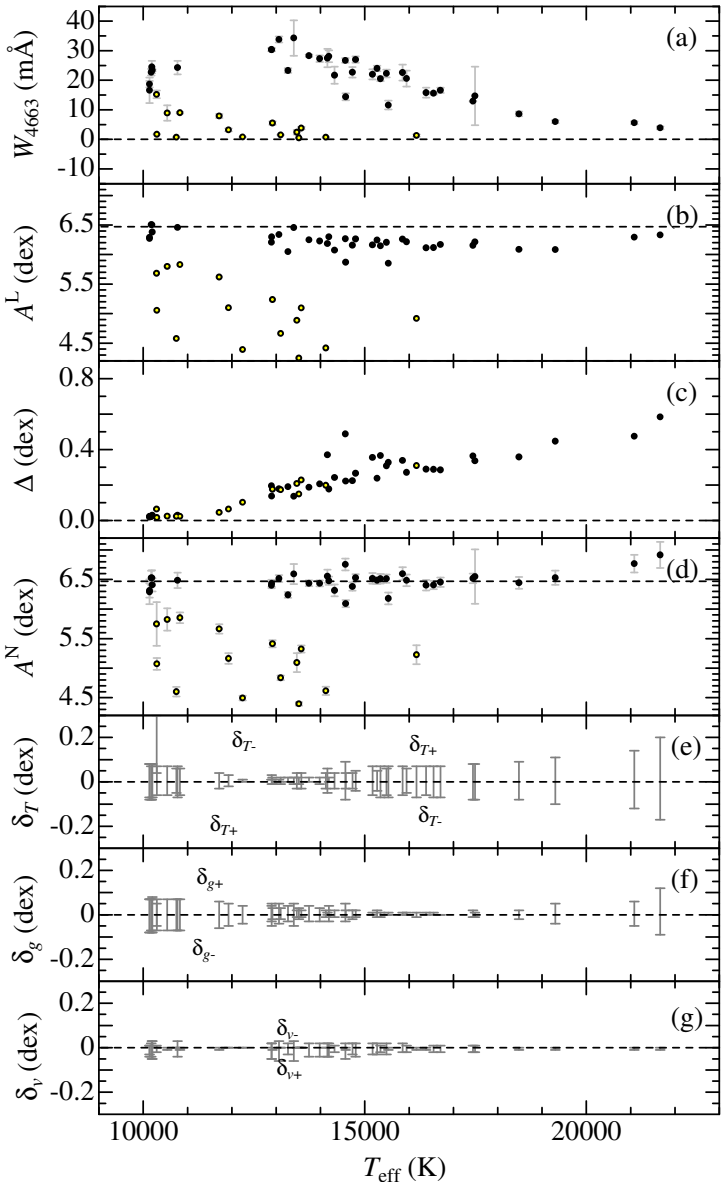

Figure 10. Abundance-related quantities for the Al II 4663 line (equivalent widths, LTE/NLTE abundances as well as NLTE corrections, and sensitivities due to perturbations of atmospheric parameters) are plotted against $T_{\rm eff}$. In panels (a)–(d), 15 chemically peculiar stars with $A^{\rm N}_{4663} < 6.0$ are distinguished by overplotting yellow small filled circles on the symbols. Otherwise, the same as in Fig. 9.

– Regarding normal B-type stars, since their Al abundances turned out almost solar as will be concluded in Sect. 5.3.1, the assumption of [Al/H] = 0 is justified.

– On the other hand, since chemically peculiar HgMn stars are considerably Al-deficient (cf. Sect. 5.3.2), applying the non-LTE departure coefficients calculated with [Al/H] = 0 is not consistent. Nevertheless, because Al abundances of such HgMn stars are not established from the problematic 6243 line (which yields only the upper limits in most cases), we have to anyhow invoke those ($A^{\rm N}_{4663}$) from the 4663 line. Then, since Δ_{4663} values are insensitive to [Al/H] (Fig. 11b), use of the [Al/H] = 0 set even in the 4663 line analysis of Al-deficient stars would not cause any serious problem.

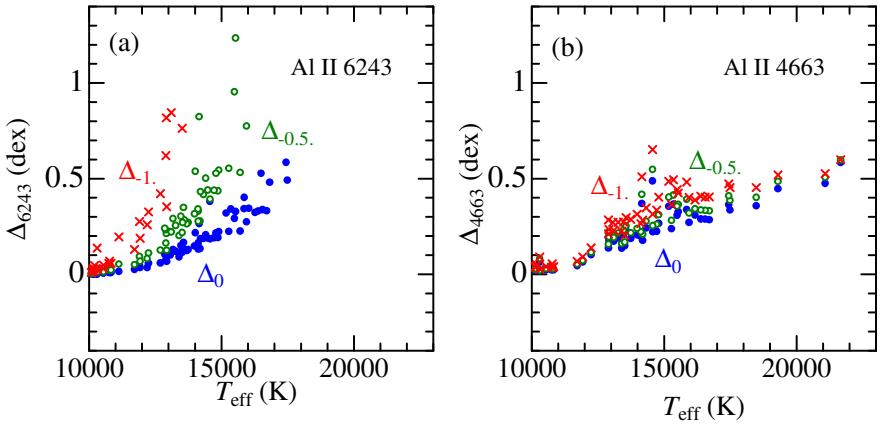

Figure 11. Test of how the non-LTE abundance correction for each star (derived from a given equivalent width) depends upon the Al abundance assumed in the statistical equilibrium calculations. Three kinds of non-LTE corrections (Δ_0, $\Delta_{-0.5}$, Δ_{-1}; depicted by filled symbols, open symbols, and crosses, respectively) are plotted against $T_{\rm eff}$, each of which correspond to different Al abundances adopted in non-LTE calculations ([Al/H] = 0, −0.5, and −1.0). Panels (a) and (b) are for Al II 6243 and Al II 4663, respectively.

5.2. Characteristics of each Al II line

Based on the results obtained in Sect. 4, we discuss the abundances derived from Al II 6243 and 4663 lines and assess their reliability and usability as abundance indicator. In addition, the problems involved with the Al II 3900 line, which was eventually abandoned to use, are also described. The discussion in this subsection is primarily confined to normal B-type stars, which may serve as a touchstone because of their prospective abundance homogeneity.

5.2.1. Al II 6243

The LTE abundances ($A^{\rm L}_{6243}$) derived from this line are considerably $T_{\rm eff}$-dependent (progressively decreasing with $T_{\rm eff}$) as shown in Fig. 9b. Although this trend is surely mitigated by applying the non-LTE corrections (Δ_{6243}; Fig. 9c), some systematic tendency remain unremoved in the non-LTE abundances ($A^{\rm N}_{6243}$; Fig. 9d), which means that they are insufficiently undercorrected. Therefore, our non-LTE calculations for this 6243 line are quantitatively still imperfect, despite that they satisfactorily predict the qualitative trend (e.g., emergence of emission feature at higher-$T_{\rm eff}$ regime; see Fig. 9a in comparison with Fig. 1a). Considering the remarkable [Al/H]-dependence of non-LTE corrections (Fig. 11). we may regard that the non-LTE results of this 6243 line are vulnerable to inadequacy in the adopted conditions (parameters) of the calculations, and thus less reliable in the quantitative sense.

5.2.2. Al II 4663

The LTE abundances ($A^{\rm L}_{4663}$) determined from the 4663 line also show some systematic tendency (decreasing with $T_{\rm eff}$; Fig. 10b). However, after the non-LTE corrections (Δ_{4663}; Fig. 10c) have been applied, this trend is almost removed in the non-LTE abundances ($A^{\rm N}_{4663}$) as can be confirmed in Fig. 10d. The exceptional outliers are two early B-type stars (HD 000886 and HD 035708) at $T_{\rm eff} \gtrsim 21000\,{\rm K}$, which might indicate that the reliability of the calculation may deteriorate at such a highest $T_{\rm eff}$ regime. The fact that the non-LTE abundances of normal B-type stars derived from this 4663 line are almost constant around $A \simeq 6.5$ over a wide temperature range ($10000\,{\rm K} \lesssim T_{\rm eff} \lesssim 20000\,{\rm K}$) suggests that this line is more reliable than the 6243 line as long as Al abundance determination is concerned. Besides, that this 4663 line is stronger (abundances are determinable even for Al-deficient stars) and does not show any apparent emission (even in early B stars) may be counted as additional evidence that this line is more advantageous than the 6243 line.

5.2.3. Al II 3900

This Al II 3900.675 line was originally selected as a potential candidate for Al abundance determination, because it was expected to have a sufficient strength (even stronger than the 6243/4663 lines) based on preparatory calculations by using the oscillator strength taken from VALD ($\log gf = -1.27$). However, observed strengths of this line in actual spectra were found to be much weaker than this expectation, suggesting the necessity of examining the reliability of $\log gf$(VALD) by checking other databases.

It was then found that, while Kurucz & Bell (1995)'s compilation presents the same value as VALD, the NIST database[8] gives a considerably lower value of $\log gf = -2.26$. Accordingly, this $\log gf$(NIST) value was eventually adopted for the Al II 3900 line in this study (cf. Table 1), which is regarded as being more reliable than $\log gf$(VALD).

Another problem involved with this Al II 3900 line is that it is severely contaminated by the neighboring Ti II line at 3900.539 Å, which is even stronger than the Al II line especially at lower $T_{\rm eff}$, though its strength drops down at higher $T_{\rm eff}$ (see Fig. 1c).

The situation mentioned above is graphically demonstrated in Fig. 12, where the observed and theoretically synthesized spectra around ∼3900 Å region are compared with each other for HD 160762 (17440 K), HD 209008 (15353 K), and HD 209459 (10204 K), which are normal stars with near-solar Al abundances of $A^{\rm N}_{4663} \sim 6.5$ (see Table 2). At any rate, this Al II 3900 line can not be used for Al abundance determinations of B-type stars because of being too weak and heavily affected by blending.

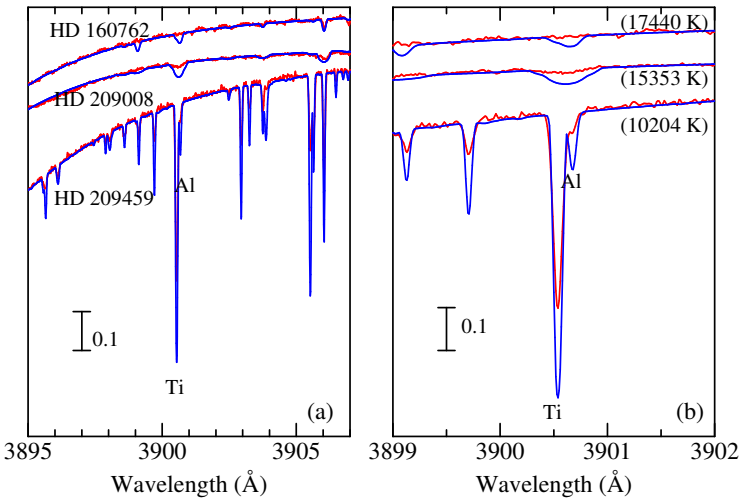

Figure 12. Observed spectra of HD 160762, HD 209008, and HD 209459 around the ∼ 3900 Å region comprising the Ti II 3900.539 and Al II 3900.675 lines (red lines) are compared with the theoretical spectra (blue lines) calculated with the solar Ti and Al abundances ($A_\odot$(Ti) = 4.99 and $A_\odot$(Al) = 6.47) under the assumption of LTE. Note that this region is on the red wing of Hζ 3889. Panels (a) and (b) are the wide view (3895–3907 Å) and the narrow view (3899–3902 Å), respectively.

[8]The Atomic Spectra Database of the National Institute of Standards and Technology. Available at https://www.nist.gov/pml/atomic-spectra-database.

5.3. Trends of Al abundances in B-type stars

In this subsection, the trends of Al abundances for normal and chemically peculiar stars are separately discussed. Here, we confine ourselves only to the non-LTE abundances derived from Al II 4663 line ($A^{\rm N}_{4663}$), which are considered to be more reliable (Sect. 5.2.2).

5.3.1. Normal B-type stars

The photospheric Al abundances of ordinary (non-CP) B-type stars should retain the composition of galactic gas from which they were formed. As mentioned in Sect. 5.2.2, the non-LTE Al abundances ($A^{\rm N}_{4663}$) turn out to be almost independent upon $T_{\rm eff}$ over a wide range of B-type stars at $10000\,{\rm K} \lesssim T_{\rm eff} \lesssim 20000\,{\rm K}$ (Fig. 10d), accomplishing a reasonable constancy. An inspection of Fig. 10d suggests that the demarcation line dividing the non-CP group (homogeneous Al abundances) and CP group (considerably Al-deficient) may be set at $A = 6.0$. Then, those 36 stars (out of 51 stars) satisfying the criterion $A^{\rm N}_{4663} > 6.0$ are regarded as normal B stars, for which the mean abundance is calculated as $\langle A^{\rm N}_{4663} \rangle = 6.47$ (standard deviation is $\sigma = 0.15$). Alternatively, if two highest-$T_{\rm eff}$ stars (HD 000886 and HD 035708) showing some deviation from the main trend (cf. Sect. 5.2.2) are excluded, $\langle A^{\rm N}_{4663} \rangle = 6.45$ with $\sigma = 0.13$.

This $\langle A^{\rm N}_{4663} \rangle$ is in remarkable agreement with the solar abundance ($A_\odot = 6.47$). That is, Al abundances of young B-type stars (representing the gas composition at the time of some $\sim 10^7$–$10^8\,{\rm yr}$ ago) are almost similar to that of the Sun (formed $\sim 4.6 \times 10^9\,{\rm yr}$ ago), which may be regarded as reasonable. Therefore, the trend of Al abundances in normal B-type stars is markedly different from the case of phosphorus (systematically subsolar by $\sim$0.2–0.3 dex in contradiction with the standard concept of galactic chemical evolution; cf. Paper II).

5.3.2. Peculiar HgMn stars

According to the demarcation in Sect. 5.3.1, those 15 stars with $A^{\rm N}_{4663} < 6.0$ are Al-deficient CP stars (yellow-dotted symbols in Fig. 10), which are mostly classified as HgMn stars (non-magnetic late B-type chemically peculiar stars). These stars are considerably underabundant in Al relative to the Sun. The extent of deficiency is diversified from star to star (by $\sim$0.5–2.0 dex; cf. Fig. 10d), though a rough tendency is observed that the anomaly tends to become more conspicuous with an increase in $T_{\rm eff}$ (from $[{\rm Al/H}] \sim -1$ around $T_{\rm eff} \sim 10000\,{\rm K}$ to $[{\rm Al/H}] \sim -2$ around $T_{\rm eff} \sim 14000\,{\rm K}$).

This is almost a reconfirmation of the trend shown in Fig. 3 of Ghazaryan & Alecian (2016), though their figure (see "Al_teff.pdf" included in their online material) indicates [Al/H] to be as low as ~ -2.5 (while the lowest [Al/H] in Fig. 10d is ~ -2), which might be due to the neglect of positive non-LTE corrections in previous determinations.

6. Summary and conclusion

Our understanding of the photospheric abundances of aluminium in B-type stars is not sufficient, despite that they may provide us with important information about the composition of galactic gas at the time of their formation. That is, previous abundance studies of this element seem to have been done more on chemically peculiar HgMn stars (late B-type), while those for relevant normal B-stars (retaining the original gas composition in their atmosphere) are comparatively scarce and do not seem to be sufficiently reliable because of the diversified results.

Motivated by this situation, a spectroscopic study was conducted to determine the aluminium abundances for 85 early-to-late B-type main-sequence stars ($10000\,\mathrm{K} \lesssim T_{\rm eff} \lesssim 22000\,\mathrm{K}$) (comprising normal stars as well as chemically peculiar HgMn stars) by using two Al II lines at 6243 and 4663 Å.

In order to take into account the non-LTE effect in the abundance analysis, non-LTE calculations were carried out on an extensive grid of models. It turned out that the non-LTE effect for these Al II 6243/4663 lines acts in the direction of line-weakening (i.e., line profile becomes shallower) caused by an overionization-induced line opacity decrease along with an enhancement of line source function, and this effect becomes more conspicuous with an increase in $T_{\rm eff}$ as well as with a decrease in $\log g$.

As for the observational data of program stars used for abundance determination, the same orange-region spectra as used in Paper II were adopted for the 6243 line, while the blue-region spectra available in the public-open database (ESO, CFHT, ELODIE) were employed for the 4663 line.

The abundance determination was carried out by the two-step process: (1) A spectrum-fitting analysis was first applied to the wavelength regions of these two lines and their equivalent widths (W_{6243} and W_{4663}) were derived from the fitting-based abundance solutions. (2) Then, non-LTE abundances/corrections as well as possible errors were evaluated from such established W values. The following conclusions are extracted from the results of Al abundances.

Regarding the non-LTE abundances of normal stars resulting from the Al II 6243 line, some $T_{\rm eff}$-dependent systematic trend remains unremoved, which means that non-LTE corrections evaluated for this line are quantitatively insufficient, despite that our non-LTE calculation reasonably reproduces the qualitative behavior of this line (e.g., appearance of emission at the higher-$T_{\rm eff}$ regime of early B-type stars).

Meanwhile, for the case of the Al II 4663 line, which is more advantageous than the 6243 line because it is stronger without showing any emission, the resulting non-LTE abundances of ordinary B stars are almost constant at the solar abundance ($A \simeq 6.5$) over the wide $T_{\rm eff}$ range ($\sim$10000–20000 K), which suggests that the abundances derived from this line are successfully non-LTE-corrected and trustable.

Therefore, according to these results derived from the Al II 4663 line, we may reasonably state that the Al abundance of the galactic gas, from which early-to-late B-type stars were born several times $\sim 10^7$–10^8 yr ago, is almost similar to the solar composition. This consequence is markedly different from the case of phosphorus (systematically subsolar by $\sim$0.2–0.3 dex; cf. Paper II).

As to the photospheric Al abundances of chemically peculiar HgMn stars (10000 K $\lesssim T_{\rm eff} \lesssim$ 15000 K), our analysis resulted that this element is conspicuously underabundant by $\sim$0.5–2 dex in comparison with the Sun (as well as normal B stars) and the extent of deficiency tends to increase towards higher $T_{\rm eff}$, which is a reconfirmation of the characteristics already reported in the past literature.

Acknowledgements. This investigation has made use of the SIMBAD database, operated by CDS, Strasbourg, France, and the VALD database operated at Uppsala University, the Institute of Astronomy RAS in Moscow, and the University of Vienna. This study is partly based on the data obtained from the ESO Science Archive Facility, ELODIE archive, and CFHT Science Archive Data (via CADC), as detailed in Table 3.

References

Allen, C. S. 1998, Abundance analysis of normal and mercury-manganase type late-B stars from optical spectra, PhD thesis, University College London, London, UK

Anders, E. & Grevesse, N. 1989, *Geochim. Cosmochim. Acta*, **53**, 197, DOI:10.1016/0016-7037(89)90286-X

Andrievsky, S. M., Spite, M., Korotin, S. A., et al. 2008, *Astronomy and Astrophysics*, **481**, 481, DOI:10.1051/0004-6361:20078837

Asplund, M., Grevesse, N., Sauval, A. J., & Scott, P. 2009, *Ann. Rev. Astron. Astrophys.*, **47**, 481, DOI:10.1146/annurev.astro.46.060407.145222

Baumüller, D. & Gehren, T. 1997, *Astronomy and Astrophysics*, **325**, 1088

Cunto, W. & Mendoza, C. 1992, *Revista Mexicana de Astronomia y Astrofisica*, **23**, 107

Fossati, L., Ryabchikova, T., Bagnulo, S., et al. 2009, *Astronomy and Astrophysics*, **503**, 945, DOI:10.1051/0004-6361/200811561

Ghazaryan, S. & Alecian, G. 2016, *Monthly Notices of the RAS*, **460**, 1912, DOI:10.1093/mnras/stw911

Golriz, S. S. & Landstreet, J. D. 2017, *Monthly Notices of the RAS*, **466**, 1597, DOI:10.1093/mnras/stw3144

Kurucz, R. L. 1993, *ATLAS9 Stellar Atmosphere Programs and 2 km/s grid, Kurucz CD-ROM, No. 13* (Cambridge, MA: Harvard-Smithsonian Center for Astrophysics)

Kurucz, R. L. & Bell, B. 1995, *Atomic Line Data, Kurucz CD-ROM, No. 23* (Cambridge, MA: Harvard-Smithsonian Center for Astrophysics)

Mihalas, D. 1978, *Stellar Atmospheres, 2nd ed.* (San Francisco: W. H. Freeman)

Monier, R. 2022, *Res. Notes AAS*, **6**, 245, DOI:10.3847/2515-5172/aca4d0

Niemczura, E., Morel, T., & Aerts, C. 2009, *Astronomy and Astrophysics*, **506**, 213, DOI:10.1051/0004-6361/200911931

Pintado, O. I. & Adelman, S. J. 1993, *Monthly Notices of the RAS*, **264**, 63, DOI:10.1093/mnras/264.1.63

Przybilla, N., Butler, K., Becker, S. R., & Kudritzki, R. P. 2006, *Astronomy and Astrophysics*, **445**, 1099, DOI:10.1051/0004-6361:20053832

Ryabchikova, T., Piskunov, N., Kurucz, R. L., et al. 2015, *Physica Scripta*, **90**, 054005, DOI:10.1088/0031-8949/90/5/054005

Takeda, Y. 1991, *Astronomy and Astrophysics*, **242**, 455

Takeda, Y. 1995, *Publications of the ASJ*, **47**, 287

Takeda, Y. 2023, *Contrib. Astron. Obs. Skalnaté Pleso*, **53**, 31 (Paper I), DOI:10.31577/caosp.2023.53.2.31

Takeda, Y. 2024, *Acta Astron.*, **74**, 43 (Paper II), DOI:10.32023/0001-5237/74.1.3

Takeda, Y. 2025, *Res. Astron. Astrophys.*, **25**, 025016, DOI:10.1088/1674-4527/adaa48

Contrib. Astron. Obs. Skalnaté Pleso **56/2**, 36 – 54, (2026)
https://doi.org/10.31577/caosp.2026.56.2.36

Surface gravitational redshift of massive protoneutron stars: effects of σ^* and ϕ mesons

J.L. Huo[1], X.H. Wu[1], W.B. Ding[2] and X.F. Zhao[1]

[1] *School of Sciences, Southwest Petroleum University, Chengdu, 610500, China (E-mail: jlhuo2006@126.com)*

[2] *College of Physics and Electronic Information Engineering, Guangxi Minzu Normal University, Chongzuo, 532200, China*

Received: December 21, 2025; Accepted: February 16, 2026

Abstract. The effects of hyperon interactions (occurring through the coupling of hyperons to the σ^* and ϕ mesons) on the surface gravitational redshift z of proto-neutron stars (PNSs)—specifically PSR J0740+6620, PSR J0348+0432, PSR J1614-2230, and PSR J0737-3039A—are investigated using relativistic mean field theory. It is found that the increase in central pressure and central energy density due to hyperon interactions becomes more pronounced for higher-mass PNSs, while for lower-mass PNSs this effect is negligible. When hyperon interactions are included, the mass M, compactness M/R, and surface gravitational redshift z of a PNS all decrease at a given central energy density ε_c. For the higher-mass PNSs PSR J0740+6620 and PSR J0348+0432, the influence of hyperon interactions on compactness M/R and surface redshift z is significant. In contrast, for the lower-mass PNSs PSR J1614-2230 and PSR J0737-3039A, the effect on M/R and z is negligible.

Key words: stars: binaries – general: stars

1. Introduction

Neutron stars (NSs) possess extremely strong magnetic fields and rotate at very high speeds (Deng et al., 2021). Some of their intriguing properties may be explained by dark matter (Ding et al., 2022). NSs are very massive and have very small radii, resulting in extremely high densities, which significantly influence their properties (Mu et al., 2017; Li et al., 2021). Consequently, once the mass of a NS is determined, it is possible to infer certain characteristics of the star.

As early as 2004, the double NS system PSR J0737–3039 was discovered (Lyne et al., 2004). The NS PSR J0737–3039A has a typical NS mass, with reported values of $M = 1.337$ $M_\odot$ (Morrison et al., 2004) or $M = 1.3381 \pm 0.0007$ $M_\odot$ (Kramer et al., 2006).

NSs with exceptionally high masses have also been discovered in recent decades. The NS PSR J1614–2230, with a mass of $M = 1.97 \pm 0.04$ $M_\odot$, was identified in 2010 (Demorest et al., 2010). Its mass was later refined to $M =$

$1.93 \pm 0.07\ \mathrm{M}_\odot$ in 2016 (Fonseca et al., 2016). Subsequently, PSR J0348+0432, with a mass of $M = 2.01 \pm 0.04\,\mathrm{M}_\odot$, was found in 2013 (Antoniadis et al., 2013). An even more massive NS, PSR J0740+6620, with a mass of $M = 2.14^{+0.10}_{-0.09}\,\mathrm{M}_\odot$, was observed in 2020 (Cromartie et al., 2020). Its mass and radius were later precisely determined to be $M = 2.08^{+0.07}_{-0.07}\,\mathrm{M}_\odot$ by (Fonseca et al., 2021) and $R = 13.7^{+2.6}_{-1.5}$ km by (Miller et al., 2021) in 2021. Most recently, the NS PSR J0952–0607, with a record mass of $M = 2.35^{+0.17}_{-0.17}\,\mathrm{M}_\odot$, was discovered in 2022 (Romani et al., 2022).

These NSs are relatively massive, and their mass must constrain their properties. Therefore, measuring NS masses is crucial for determining their structure and internal properties. Although the massive NSs PSR J1614-2230, PSR J0348+0432, and PSR J0740+6620 are not the heaviest discovered to date, studying the influence of their precisely measured masses on their properties remains highly significant.

After a supernova, a NS is formed in the core. Prior to that, a proto-neutron star (PNS) emerges, which can reach temperatures as high as 30 MeV. Subsequently, the PNS cools via neutrino emission and evolves into a NS (Burrows & Lattimer, 1986). Thus, the study of PNSs is important for understanding the formation and evolution of NSs.

In theoretical research, we can compare PNS evolutionary models with observational data of cold NSs. The purpose of this comparison is not to directly equate the transient and steady states, but rather to leverage the continuous physical link—from the hot PNS to the cold NS—established by theoretical models. By contrasting the initial/early stages of the evolutionary trajectory with the final/observed state, we aim to jointly constrain the microphysics of dense matter.

The description of NS matter can incorporate σ, ω, and ρ mesons to represent the interaction between nucleons (Glendenning, 1997), while interactions between hyperons can be described by the mesons $f_0(1020)$ (denoted as σ^*) and $\phi(975)$ (denoted as ϕ) (Schaffner et al., 1994).

Closely related to the mass and radius of a NS is the surface gravitational redshift, which depends directly on the compactness M/R (Glendenning, 1997). Therefore, studying the surface gravitational redshift of NSs is as important as investigating their compactness.

In this work, we employ relativistic mean field (RMF) theory (Zhou, 2016) with the baryon octet to examine the influence of the σ^* and ϕ mesons on the surface gravitational redshift of massive PNSs PSR J0740+6620, PSR J0348+0432, and PSR J1614-2230. For comparison, we also calculate the surface gravitational redshift of the typical-mass PNS PSR J0737-3039A.

2. RMF theory at finite temperature: the infinite system

The Lagrangian density of infinite nuclear matter is as follows (Glendenning, 1997)

$$\begin{aligned}\mathcal{L} = & \sum_B \overline{\Psi}_B(i\gamma_\mu\partial^\mu - m_B + g_{\sigma B}\sigma + g_{\sigma^* B}\sigma^* \\ & -g_{\omega B}\gamma^0\omega - g_{\phi B}\gamma^0\phi - g_{\rho B}\gamma^0\tau_3\rho)\Psi_B \\ & -\frac{1}{2}m_\sigma^2\sigma^2 - \frac{1}{3}g_2\sigma^3 - \frac{1}{4}g_3\sigma^4 \\ & +\frac{1}{2}m_\omega^2\omega^2 + \frac{1}{2}m_\rho^2\rho^2 - \frac{1}{2}m_{\sigma^*}^2\sigma^{*2} + \frac{1}{2}m_\phi^2\phi^2 \\ & + \sum_{\lambda=e,\mu} \overline{\Psi}_\lambda \left(i\gamma_\mu\partial^\mu - m_\lambda\right)\Psi_\lambda. \end{aligned} \tag{1}$$

Given neutrino binding, the baryonic partition function of infinite nuclear matter at finite temperature is

$$\begin{aligned} lnZ_B = & \frac{V}{T}\langle\mathcal{L}\rangle + \sum_B \frac{2J_B+1}{2\pi^2} \\ & \int_0^\infty k^2 dk \left\{ ln\left[1 + e^{-(\varepsilon_B(k)-\mu_B)/T}\right]\right\}. \end{aligned} \tag{2}$$

The total baryon number density (Glendenning, 1987a,b) is

$$\rho = \sum_B \frac{2J_B+1}{2\pi^2} b_B \int_0^\infty k^2 n_B(k) dk. \tag{3}$$

The energy density and the pressure of baryons and mesons respectively are

$$\begin{aligned} \varepsilon = & \frac{1}{2}m_\sigma^2\sigma^2 + \frac{1}{2}m_{\sigma^*}^2\sigma^{*2} + \frac{1}{3}g_2\sigma^3 + \frac{1}{4}g_3\sigma^4 \\ & +\frac{1}{2}m_\omega^2\omega_0^2 + \frac{1}{2}m_\phi^2\phi^2 + \frac{1}{2}m_\rho^2\rho_{03}^2 \\ & +\sum_B \frac{2J_B+1}{2\pi^2}\int_0^\infty \kappa^2 n_B(k)\mathrm{d}\kappa\sqrt{\kappa^2 + m_B^{*2}}, \end{aligned} \tag{4}$$

$$\begin{aligned} p = & -\frac{1}{2}m_\sigma^2\sigma^2 - \frac{1}{2}m_{\sigma^*}^2\sigma^{*2} - \frac{1}{3}g_2\sigma^3 - \frac{1}{4}g_3\sigma^4 \\ & +\frac{1}{2}m_\omega^2\omega_0^2 + \frac{1}{2}m_\phi^2\phi^2 + \frac{1}{2}m_\rho^2\rho_{03}^2 \\ & +\frac{1}{3}\sum_B \frac{2J_B+1}{2\pi^2}\int_0^\infty \frac{\kappa^4}{\sqrt{\kappa^2 + m_B^{*2}}} n_B(k) d\kappa. \end{aligned} \tag{5}$$

Here, $n_B(k)$ is the Fermi-Dirac distribution function of baryons

$$n_B(k) = \frac{1}{1 + exp\left[\left(\varepsilon_B(k) - \mu_B\right)/T\right]}. \tag{6}$$

If we don't take into account the interactions between leptons at finite temperatures, their partition function is

$$\begin{aligned} lnZ_L = & \frac{V}{T}\sum_i \frac{\mu_i^4}{24\pi^2}\left[1 + 2\left(\frac{\pi T}{\mu_i}\right)^2 + \frac{7}{15}\left(\frac{\pi T}{\mu_i}\right)^4\right] \\ & + V\sum_\lambda \frac{1}{\pi^2}\int_0^\infty k^2 dk\left\{ln\left[1 + e^{-(\varepsilon_\lambda(k) - \mu_\lambda)/T}\right]\right\}, \end{aligned} \tag{7}$$

the first line represents the contribution of massless neutrinos and the second line the contribution of electrons and μs.

The lepton number density is

$$\rho_l = \frac{1}{\pi^2}\int_0^\infty k^2 n_l(k) dk, \tag{8}$$

$$\rho_\nu = \frac{\pi^2 T^2 \mu_\nu + \mu_\nu^3}{6\pi^2}. \tag{9}$$

The energy density and the pressure of leptons are

$$\begin{aligned} \varepsilon &= \sum_l \frac{1}{\pi^2}\int_0^\infty \kappa^2 n_l(k) \mathrm{d}\kappa \sqrt{\kappa^2 + m_l^2} \\ &= \sum_\nu \left(\frac{7\pi^2 T^4}{120} + \frac{T^2\mu_\nu^2}{4} + \frac{\mu_\nu^4}{8\pi^2}\right), \end{aligned} \tag{10}$$

$$\begin{aligned} p &= \frac{1}{3}\sum_l \frac{1}{\pi^2}\int_0^\infty \frac{\kappa^4}{\sqrt{\kappa^2 + m_l^2}} n_l(k) d\kappa \\ &= \sum_\nu \frac{1}{360}\left(7\pi^2 T^4 + 30 T^2 \mu_\nu^2 + \frac{15\mu_\nu^4}{\pi^2}\right). \end{aligned} \tag{11}$$

The chemical potentials of baryons are

$$\mu_i = \mu_n - q_i\left(\mu_e - \mu_{\nu e}\right). \tag{12}$$

We can obtain the mass and the radius of a PNS through the Tolman-Oppenheimer-Volkoff (TOV) equation (Tolman, 1939; Oppenheimer & Volkoff, 1939)

$$\frac{\mathrm{d}p}{\mathrm{d}r} = -\frac{(p + \varepsilon)\left(m + 4\pi r^3 p\right)}{r\left(r - 2m\right)}, \tag{13}$$

$$m = 4\pi\int_0^r \varepsilon r^2 \mathrm{d}r, \tag{14}$$

$$M = m(R). \tag{15}$$

The TOV equations are only applicable to spherically symmetric, static (i.e., non-rotating and time-invariant) stellar objects. However, NSs are known to rotate very rapidly, and PNSs evolve rapidly over time. Neglecting rotation and temporal evolution will introduce certain errors. (1) The error from neglecting rotational effects depends mainly on the rotational speed. For slow rotation (period P$\geq$ 10 ms), the centrifugal force correction to the global structure (mass, radius) is approximately 1% to a few percent, and the TOV solution serves as a good approximation. For potentially extremely rapid rotation (P $\sim$ 1 ms), centrifugal support becomes significant and may lead to deviations exceeding 10% in mass and radius estimates, while also failing to describe stellar oblateness. This study aims to investigate the influence of the equation of state (EoS) within a static baseline; therefore, the spherical symmetry assumption is intentionally adopted to focus the problem. The spherical symmetry and static assumptions are limitations, and conclusions for rapidly rotating stars require further examination in axisymmetric models. (2) The error induced by neglecting temporal evolution. The TOV equations describe instantaneous hydrostatic equilibrium. During the middle and late stages of PNS evolution ($t > 1$ s), although temperature and composition change rapidly, the timescale for establishing hydrostatic equilibrium (milliseconds) is much shorter than the evolutionary timescale (10 seconds). The system can thus be considered to undergo a sequence of quasi-static equilibrium states. Therefore, our sequence of static solutions can be interpreted as potential 'snapshots' along the PNS cooling path. While this approach cannot self-consistently describe the evolutionary timescale, it clearly reveals the dependence of the structure on internal physical conditions. The dynamical phase of the very early stage (t $<$ 1 s) is beyond the applicable scope of this model. In summary, we adopt the simplified model in order to reveal the core physical mechanisms within a controlled framework and to provide a theoretical benchmark for more complex multidimensional time-dependent simulations.

The surface gravitational redshift of a PNS can be calculated by (Glendenning, 1997):

$$z = \frac{1}{\sqrt{1 - 2(M/R)}} - 1. \tag{16}$$

This formula is derived from the Schwarzschild metric, which holds valid above the surface of any star. Therefore, this formula is applicable to any relativistic star.

3. The parameters

We calculate the mass and radius of the PNSs using the following eight groups of nucleon coupling constants: DD-ME1 (Typel & Wolter, 1999), FSU2H (Tolos et al., 2017), FSU2R (Tolos et al., 2017), FSUGold (Todd-Rutel & Piekarewicz,

2005), GL85 (Glendenning, 1985), GL97 (Glendenning, 1997), GM1 (Glendenning & Moszkowski, 1991), and TW99 (Typel & Wolter, 1999).

The ratios of hyperon–hyperon coupling constants to nucleon–nucleon coupling constants can be defined as $x_{\sigma h} = \frac{g_{\sigma h}}{g_\sigma}$, $x_{\omega h} = \frac{g_{\omega h}}{g_\omega}$, $x_{\rho h} = \frac{g_{\rho h}}{g_\rho}$, where h denotes the hyperons Λ, Σ, and Ξ.

The coupling constant between ρ mesons and nucleons is derived from quark SU(6) symmetry (Schaffner & Mishustin, 1996; Schaffner-Bielich & Gal, 2000). The mass of a PNS increases with larger values of $x_{\sigma h}$ and $x_{\omega h}$ (Zhao, 2019). Consequently, to obtain the PNS mass, one must select sufficiently large values for these parameters. The theoretical baseline for the parameter $x_{\omega h}$ is approximately 0.667 (Glendenning, 1997). In phenomenological models, its typical variation range is about 0.5 to 1.0 (Weissenborn et al., 2012; Chatterjee & Vidana, 2016). To construct a viable model that includes hyperons while still yielding NSs with a mass of $\sim$2 $M_\odot$, it is necessary to adopt a larger value of $x_{\omega h}$ (i.e., a strong repulsive potential) to compensate for the softening of the EoS induced by the presence of hyperons. A value of $x_{\omega h} \sim 0.8$ is commonly required to satisfy this observational constraint (Weissenborn et al., 2012). Therefore, selecting 0.9 is reasonable and consistent with current observational limits. Within a more refined SU(3) flavor symmetry framework, the vector coupling constants for different hyperons (Λ, Σ, Ξ) can and do differ (Schaffner & Mishustin, 1996; Schaffner-Bielich & Gal, 2000). The present work adopts a uniform value of 0.9 as a simplification, aiming first to focus on the overall effects of the presence of hyperons. Investigating the differences in the couplings of different hyperons is an important direction for future research. In this work, we set $x_{\omega h}$=0.9, while $x_{\sigma h}$ is determined by fitting the hyperon potential well depth in saturated nuclear matter (Glendenning, 1997)

$$U_h^{(N)} = m_n \left(\frac{m_n^*}{m_n} - 1 \right) x_{\sigma h} + \left(\frac{g_\omega}{m_\omega} \right)^2 \rho_0 x_{\omega h}. \tag{17}$$

In this work, we adopt the hyperon potential depths $U_\Lambda^{(N)}$ = -30 MeV (Schaffner-Bielich & Gal, 2000; Weissenborn et al., 2012; Gal et al., 2016), $U_\Sigma^{(N)}$ = 30 MeV (Schaffner-Bielich & Gal, 2000; Weissenborn et al., 2012; Gal et al., 2016; Batty et al., 1997), and $U_\Xi^{(N)}$ = -14 MeV (Harada et al., 2010).

We take the coupling parameters between the mesons σ^* and ϕ and the hyperons as (Schaffner et al., 1994)

$$g_{\phi\Xi} = 2g_{\phi\Lambda} = 2g_{\phi\Sigma} = -2\sqrt{2}g_\omega/3, \tag{18}$$

$$g_{\sigma^*\Lambda}/g_\sigma = g_{\sigma^*\Sigma}/g_\sigma = 0.69, \tag{19}$$

$$g_{\sigma^*\Xi}/g_\sigma = 1.25. \tag{20}$$

The temperature parameter in PNS models plays a dual role: it strongly influences local energy density and pressure through the T^4 term, while the structure

of the TOV equations may render the overall macroscopic properties less sensitive to it. For example, in earlier calculations (Zhao et al., 2025), when the temperature of the PNS was raised from 14 MeV to 21 MeV, the central energy density decreased from 1.028×10^{15}g cm^{-3} to 1.019×10^{15}g cm^{-3} (by 0.9%), and the central pressure decreased from 2.178×10^{35}dyne cm^{-2} to 2.118×10^{35}dyne cm^{-2}d (by 6%). In contrast, the computed maximum mass increased from 2.2562 $M_\odot$ to 2.2576 $M_\odot$ (a rise of 0.0014 $M_\odot$), representing only a 0.06% increase. In the present work, the temperature of the PNSs is chosen as T=15 MeV (Burrows & Lattimer, 1986). The chosen temperature of $T = 15$ MeV in this study corresponds to the typical physical conditions within the PNS core during the initial tens of seconds following a supernova explosion. This temperature value is based on the standard understanding of PNS evolution. Simulation studies indicate that at this stage, due to neutrino trapping and strong compression, the PNS core can reach temperatures of 10–30 MeV (Pons et al., 1999; Keil et al., 2003). When investigating neutrino processes, the EoS , and nucleosynthesis inside a PNS, the range of 10–20 MeV is widely considered as the characteristic temperature range (Hempel & Schaffner-Bielich, 2010; Roberts et al., 2012). Therefore, the selection of $T = 15$ MeV aims to represent this high-energy, high-density environment, in order to explore the behavior of relevant nuclear processes under astrophysical conditions.

In 2019, precise measurements of the NS PSR J0030+0451 were obtained. Riley et al. reported a mass $M = 1.34^{+0.15}_{-0.16}$ $M_\odot$ and a radius $R = 12.71^{+1.14}_{-1.19}$ km (Riley et al., 2019), while Miller et al. found $M = 1.44^{+0.15}_{-0.14}$ $M_\odot$ and $R = 13.02^{+1.24}_{-1.06}$ km (Miller et al., 2019). The accurate determination of its mass and radius is highly significant, providing a key observational constraint for selecting viable equations of state (EoS) in NS modeling

The mass values (or maximum masses) of PNSs as functions of radius are presented in Fig. 1. The four thick lines correspond to the PNS masses associated with PSR J0740+6620, PSR J0348+0432, PSR J1614-2230, and PSR J0737-3039A, respectively. The results show that only the TW99, DD-ME1, and GM1 models can reproduce the masses of all these four PNSs. The mass–radius relations predicted by TW99, DD-ME1, and GM1 are displayed in the right panel of Fig. 1. It can be seen that for a given mass, there exist two radii, among which the radii on the left side of the mass peak belong to the unstable non-physical branch, while those on the right side belong to the stable physical branch. Due to the residual high thermal pressure and particle components that have not fully reached β-equilibrium inside the PNS, its radius during the early evolutionary stages (e.g., 10–30 seconds after birth) is expected to be 10%–30% larger than that of its cold NS counterpart of the same mass (Burrows & Lattimer, 1986; Pons et al., 1999; Zhao, 2011). This difference serves as an important testable feature linking PNS evolutionary theory with observations of cold NSs. We see that the mass and radius of the PNS given by the GM1 model agree best with the results from Riley et al. and Miller et al. (see the shaded region in the

right panel of Fig. 1) among these models. Therefore, in this work, the GM1 model is adopted to investigate the effect of hyperon interactions on the surface gravitational redshift of PNSs.

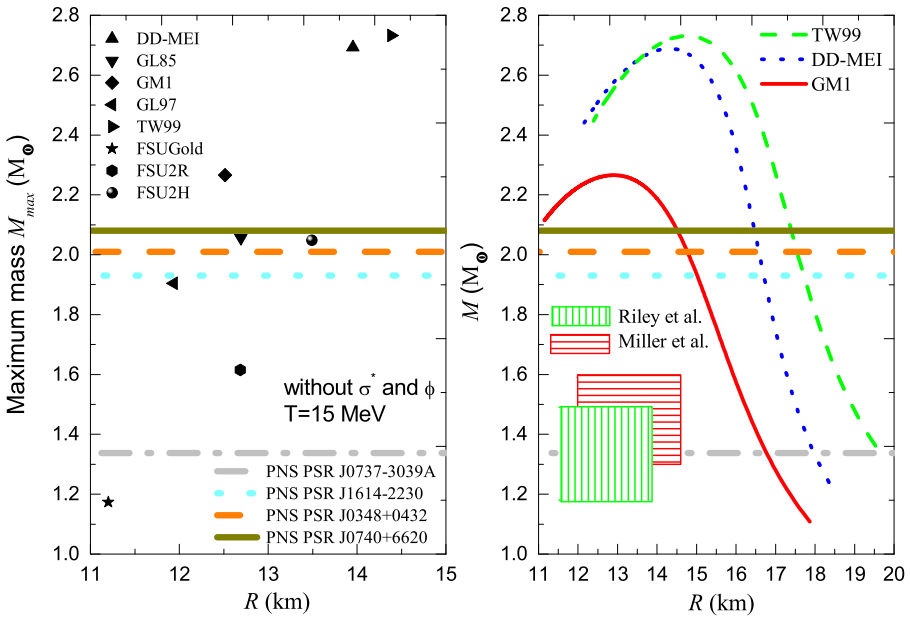

Figure 1. The mass M (or maximum mass M_{max}) of the PNS as a function of its radius R. The four thick lines correspond to the masses of the PNSs for PSR J0740+6620, PSR J0348+0432, PSR J1614–2230, and PSR J0737–3039A, respectively.

4. Mass and radius of PNSs

Figure 2 shows the radius R and mass M of a PNS as functions of the central energy density ε_c, calculated using the GM1 EoS. The four thick horizontal lines indicate the measured masses of the observed pulsars PSR J0740+6620, PSR J0348+0432, PSR J1614-2230, and PSR J0737-3039A, respectively. Solid red curves correspond to models without hyperon–hyperon interactions, while dashed green curves represent models that include these interactions.

Figure 2 shows that the mass M of the PNS increases while the radius R decreases with increasing central energy density ε_c. When hyperonic interactions are included, the mass M of the PNS decreases and its radius R increases at the same central energy density ε_c relative to the case without such interactions

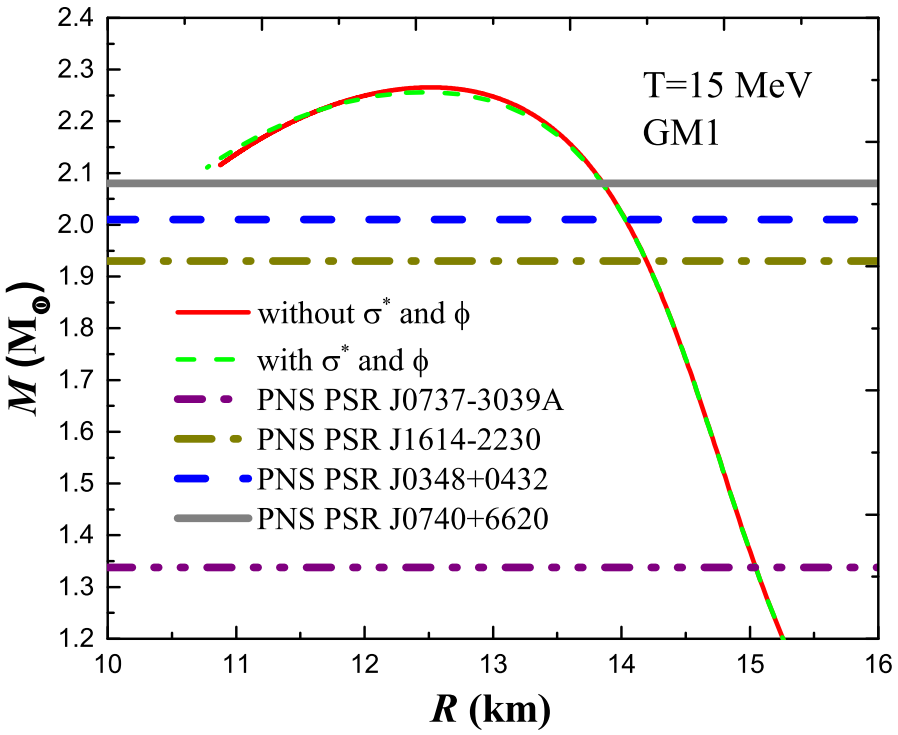

Figure 2. The mass M of a PNS as functions of radius R calculated within the GM1 EOS. The four thick horizontal lines mark the measured masses of the observed pulsars PSR J0740+6620, PSR J0348+0432, PSR J1614-2230, and PSR J0737-3039A, respectively. Solid red curves correspond to models without hyperon–hyperon interactions; dashed green curves include hyperon–hyperon interactions.

Under the constraints provided by the respective masses of the PNSs PSR J0740+6620, PSR J0348+0432, PSR J1614-2230, and PSR J0737-3039A (see Table 1), and when hyperonic interactions are considered, the radius of PSR J0740+6620 decreases from $R = 13.858$ km to $R = 13.849$ km, a reduction of about 0.065%. The radius of PSR J0348+0432 decreases from $R = 14.031$ km to $R = 14.029$ km, or about 0.014%. The radii of PSR J1614-2230 and PSR J0737-3039A remain unchanged at $R = 14.199$ km and $R = 15.05$ km, respectively (see Table 1). These results suggest that the reduction in radius due to hyperonic interactions is larger for more massive PNSs, while for less massive PNSs the effect on the radius is negligible.

Table 1. The calculated physical quantities of PNSs. The masses of PSR J0740+6620 (hereafter J0740+6620), PSR J0348+0432 (J0348+0432), PSR J1614-2230 (J1614-2230), and PSR J0737-3039A (J0737-3039A) are $M = 2.08$ $M_\odot$, $M = 2.01$ $M_\odot$, $M = 1.93$ $M_\odot$, and $M = 1.338$ $M_\odot$, respectively. The corresponding radius R, central energy density ε_c, central pressure p_c, compactness M/R, and surface gravitational redshift z are derived for each star. The units are as follows: R in km, ε_c in 10^{15} g·cm^{-3}, p_c in 10^{35} dyne·cm^{-2}, and M/R in $M_\odot$/km. These results are obtained using the GM1 nucleon coupling constant and assuming a uniform temperature of $T = 15$ MeV for all PNS models..

Parameter	R	ε_c	p_c	M/R	z
J0740+6620					
Withoutσ^* and ϕ	13.858	1.0202	2.1650	0.15009	0.3404
With σ^* and ϕ	13.849	1.0290	2.1798	0.15019	0.3402
Rate of variation	-0.065%	0.980%	0.739%	0.067%	-0.059%
J0348+0432					
Without σ^* and ϕ	14.031	0.9339	1.8300	0.14325	0.3168
With σ^* and ϕ	14.029	0.9365	1.8322	0.14327	0.3167
Rate of variation	-0.014%	0.644%	0.120%	0.014%	-0.032%
J1614-2230					
no σ^* and ϕ	14.199	0.856	1.533	0.1358	0.2921
with σ^* and ϕ	14.199	0.857	1.533	0.1358	0.2921
Rate of variation	0	0.117%	0%	0%	0%
J0737-3039A					
no σ^* and ϕ	15.05	0.563	0.553	0.0887	0.1639
with σ^* and ϕ	15.05	0.563	0.553	0.0887	0.1639
Rate of variation	0%	0%	0%	0%	0%

5. Energy density and pressure in PNSs

Figure 3 shows the pressure p of the PNS as a function of energy density ε. The thick vertical lines indicate the central energy densities ε_c for the PNSs of PSR J0740+6620, PSR J0348+0432, PSR J1614–2230, and PSR J0737–3039A. Solid lines correspond to models without hyperon interactions, and dashed lines to those with hyperon interactions included. It can be seen that p generally increases with ε. When hyperon interactions are considered, however, p is reduced at a given ε compared to the case without such interactions.

Constrained by the mass of the corresponding PNSs, and given the interactions between hyperons, the central pressure of PNS PSR J0740+6620 increases from p_c= 2.1650× 10^{35}dyne.cm^{-2} to p_c=2.1798× 10^{35} dyne.cm^{-2}, increased by about 0.739%; the central pressure of PNS PSR J0348+0432 increases from

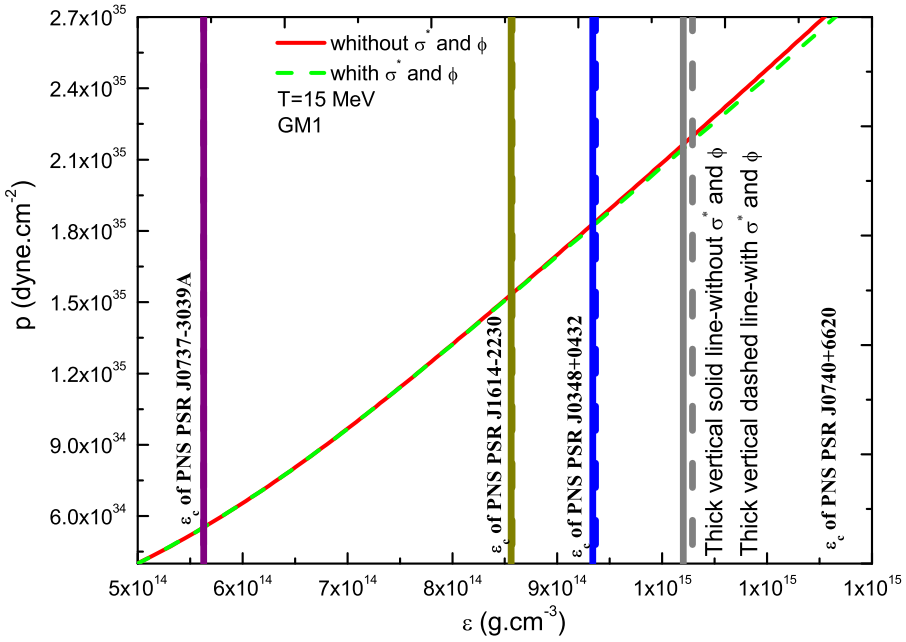

Figure 3. The pressure p of the PNS as a function of the energy density ε. The vertical thick lines mark the central energy densities ε_c of the PNSs for PSR J0740+6620, PSR J0348+0432, PSR J1614–2230, and PSR J0737–3039A, respectively. Solid vertical lines correspond to models without hyperon interactions, and dashed vertical lines correspond to models with hyperon interactions included.

p_c=1.8300 $\times 10^{35}$ dyne.cm^{-2} to p_c=1.8322$\times$ 10^{35} dyne.cm^{-2}, increased by about 0.120%; the central pressures of PNSs PSR J1614-2230 and PSR J0737-3039A respectively are p_c=1.533$\times$ 10^{35}dyne.cm^{-2} and p_c=0.533$\times$ 10^{35} dyne.cm^{-2}, no change. A similar conclusion holds for the central energy density ε_c. From this, we conclude that the larger the mass of the PNS, the greater the increase of the central pressure and the central energy density of the PNS due to the interaction between hyperons; for the PNS with reduced mass, this effect can be ignored.

6. The surface gravitational redshift of PNSs

Figure 4 presents the compactness M/R of the PNS as a function of the central energy density ε_c. The thick vertical lines indicate the central energy densities ε_c corresponding to the PNSs of PSR J0740+6620, PSR J0348+0432, PSR J1614-2230, and PSR J0737-3039A. Among these, the solid vertical lines denote cases without considering hyperon interactions, while the dashed vertical lines

represent cases with hyperon interactions included. It can be observed that the compactness M/R of the PNS increases with rising central energy density ε_c. When hyperon interactions are taken into account, the compactness M/R is reduced.

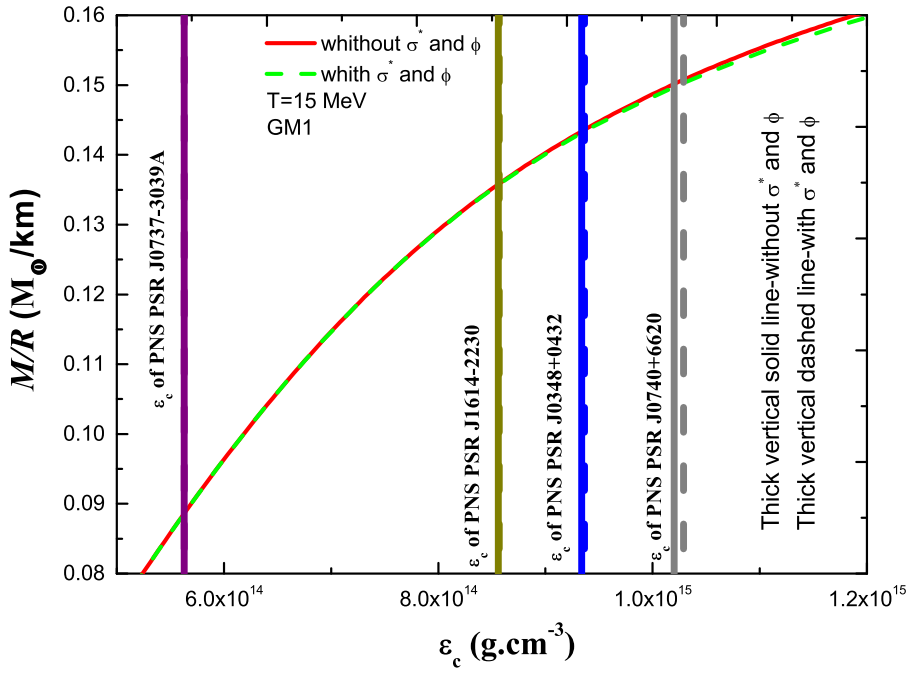

Figure 4. The compactness M/R of the PNS as a function of the central energy density ε_c . The thick vertical lines indicate the central energy densities ε_c of the PNSs corresponding to PSR J0740+6620, PSR J0348+0432, PSR J1614-2230, and PSR J0737-3039A, respectively. The solid vertical lines represent cases without hyperon interactions, while the dashed vertical lines represent cases with hyperon interactions.

Under the mass constraints imposed by the observed pulsars PSR J0740+6620, PSR J0348+0432, PSR J1614-2230, and PSR J0737-3039A, and when hyperon-hyperon interactions are included, the compactness M/R exhibits the following changes: for PSR J0740+6620, it increases from 0.15009 $M_\odot$/km to 0.15019 $M_\odot$/km, a relative increase of approximately 0.067%; for PSR J0348+0432, it increases from 0.14325 $M_\odot$/km to 0.14327 $M_\odot$/km, corresponding to a 0.014% increase. The compactness values for PSR J1614-2230 and PSR J0737-3039A remain unchanged. These results indicate that the effect of hyperon interactions on the compactness is negligible for lower-mass PNSs

Figure 5 shows the surface gravitational redshift z of the PNS as a function of the central energy density ε_c. It can be seen that the surface gravitational redshift z of the PNS increases with the central energy density ε_c. When hyperonic interactions are taken into account, the surface gravitational redshift z of the PNS is reduced at the same central energy density ε_c.

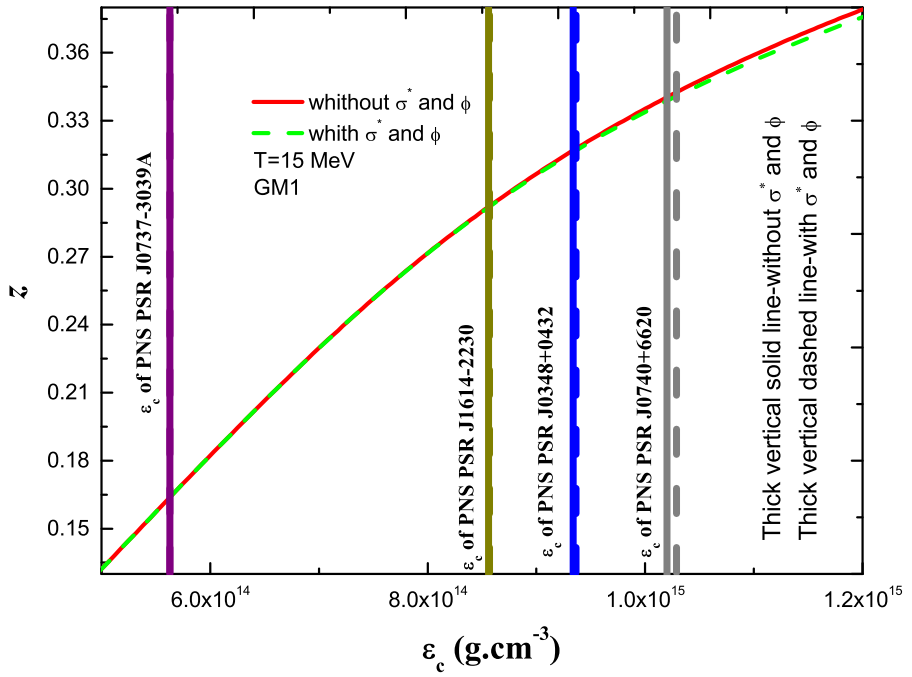

Figure 5. Surface gravitational redshift z of the PNS as a function of central energy density ε_c. The thick vertical lines indicate the central energy densities ε_c for the PNS models of PSR J0740+6620, PSR J0348+0432, PSR J1614-2230, and PSR J0737-3039A, with solid and dashed lines corresponding to models without and with hyperonic interactions, respectively.

Under the constraints of the respective masses of the PNSs PSR J0740+6620, PSR J0348+0432, PSR J1614-2230, and PSR J0737-3039A, and considering the effect of hyperon interactions, the surface gravitational redshift of PSR J0740+6620 decreases from $z = 0.3404$ to $z = 0.3402$, corresponding to a reduction of approximately 0.059%. For PSR J0348+0432, the surface gravitational redshift increases from $z = 0.3168$ to $z = 0.3167$, which is a decrease of about 0.032%. In contrast, the surface gravitational redshifts of PSR J1614-2230 and PSR J0737-3039A remain unchanged. These results indicate that, for

lower-mass PNSs, hyperon interactions have almost no effect on the surface gravitational redshift.

Figure 6 shows the surface gravitational redshift z of the PNS as a function of its radius R . The symbols in the figure correspond to the surface gravitational redshifts of PNSs PSR J0740+6620, PSR J0348+0432, PSR J1614-2230, and PSR J0737-3039A, respectively. Here, solid symbols denote cases without hyperon interactions, while open symbols represent cases with hyperon interactions taken into account. It can be observed that the surface gravitational redshift of a PNS decreases with increasing radius. When hyperon interactions are considered, the surface gravitational redshift for a given radius is reduced.

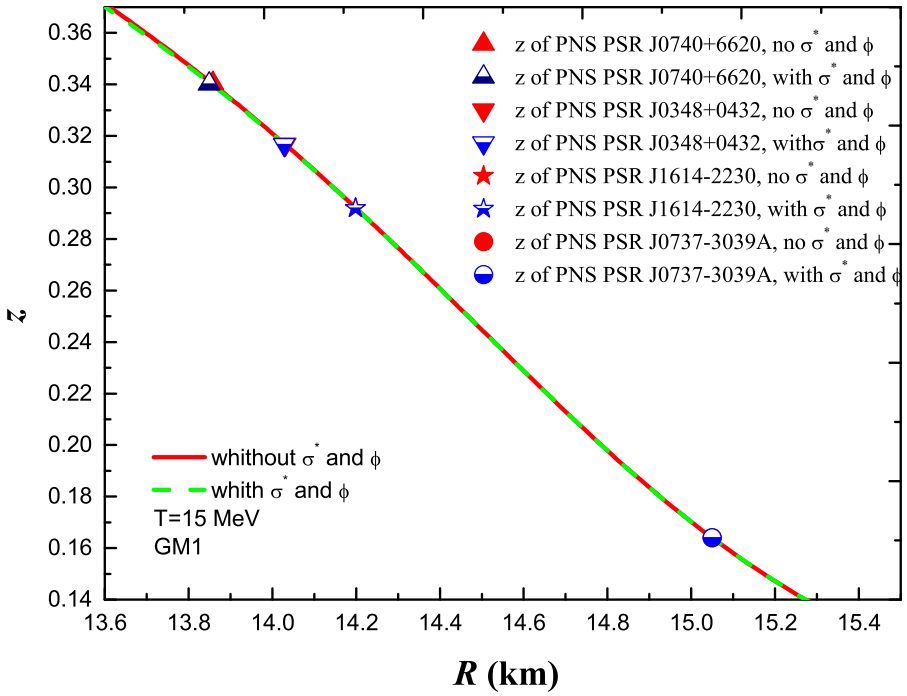

Figure 6. Surface gravitational redshift z of the PNS as a function of radius R . The symbols represent the values for PNSs PSR J0740+6620, PSR J0348+0432, PSR J1614-2230, and PSR J0737-3039A, respectively. Solid symbols correspond to cases without hyperon interactions, while open symbols denote cases with hyperon interactions included.

The surface gravitational redshift z of the PNS as a function of mass M is shown in Fig. 7. The four thick lines correspond to the masses of the PNSs PSR J0740+6620, PSR J0348+0432, PSR J1614-2230, and PSR J0737-3039A,

respectively. The solid red curves represent models without including hyperon interactions, whereas the dashed green curves represent those with hyperon interactions taken into account.

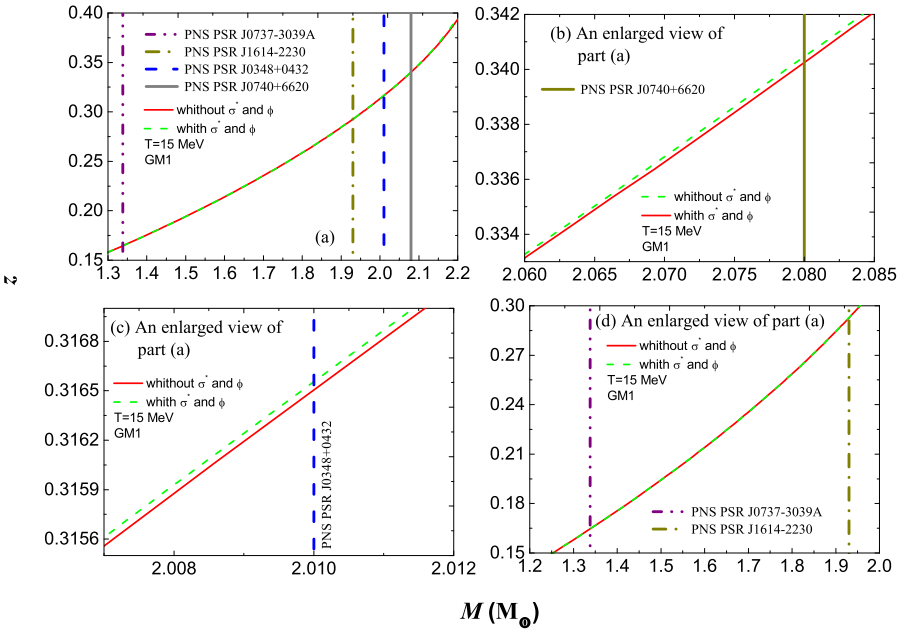

Figure 7. The surface gravitational redshift z of the PNS as a function of mass M. The four thick lines indicate the masses of the PNSs PSR J0740+6620, PSR J0348+0432, PSR J1614-2230, and PSR J0737-3039A, respectively. Solid red curves correspond to models without hyperon interactions, while dashed green curves correspond to models with hyperon interactions included.

From Fig. 7(a), it can be observed that the surface gravitational redshift z of the PNS increases with its mass M. When hyperon interactions are included, the surface gravitational redshift z increases—compared to models with the same mass M—for the PNSs PSR J0740+6620 and PSR J0348+0432 (see Figs. 7(b) and 7(c)). In contrast, the surface gravitational redshift z of the lower-mass PNSs PSR J1614-2230 and PSR J0737-3039A remains essentially unchanged.

7. Summary

In this paper, the effects of hyperon interactions on the surface gravitational redshift z of the PNSs PSR J0740+6620, PSR J0348+0432, PSR J1614-2230,

and PSR J0737-3039A are investigated within the RMF framework. The calculations adopt the nucleon coupling parameter set GM1 and assume a PNS temperature of $T = 15$ MeV.

As can be observed, the pressure p of the PNS increases with the energy density ε. When hyperon interactions are taken into account, the pressure p decreases at a given energy density ε. The increase in both central pressure and central energy density due to hyperon interactions becomes more pronounced for higher PNS masses. In contrast, for lower-mass PNSs, this effect is negligible.

As the central energy density ε_c increases, the mass M, the compactness M/R, and the surface gravitational redshift z of the PNS also increase, whereas its radius R decreases. When hyperon interactions are included, at a given ε_c, the values of M, M/R, and z are reduced.

For the higher-mass PNSs PSR J0740+6620 and PSR J0348+0432, the influence of hyperon interactions on the compactness M/R and the surface gravitational redshift z is significant. In contrast, for the lower-mass PNSs PSR J1614-2230 and PSR J0737-3039A, the effect of hyperon interactions on M/R and z is negligible.

A comprehensive assessment of PNS redshift requires considering rotation and rapid evolution. The current adoption of a static, spherically symmetric model represents a first-order approximation, aimed at focusing on constraining the core EoS. Rotation introduces anisotropy in the redshift and a dependence on the line-of-sight direction (Cadeau et al., 2005; Morsink et al., 2007), while time evolution leads to a significant increase in redshift over time and a 'time-averaging' effect in actual observations. These complex effects will be important directions for our future research.

Acknowledgements. This work was support by the Project of Science and Technology Strategic Cooperation between Nanchong City and SWPU of China (Grant No. SXHZ017), the Project of Science and Technology Strategic Cooperation between Nanchong City and SWPU of China (Grant No. SXHZ036), and the Natural Science Foundation of China (Grant No.12465023).

References

Antoniadis, J., Freire, P. C. C., et al., A Massive Pulsar in a Compact Relativistic Binary. 2013, *Science*, **340**, 448, DOI:10.1126/science.1233232

Batty, C. J., Friedman, E., & Gal, A., Strong interaction physics from hadronic atoms. 1997, *Phys. Rep.*, **287**, 385, DOI:10.1016/S0370-1573(97)00011-2

Burrows, A. & Lattimer, J. M., The Birth of Neutron Stars. 1986, *Astrophysical Journal*, **307**, 178, DOI:10.1086/164405

Cadeau, C., Leahy, D. A., & Morsink, S. M., Pulse Shapes from Rapidly Rotating Neutron Stars: Equatorial Photon Orbits. 2005, *The Astrophysical Journal*, **618**, 451, DOI:10.1086/425857

Chatterjee, D. & Vidana, I., Do hyperons exist in the interior of neutron stars? 2016, *The European Physical Journal A*, **52**, 29, DOI:10.1140/epja/i2016-16029-x

Cromartie, H. T., Fonseca, E., & Ransom, S. M., Relativistic Shapiro delay measurements of an extremely massive millisecond pulsar. 2020, *Nature Astronomy*, **4**, 72, DOI:10.1038/s41550-019-0880-2

Demorest, P. B., Pennucci, T., Ransom, S. M., Roberts, M. S. E., & Hessels, J. W. T., A two-solar-mass neutron star measured using Shapiro delay. 2010, *Nature*, **467**, 1081, DOI:10.1038/nature09466

Deng, Z. L., Li, X. D., & Gao, Z. F., Evolution of LMXBs under Different Magnetic Braking Prescriptions. 2021, *The Astrophysical Journal*, **909**, 174, DOI:10.3847/1538-4357/abe0b2

Ding, W. B., Cai, M. D., & Chan, A. H., The impact of dark matter on neutron stars with antikaon condensations. 2022, *International Journal of Modern Physics A*, **37**, 2250034, DOI:10.1142/S0217751X22500348

Fonseca, E., Pennucci, T. T., Ellis, J. A., et al., The NANOGrav Nine-year Data Set: Mass and Geometric Measurements of Binary Millisecond Pulsa. 2016, *The Astrophysical Journal*, **832**, 167, DOI:10.3847/0004-637X/832/2/167

Fonseca, E., T, C. E., T, P. T., et al., Refined Mass and Geometric Measurements of the High-mass PSR J0740+6620. 2021, *The Astrophysical Journal Letters*, **915**, L12, DOI:10.3847/2041-8213/ac03b8

Gal, A., Hungerford, E. V., & Millener, D. J., Strangeness in nuclear physics. 2016, *Reviews of Modern Physics*, **88**, 035004, DOI:10.1103/RevModPhys.88.035004

Glenden ning, N. K. & Moszkowski, S. A., Reconciliation of neutron-star masses and binding of the Lambda in hypernuclei. 1991, *Physical Review Letters*, **67**, 2414, DOI:10.1103/PhysRevLett.67.2414

Glendenning, N., Hot metastable state of abnormal matter in relativistic nuclear field theory. 1987a, *Nuclear Physics A*, **469**, 600, DOI:10.1016/0375-9474(87)90015-7

Glendenning, N. K., Neutron stars are giant hypernuclei ? 1985, *Astrophysical Journal*, **293**, 470, DOI:10.1086/163253

Glendenning, N. K., Finite temperature metastable matter. 1987b, *Physics Letters B*, **185**, 275, DOI:10.1016/0370-2693(87)90999-3

Glendenning, N. K. 1997 (New York, Inc.: Springer-Verlag)

Harada, T., Hirabayashi, Y., & Umeya, A., Production of doubly strange hypernuclei via Ξ^- doorways in the 16O (K^- ,K^+) reaction at 1.8 GeV/c. 2010, *Physics Letters B*, **690**, 363, DOI:10.1016/j.physletb.2010.05.053

Hempel, M. & Schaffner-Bielich, J., A statistical model for a complete supernova equation of state. 2010, *Nuclear Physics A*, **837**, 210, DOI:10.1016/j.nuclphysa.2010.02.010

Keil, M. T., Raffelt, G. G., & Janka, H. T., Monte Carlo Study of Supernova Neutrino Spectra Formation. 2003, *The Astrophysical Journal*, **590**, 971, DOI:10.1086/375130

Kramer, M., Stairs, I. H., Manchester, R. N., et al., Tests of General Relativity from Timing the Double Pulsar. 2006, *Science*, **314**, 97, DOI:10.1126/science.1132305

Li, Y., Chen, H., Wen, D., & Zhang, J., Constraining the nuclear symmetry energy and properties of the neutron star from GW170817 by Bayesian analysis. 2021, *European Physical Journal A*, **57**, 31, DOI:10.1140/epja/s10050-021-00342-w

Lyne, A. G., Burgay, M., et al., A Double-Pulsar System: A Rare Laboratory for Relativistic Gravity and Plasma Physics. 2004, *Science*, **303**, 1153, DOI:10.1126/science.1094645

Miller, M. C., Lamb, F. K., Dittmann, A. J., et al., PSR J0030+0451 Mass and Radius from NICER Data and Implications for the Properties of Neutron Star Matter. 2019, *The Astrophysical Journal Letters*, **887**, L24, DOI:10.3847/2041-8213/ab50c5

Miller, M. C., Lamb, F. K., Dittmann, A. J., et al., The Radius of PSR J0740+6620 from NICER and XMM-Newton Data. 2021, *The Astrophysical Journal Letters*, **918**, L28, DOI:10.3847/2041-8213/ac089b

Morrison, I. A., Baumgarte, T. W., Shapiro, S. L., et al., The Moment of Inertia of the Binary Pulsar J0737-3039A: Constraining the Nuclear Equation of State. 2004, *The Astrophysical Journal*, **617**, L135, DOI:10.1086/427235

Morsink, S. M., Leahy, D. A., Cadeau, C., et al., The Oblate Schwarzschild Approximation for Light Curves of Rapidly Rotating Neutron Stars. 2007, *The Astrophysical Journal*, **663**, 1244, DOI:10.1086/518648

Mu, X. L., Jia, H. Y., & Zhou, X. 2017, *The Astrophysical Journal*, **846**, 140, DOI:10.3847/1538-4357/aa880c

Oppenheimer, J. R. & Volkoff, G. M., On Massive Neutron Cores. 1939, *Physical Review*, **55**, 374, DOI:10.1103/PhysRev.55.374

Pons, J. A., Reddy, S., Prakash, M., Lattimer, J. M., & Miralles, J. A., Evolution of Proto-Neutron Stars. 1999, *The Astrophysical Journal*, **513**, 780, DOI:10.1086/306889

Riley, T. E., Watts, A. L., Bogdanov, S., et al., A NICER View of PSR J0030+0451: Millisecond Pulsar Parameter Estimation. 2019, *The Astrophysical Journal Letters*, **887**, L21, DOI:10.3847/2041-8213/ab481c

Roberts, L. F., Reddy, S., & Shen, G., Medium modification of the charged-current neutrino opacity and its implications. 2012, *Physical Review C*, **86**, 065803, DOI:10.1103/PhysRevC.86.065803

Romani, R. W., Kandel, D., Filippenko, A. V., et al., PSR J0952-0607: The Fastest and Heaviest Known Galactic Neutron Star. 2022, *The Astrophysical Journal Letters*, **934**, L17, DOI:10.3847/2041-8213/ac8007

Schaffner, J., Dover, C. B., Gal, A., et al., Multiply Strange Nuclear Systems. 1994, *Annals of Physics*, **235**, 35, DOI:10.1006/aphy.1994.1090

Schaffner, J. & Mishustin, I. N., Hyperon-rich matter in neutron stars. 1996, *Physical Review C*, **53**, 1416, DOI:10.1103/PhysRevC.53.1416

Schaffner-Bielich, J. & Gal, A., Properties of strange hadronic matter in bulk and in finite systems. 2000, *Physical Review C*, **62**, 034311, DOI:10.1103/PhysRevC.62.034311

Todd-Rutel, B. G. & Piekarewicz, J., Neutron-Rich Nuclei and Neutron Stars: A New Accurately Calibrated Interaction for the Study of Neutron-Rich Matter. 2005, *Physical Review Letters*, **95**, 122501, DOI:10.1103/PhysRevLett.95.122501

Tolman, R. C., Static Solutions of Einstein's Field Equations for Spheres of Fluid. 1939, *Physical Review*, **55**, 364, DOI:10.1103/PhysRev.55.364

Tolos, L., Centelles, M., & Ramos, A., The Equation of State for the Nucleonic and Hyperonic Core of Neutron Stars. 2017, *Publications of the Astronomical Society of Australia*, **34**, e065, DOI:10.1017/pasa.2017.60

Typel, S. & Wolter, H. H., Relativistic mean field calculations with density-dependent meson-nucleon coupling. 1999, *Nuclear Physics A.*, **656**, 331, DOI:10.1016/S0375-9474(99)00310-3

Weissenborn, S., Chatterjee, D., Schaffner-Bielich, J., et al., Hyperons and massive neutron stars: Vector repulsion and SU(3) symmetry. 2012, *Physical Review C*, **85**, 065802, DOI:10.1103/PhysRevC.85.065802

Zhao, X. F., Constraining the Surface Gravitational Redshift of Proto Neutron Stars with New Nucleon Coupling Constants. 2011, *International Journal of Theoretical Physics*, **50**, 2951, DOI:10.1007/s10773-011-0795-x

Zhao, X. F., The Composition of Baryon in the Proto Neutron Star PSR J0348+0432. 2019, *International Journal of Theoretical Physics*, **58**, 1060, DOI:10.1007/s10773-018-03997-2

Zhao, X. F., Ding, W. B., & Tang, B., Temperature Effects in the Proto Neutron Star Phase of PSR J0740+6620. 2025, *Astrophysics*, **68**, 403, DOI:10.1007/s10511-025-09885-y

Zhou, S. G., Multidimensionally constrained covariant density functional theories-nuclear shapes and potential energy surfaces. 2016, *Physica Scripta*, **91**, 063008, DOI:10.1088/0031-8949/91/6/063008

Contrib. Astron. Obs. Skalnaté Pleso **56/2**, 55 – 81, (2026)
https://doi.org/10.31577/caosp.2026.56.2.55

New variable stars from TESS sectors 77 & 79

A. Dzygunenko[1], N. Telekh[2], K. Liashenko[3], A. Mosiichuk[4], D. Zazubyk[5], D. Tvardovskyi[6], V. Smorodska[6], V. Udovychenko[6], V. Zadubets[6], M. Yatsiuk[7] and V. Boyko[8]

[1] *American Academy in Prague, Kloboučnická 1425/13 str., 14000, Prague, Czech Republic (E-mail: andridzigunenko@gmail.com)*

[2] *III Adam Mickiewicz Secondary School in Katowice, 11 Adama Mickiewicza str., 40-092 Katowice, Poland*

[3] *National Aerospace University "Kharkiv Aviation Institute", 17 Vadym Manko str., 61000 Kharkiv, Ukraine*

[4] *Zhytomyr Higher Professional Technological School, 72 Serhiy Parajanov str., 10001, Zhytomyr, Ukraine*

[5] *Taras Shevchenko National University of Kyiv, 60 Volodymyrska str., 01601, Kyiv, Ukraine*

[6] *Citizen scientist*

[7] *Lyceum 63, 10 Ivan Vyhovsky str., 04136, Kyiv, Ukraine*

[8] *Akhiezer Institute for Theoretical Physics, National Scientific Center, Kharkiv Institute of Physics and Technology, 1 Akademichna str., 61108, Kharkiv, Ukraine*

Received: May 12, 2025; Accepted: December 10, 2025

Abstract. In this research, we conducted a search for new variable stars among recent Transiting Exoplanet Survey Satellite observations. We have chosen data from the 79th sector and a part of the 77th sector. As the main result, we discovered 191 variable stars with a sufficient signal-to-noise ratio that were not classified as variables before. We classified 43 of them and determined the variability period for 89 objects. In addition, we found an object with highly unusual changes in magnitude (TIC 149623590), for which we encourage further investigation. The objective of this project is to attract new citizen scientists to astronomy by conducting simple research under the supervision of more experienced mentors.

Key words: stars – variables: general

1. Introduction

Searching for new variable stars has been an area where both professional and amateur astronomers can contribute. Student-led research has actually shown that meaningful scientific results are possible when participants are guided through real data analysis, for example, with mentors or supervisors. For example, Percy (2006, 2008) described how high school and undergraduate students

successfully carried out variable star projects, applying time-series analysis and even publishing discoveries such as the first red giant pulsating in two modes. More recently, Chisabi et al. (2025) reported on a student project regarding pulsar timing following a MeerKAT workshop.

Citizen-science projects also demonstrate what is possible when professionals and volunteers work together, as demonstrated by Kostov et al. (2025) in the case of the Transiting Exoplanet Survey Satellite Ricker et al. (2015) TESS Ten Thousand catalog of eclipsing binaries. Our project is much smaller in scale, but these examples show that with proper guidance and checking, contributions from non-professionals can still be reliable and scientifically useful.

Professional surveys have also used TESS data and other archives to expand the known population of variables. Zhou (2025) identified over 11,000 new δ Scuti and γ Doradus stars through systematic light-curve inspection. This paper also shows the use of visual inspection and period analysis; these methods remain effective approaches even in large-scale research.

Our work continues this tradition within a student-driven framework. The research project was designed to involve students and amateur astronomers in astronomical research by guiding them through a structured study. The main objective of the research is to find new variable stars among observations from the TESS space telescope in sectors 77 and 79. In this way, our project connects the educational potential of student research with the previous methodologies of professional surveys.

TESS[1] is a NASA & MIT space mission launched in 2018 to boost the search for exoplanets across the entire sky. TESS has an unusually large and elongated field of view (24 by 96 degrees), which constitutes a single sector of observations. Each sector is continuously observed during 27.4 days, usually with a single 2-4 day gap in the middle of this period. The observations were performed using the 2-minute short cadence (SC) mode for pre-selected targets, which provides $\approx 16,000$ data points (frames) per target per sector. The entire sky is divided into 31 sectors: 13 for each hemisphere and 5 along the ecliptic. More technical details about TESS are presented in Ricker et al. (2015).

The data from this space observatory is also actively used in other branches of astronomy, most notably in asteroseismology, which was suggested even prior to its launch in Campante et al. (2016). Later research, for example Antoci et al. (2019) and Prša et al. (2022) focusing on the eclipsing binaries, undoubtedly confirmed that suggestion.

We decided to use it for the search for new variable stars, as this process is quite simple and does not require years of studying astronomy. Nevertheless, students must have enough knowledge about the subject to be able to conduct the research. Since they have no prior experience of such research, we prepared a series of educational videos and supplementary text materials. They cover the definitions, physical processes, classification, and some aspects of the research

[1] https://tess.mit.edu/observations/

methods. In total, 10 students managed to finish the educational part and join the research itself.

2. Methods and algorithms

In this section, we describe the details of our research methods and software. This project is the second in our student-led research series, and the methodology follows closely from our previous study Dzygunenko et al. (2026), with some minor updates. While the general algorithm is briefly summarized here, we also include new procedures for identifying potential exoplanet transits, which were not considered in the earlier project.

2.1. General procedure

The procedure for each star consisted of the following steps:

1. Check if the star shows any signs of variability on its light curve and if it is astrophysical variability or a non-astrophysical variability in TESS data. A common solution is to perform aperture photometry from the target pixel files.

2. If a star is variable, check if its variability was detected earlier by someone. First, we checked the database SIMBAD and the AAVSO VSX (The International Variable Star Index) catalog, then all available articles about each star. If neither SIMBAD, VSX, nor NASA ADS contains any mentions of variability for this star, we considered it a newly discovered one.

3. If the star is periodic, we tried to estimate its period using the Lomb-Scargle periodogram, implemented in our Python code.

4. If a star is an eclipsing binary, we classified it "by eye," since those variability types are not numerous and are usually easy to distinguish. The "By eye" classification refers to visually identifying the three main types of eclipsing binaries based on the morphology of the light curves: (i) EA (Algol-type) systems show sharp, well-separated eclipses with flat/almost flat intervals in between; (ii) EB (β Lyrae-type) systems exhibit continuous brightness variation with no flat sections due to tidal distortion; and (iii) EW (W UMa-type) systems have short periods and nearly equal, sinusoidal eclipses due to the stars being in contact.

5. If we suspect an exoplanet orbiting around the star, we apply several vetting methods to rule out false positives. They include analyzing aperture masks, pixel-level light curves, centroid motion, background flux variations, and specialized algorithms like TessCentroidVetting.

6. For pulsating variable stars, we first evaluated whether a star could plausibly belong to this class by estimating its absolute magnitude and spectral type. If the parameters matched those typical of known pulsating variables, we then examined whether the observed period, amplitude, and overall light curve shape were consistent with any specific type. As illustrated in Fig. 1, the location of the new variable star TIC 141985410 on the Hertzsprung-Russell diagram confirms its classification as a DSCT (δ Scuti) variable. The source of this figure [2].

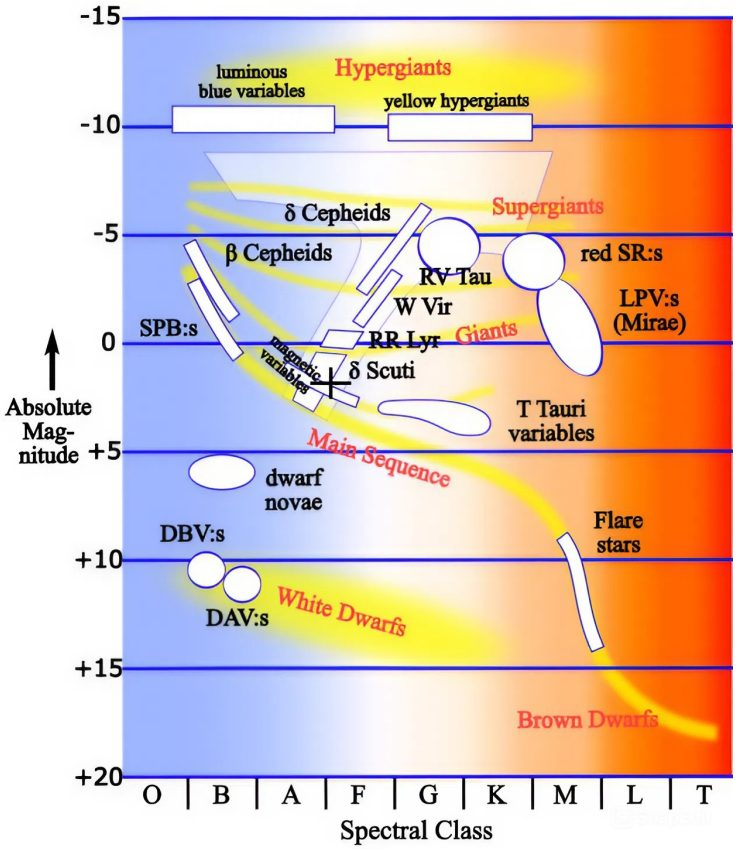

Figure 1. The location of the new variable star TIC 141985410 on the Hertzsprung-Russell diagram, indicated with a + sign.

[2]https://en.wikipedia.org/wiki/Variable_star/media/File:HR-vartype.svg

2.2. Search for exoplanets

Exoplanet transits are a type of variability that was not present in our previous research due to a much smaller number of stars we studied. In this study, we detected 6 light curves, which could be interpreted as exoplanet transits. Despite that, we could not claim a new exoplanet outright because we had to make some checks first. To distinguish real exoplanet transits from false positives, we used the following algorithm, illustrated by TIC 237280203 (Figs. 2 - 7):

1. **Aperture mask analysis.** We examined the authorized aperture masks to ensure the transit signal originates from the target star and not a nearby contaminating source (Fig. 3). Inconsistent transit depths between different masks may indicate a blended eclipsing binary. We used the software developed by Nora Eisner from October 15, 2021 [3], the lightkurve package was used as well [4].

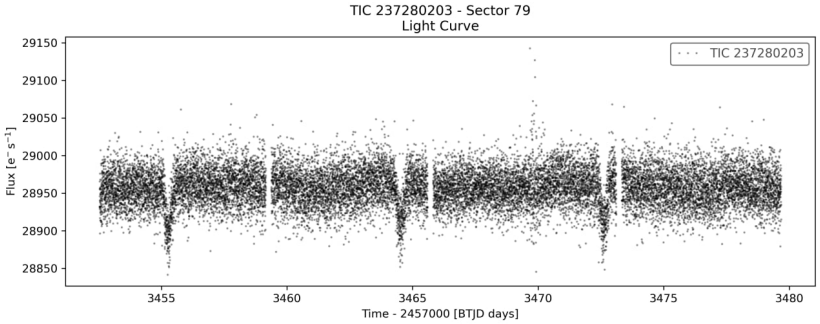

Figure 2. TIC 237280203 as an example for illustration of the algorithm steps.

2. **Pixel-level light curves.** By extracting light curves for each pixel in the target's vicinity, we checked whether the transit signal appears only in the target's pixels (Fig. 4). Dips in neighboring pixels suggest a background eclipsing binary or an instrumental artifact. We used the software developed by Nora Eisner from October 15, 2021 [5].

3. **Centroid motion and satellite motion.** We tracked the position of the brightest pixel during transit events (Fig. 5). Significant centroid shifts imply an off-target origin, such as a nearby eclipsing binary or a moving solar system object. This method was developed by Joseph Twicken and described in Twicken (2019).

[3] https://github.com/noraeisner/PH_Coffee_Chat
[4] https://github.com/lightkurve/lightkurve
[5] https://github.com/noraeisner/PH_Coffee_Chat

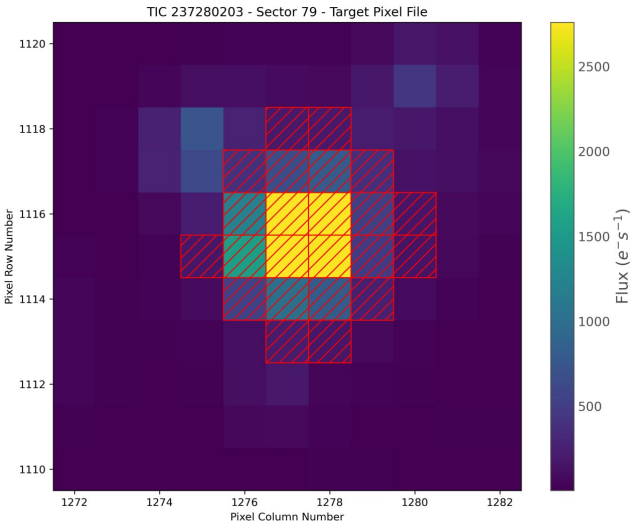

Figure 3. Aperture mask analysis for TIC 237280203. The object is located at the center of the image and corresponds to four yellow pixels.

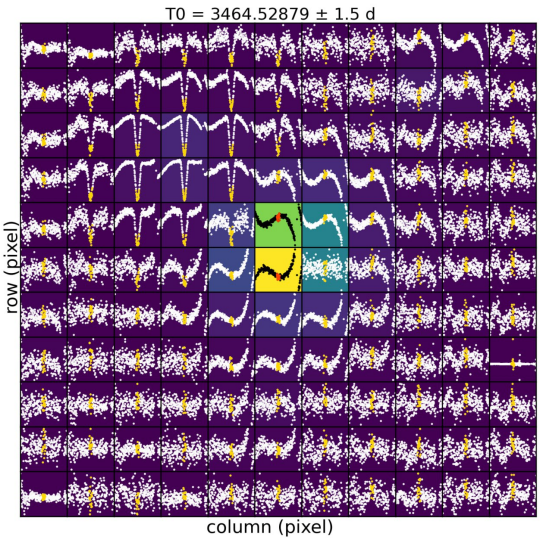

Figure 4. Pixel-level light curves for TIC 237280203. The code computes the flux changes for each individual pixel within close vicinity of the selected object. A group of pixels to the upper left from the center shows clear signs of a background eclipsing binary.

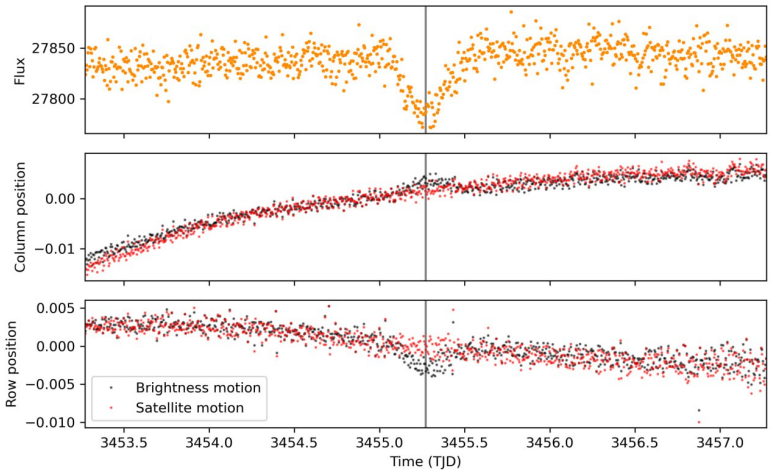

Figure 5. Centroid motion and satellite motion for TIC 237280203. The code analyzes how the position of the brightest pixel shifts along the X-axis (middle panel) and Y-axis (bottom panel) around the timing of a transit (top panel).

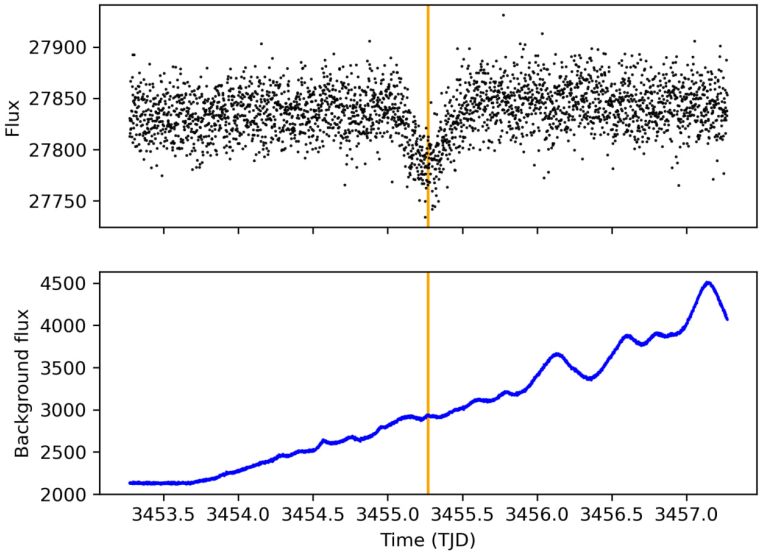

Figure 6. Background flux monitoring for TIC 237280203. In this case the background noise is within the appropriate range.

4. **Background flux monitoring.** Sudden spikes in background flux during transit-like events may indicate contamination from passing solar system objects or scattered light, which could mimic planetary transits (Fig. 6). We used software, developed by Nora Eisner from October 15, 2021 [6].

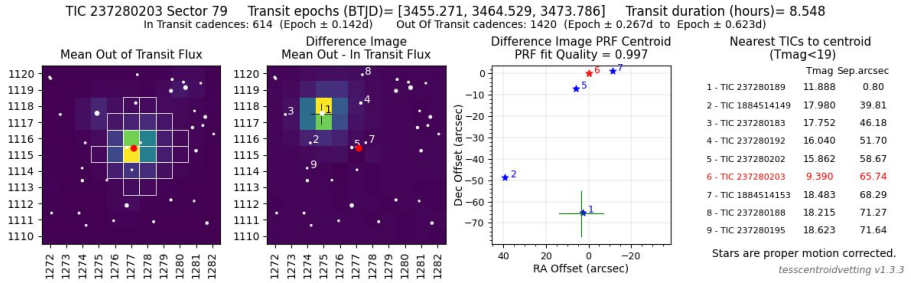

Figure 7. Automated vetting for TIC 237280203.

5. **Automated vetting with TessCentroidVetting.** This algorithm quantitatively evaluates centroid motion during transits, providing statistical confidence in the on-target nature of the signal (see Fig. 7). We used the software "TESS centroid vetting," developed by Rafael Rodrigues and Sam Lee, version 1.3.3. from October 4, 2024 [7].

   However, the periodic dimming can be caused by a stellar spot on the rotating stellar surface. In this case the only tool to determine could be measuring the radial velocities.

Through this multi-stage vetting process, 4 objects out of 6 were confirmed to be false positives (FP). There are background eclipsing binaries (TIC 229458129, TIC 233604585, TIC 237277754, and TIC 237280203). The fifth target (TIC 1400824435) most likely is an eclipsing binary itself because the depth of eclipses on its light curve alternates slightly. The sixth and final signal (TIC 149623590) appears to be of unknown origin and requires further investigation.

2.3. TIC 149623590

TIC 149623590 was by far the most unusual of all variable stars we discovered. It resembles either an exoplanet transit or an Algol-type eclipsing binary with secondary minima not visible due to the gaps in the data (see Fig.8). However, the two minima we could see are significantly asymmetric, which is not typical for both types.

[6] https://github.com/noraeisner/PH_Coffee_Chat
[7] https://github.com/exo-pt/TESS-Centroid_vetting

In total, two minima (T_0=3454.40943 BTJD and T_0=3468.31511 BTJD) were recorded, to which we applied the multi-stage vetting process described in detail in Sec. 2.2, in order to determine whether these signals were caused by astrophysical variability or by systemic trends of the TESS telescope or background flux (e.g., light reflected from the Earth's atmosphere or from objects in our solar system).

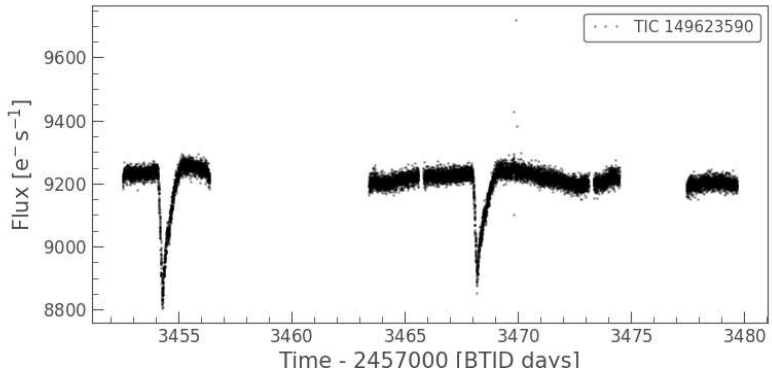

Figure 8. The light curve of the TIC 149623590 in the 79th sector of the TESS observations.

As illustrated in Fig. 9, the photometric aperture fully covers the pixels containing the maximum stellar flux (where our target star is located) and extends to capture several neighboring pixels.

While a background eclipsing binary would typically appear as sinusoidal spikes concentrated within a localized group of pixels, and an object crossing TESS's field of view in the Solar System would show flat-bottomed drops localized to a pixel cluster, Fig. 10 shows that spikes are observed across the entire Target Pixel File (TPF) region, encompassing both the target and the surrounding field. This widespread variability is difficult to reconcile with a purely astrophysical source without additional data.

To investigate the possibility of an instrumental uncertainty, we tracked the centroid during both observed minima (Figs. 11–12). The upper panels of Figs. 11–12 show the asymmetrical shape of the minima in the target flux, while the lower panels display a maximum in brightness motion that corresponds to the time of the star's minima. The same pattern is seen in Figs. 13-14, where we monitored a background flux for both minima, confirming that the signal is originating across the entire TPF area, rather than being isolated to the target aperture.

Finally, the automated vetting procedure shows a gradient in the difference images and formally identified a TIC 149623587 as the source of the signal within

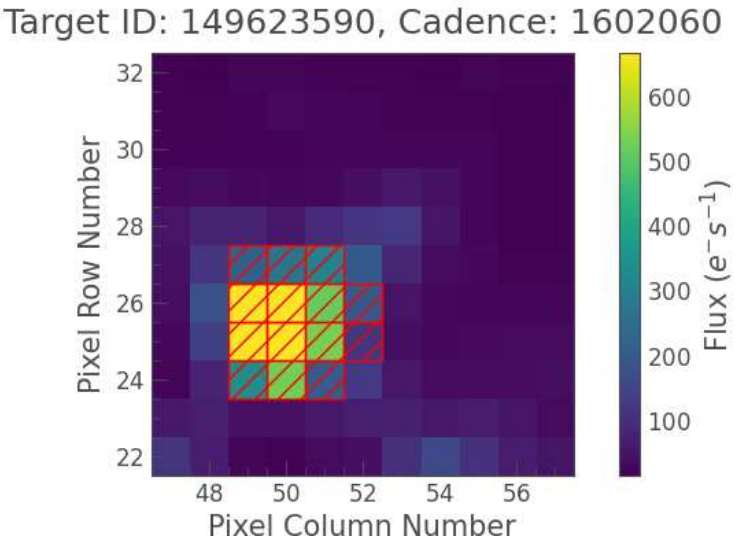

Figure 9. Aperture mask analysis for TIC 149623590. The object is located closer to the left edge of the image and corresponds to four of the brightest yellow pixels.

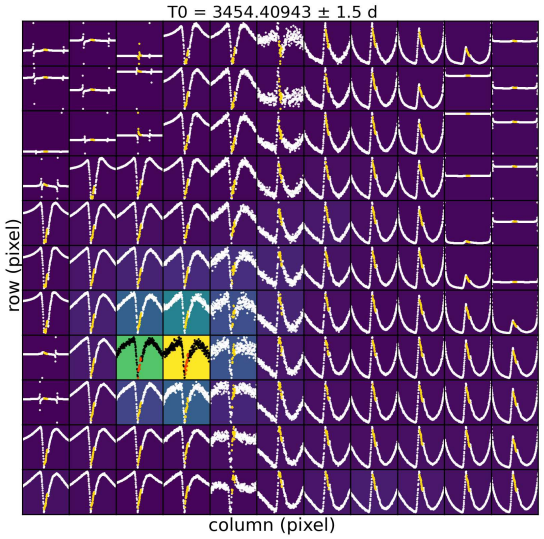

Figure 10. Pixel-level light curves for TIC 149623590. The code computes the flux changes for each individual pixel within close vicinity of the selected object. A whole pixel file shows clear signs of a background source of the signal.

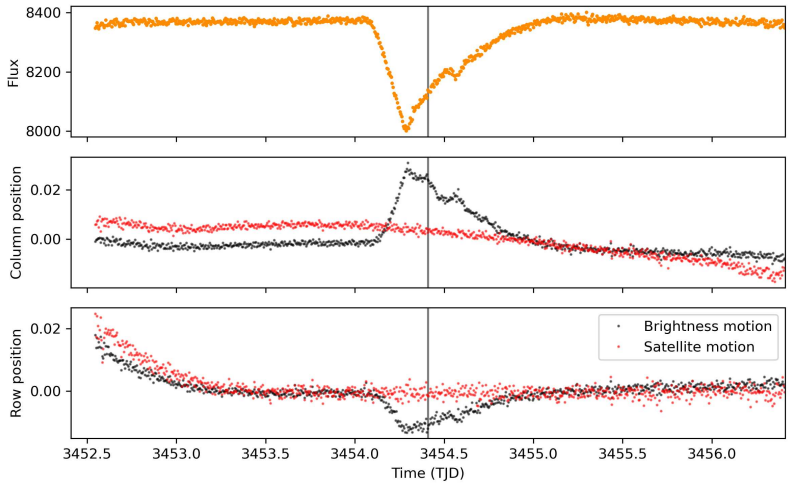

Figure 11. Centroid motion and satellite motion analysis for signal T_0=3454.40943 BTJD on the light curve of TIC 149623590. The code analyzes how the position of the brightest pixel shifts along the X-axis (middle panel) and Y-axis (bottom panel) around the timing of a transit (top panel).

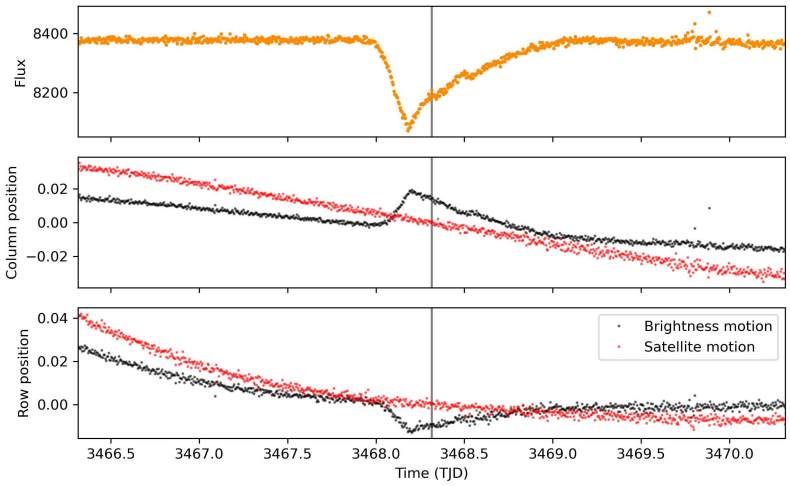

Figure 12. Centroid motion and satellite motion analysis for signal T_0=3468.31511 BTJD on the light curve of TIC 149623590. The code analyzes how the position of the brightest pixel shifts along the X-axis (middle panel) and Y-axis (bottom panel) around the timing of a transit (top panel).

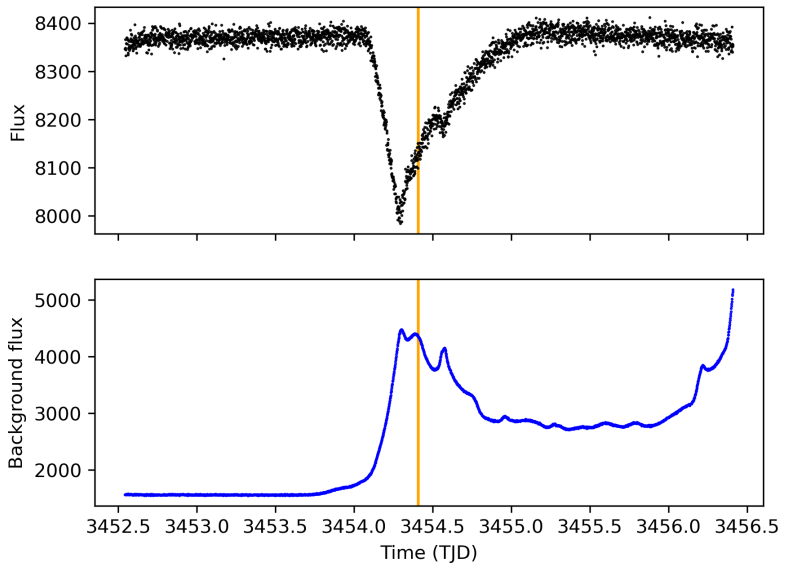

Figure 13. Background flux monitoring for signal T_0=3454.40943 BTJD on the light curve of TIC 149623590.

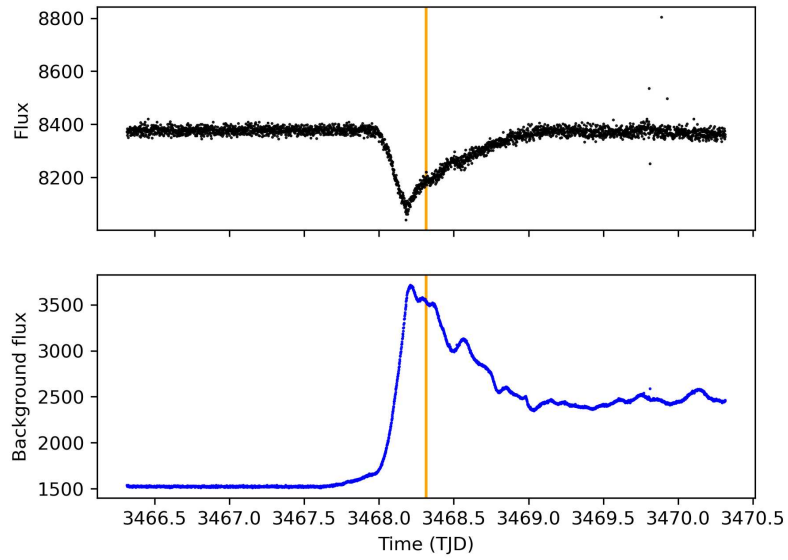

Figure 14. Background flux monitoring for signal T_0=3468.31511 BTJD on the light curve of TIC 149623590.

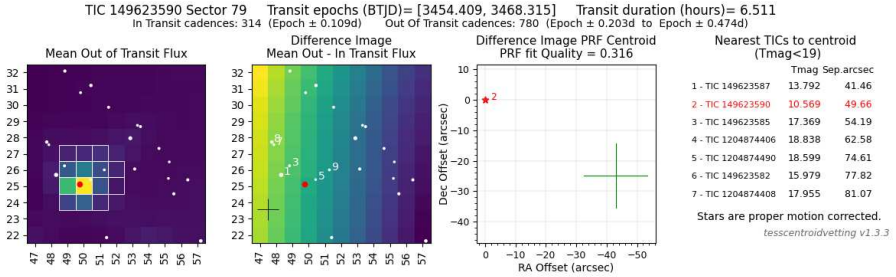

Figure 15. Automated vetting for TIC 149623590.

the TPF. Since there are no other bright variable objects near this star that could cause this complex artifact, we question the reliability of the automated check results, and the source of these minima remains uncertain.

No publicly available spectroscopic observations were found for this object, as well as no additional photometric observations. Thus, we cannot yet determine the type of the object accurately. Moreover, we cannot completely rule out the possibility of an exoplanet or an eclipsing binary system, or that asymmetry is caused by a protoplanetary or accretion disk, since neither of our tests definitively disproved this hypothesis. This object is certainly worth further study, which may lead to noticeable future discoveries.

3. Results

3.1. General table

As the main result, we present a table with 191 newly found variable stars (see Table 1). We managed to calculate periods of 89 of them and estimate classification of 43 objects. If a period is marked as >27, it indicates that the full variability cycle does not fit within a single TESS sector (27.4 days). The asterisk next to the variability type means that the classification for this star is uncertain.

Table 1. List of 191 newly discovered variable stars. The corresponding light curves are displayed in the Appendix (Figs. 16-23). Footnotes elaborate the variability types upon their first appearance in the table.

TIC ID	Variability type	Period	TIC ID	Variability type	Period
7584971	unknown[8]		148049214	DSCT[9]	0.03405
7617177	unknown		148073753	DCEPS[10]	3.87633
7857074	unknown		148119656	unknown	
8347908	unknown	2.12165	148165057	unknown	
9530168	unknown		149690708	unknown	2.65301
10363353	unknown		149693058	unknown	
10473978	unknown	0.3	149736629	unknown	
10491567	unknown		149737192	unknown	
10792081	unknown		149793837	unknown	
11061881	unknown		150486675	unknown	
21028309	unknown		154340851	unknown	
21633694	RRAB[11]	0.33813	154660474	unknown	2.91772
21634379	unknown		154700607	RRD[12]	2.31921
21831633	unknown		154742877	unknown	3.3988
21856856	unknown		154810900	unknown	2.00377
22040779	unknown		154867969	unknown	
22110165	unknown		154874139	unknown	
22113313	unknown		154874588	unknown	5.68367
43276438	CWB[13]	4.07195	229406488	CWB	4.06823
43734727	CWB	5.07478	229458129	FP[14]	1.59619
43794987	unknown	3.60383	229589801	unknown	
43797951	RRD	1.11667	229608810	EA[15]	3.57035
43798687	unknown	1.20601	230137379	RR[16]	1.97426
43870800	unknown		230197161	unknown	6.28467
43908172	DCEPS	5.32061	232529657	unknown	0.8327
44187228	unknown	1.39155	232609078	unknown	
44188129	unknown		232616284	unknown	2.1653
44190078	EA	11.05	233087496	CWA[17]	8.05697

[8]Impossible to definitively identify the variability type.
[9]δ Scuti-type pulsating variable.
[10]δ Cephei-type pulsating variable.
[11]RR Lyrae type pulsating variable, subtype AB.
[12]RR Lyrae-type pulsating variable, subtype D.
[13]BL Herculis-type stars, a subtype of W Virginis variables.
[14]False positive: an exoplanet transit-like signal, but not an exoplanet after further inspection.
[15]β Persei-type eclipsing binary.
[16]RR Lyrae-type pulsating variable, subtype unknown.
[17]W Virginis-type variable star.

Table 1. Continued.

TIC ID	Variability type	Period	TIC ID	Variability type	Period
44267585	EA	>27	233098381	unknown	2.41891
44270304	DSCT*[18]	0.34392	233120677	unknown	1.04069
44386100	unknown	1.45108	233125012	unknown	
44386592	unknown	1.77354	233199626	unknown	10.74
75625642	RR	4.62289	233373166	unknown	
75652037	unknown		233394432	RRC[19]	
75727889	unknown	5.29078	233497034	unknown	
75832705	unknown		233508020	unknown	
75963868	unknown		233526133	unknown	
76138761	unknown	1.88384	233539654	CWB	4.13077
76143193	unknown		233573215	unknown	0.76934
76196131	unknown		233603364	EB[20]	6.62956
82359031	unknown		233604585	FP	3.14164
82408526	unknown		233616650	unknown	1.83426
82599979	unknown		233628452	DSCT	0.36434
82611261	unknown	7.33256	233631689	unknown	
85511656	unknown	1.80732	233633066	DSCT	0.10513
85743873	unknown		233650118	unknown	4.04771
88840705	unknown		233730340	unknown	
88877401	unknown		233790846	unknown	
88995742	unknown		235596189	unknown	
99543677	unknown		235711657	unknown	7.7032
101675157	unknown	5.21821	235712705	unknown	
102988612	unknown		235947146	unknown	
103096562	unknown	1.22781	235980310	unknown	
103179478	unknown		236001714	CWB	6.40481
103194937	unknown		236010034	unknown	5.2
103508168	unknown	1.42066	236013234	unknown	
103565392	unknown		236393296	unknown	
115183789	unknown	2.04017	236750863	unknown	
115288430	unknown		236752232	unknown	
115611128	unknown	0.88966	236770582	RRC	4.86927
116048705	unknown		237119483	unknown	
116097246	unknown		237132577	unknown	
116126490	unknown		237133525	unknown	
116164903	unknown		237277754	FP	0.7048

[18] An asterisk means classification is uncertain.
[19] RR Lyrae-type pulsating variable, subtype C.
[20] β Lyrae-type eclipsing binary.

Table 1. Continued.

TIC ID	Variability type	Period	TIC ID	Variability type	Period
116241468	RR	0.87532	237280203	FP	9.23
122789619	unknown	1.71742	237285047	unknown	
122890144	unknown		243335760	unknown	
123091906	unknown		416053615	SRs[21]	8.02145
137083163	unknown		416099134	unknown	7.33382
137086255	unknown	0.52792	416102581	DSCT	0.06352
137479673	unknown		416120082	unknown	
137995653	RVA*[22]	2.55983	416124077	unknown	
138026606	DCEPS	4.23973	416125133	RR	2.61754
138046660	unknown	2.94937	417617028	unknown	
138107363	RRC		417620193	unknown	
138108399	unknown	1.67503	417703706	RRD	0.5424
138121408	unknown		417746470	unknown	
138471905	DCEP	9.69081	418111831	unknown	2.51609
140737856	unknown	9.3567	418372012	unknown	
141533678	unknown		420456245	unknown	
141917304	unknown		420536861	unknown	
141950998	unknown		420729120	unknown	
141983134	unknown	1.09414	420801643	unknown	
141985410	DSCT	0.05264	423029433	unknown	
142010247	unknown		424731804	unknown	2.85634
142043413	unknown	0.75373	427029032	unknown	
142677896	RRC	0.3293	428772395	RR	1.11988
143036407	unknown	3.0318	428888603	unknown	
143062447	RR	2.26121	435741597	unknown	
143100422	unknown	1.40594	435741713	CWB	4.07405
143162957	unknown		441720037	unknown	2.95963
143185397	unknown		441789740	unknown	
143185490	unknown	2.60911	441808062	unknown	4.0682
147716003	unknown		1400824435	EB	2.16605
147751796	unknown		149623590	unknown	
147752402	CWB	3.08347			

[21] Semi-regular variable star.

[22] RV Tauri-type variable, subtype A.

3.2. Period uncertainty estimation

To roughly estimate uncertainty s of our calculations for the period, we conducted a test. This test involved creating artificial datasets, similar to TESS observations: sine waves with a random amplitude, period, and noise. Each dataset is exactly 1 sector (27.4 days) long with a 2-5 day gap in the middle and a 2-minute interval between data points. The period of the sine wave was in the range from 0.1 to 50 days. In total, we generated 500 TESS-like sectors. We ran each of them through the Lomb-Scargle algorithm to compute the period and calculate the percentage difference between real and calculated periods.

As a result, we have realized that accuracy decreases rapidly for longer periods, since fewer and fewer sine waves could fit into a single sector. For example, stars with periods less than 2 days have typical uncertainty of 0.005-0.1%. Stars with periods of 2-10 days have uncertainty s of about 0.1-0.6%. With a period approaching the duration of a sector (27.4 days), uncertainty increases to 0.8-1.2%, and for periods of 40-50 days, uncertainty could reach as much as 3%, which is an inappropriately large uncertainty for variable stars. We note that the calculated uncertainty do not decrease with an increasing number of points on the Lomb-Scargle diagram after a certain point. We have tested 1000, 3000 and 10 000 points per diagram, giving us almost the same results.

4. Discussion and Conclusions

The main purpose of this research was educational. We trained students to work with real TESS data. They watched specially prepared videos about basic aspects of variable stars and their research, read our manuals, and practiced with already classified light curves before working with new observations. More experienced researchers supervised their progress and checked the results. Students also could use obtained knowledge in their future research. However, the dropout rate during the initial stages was much higher than expected, which made us review our approach to teaching.

From a scientific perspective, we also faced several challenges. The first was to quickly search across hundreds of stars viewed by students. We had to confirm that all objects they marked as "new variable stars" are indeed new and variable, which appeared to be easier said than done. We checked the variability of the stars manually by analyzing their light curves. We excluded light curves with very high noise and only accepted those with a clear and reliable signal. For the other part, we made a code in Python, which searches for keywords related to variable stars in articles and in SIMBAD and AAVSO VSX for each star. It significantly reduced the amount of time and effort required for the process. In total, over 300 claimed stars were rejected because of either having a too low signal-to-noise ratio or being discovered previously. We also found out that if an article indexed in NASA ADS is not yet connected to SIMBAD, it may lead to a temporary mismatch in the classification and repetitive discoveries.

The second tough challenge was classification. While eclipsing binaries were easy to classify, pulsating variables proved to be anything but. Since we were limited to using only light curves and radial velocities were not available for the vast majority of the stars, we were not able to classify more than half of the stars at all. Many types of pulsating stars have similar light curves; moreover, their shapes also match some types of rotating variable stars. To avoid providing a false classification, we tried to check if a star at least could be a pulsating variable. We used tools such as the Hertzsprung–Russell diagram along with established formulas—Ballesteros' for temperature and Pogson's for magnitude—to improve our confidence in classifying variable stars. Although it helped, the classification of pulsating stars remained especially challenging, and some uncertainty remains. To avoid misleading further research, any star whose light curve and corresponding parameters did not clearly match established types was marked as unknown. The total number of stars marked as unknown is 148.

Based on our experience, attracting new students to astronomy using simple research is possible and quite efficient, considering the moderate amount of effort it required. The project successfully joined scientific research with education by giving students hands-on experience with real TESS data—from detecting variability to validating classifications. However, both the educational part and the actual research should be improved for the future projects. Using semi-automated tools could help measure important features of the light curves while still allowing for manual checks. Although our method was partially manual, it yielded significant new data for the astronomical community for further analysis and use. Overall, while our current semi-automated method was successful for analyzing periodic variable stars, improving our approach will be important to increase both accuracy and the variety of objects we could study.

Acknowledgements. This paper includes data collected with the TESS mission, obtained from the MAST data archive at the Space Telescope Science Institute (STScl). Funding for the TESS mission is provided by the NASA Explorer Program. STScl is operated by the Association of Universities for Research in Astronomy, Inc., under NASA contract NAS 5-26555. This research was conducted as the first part of the TESS-UA-2024 research project for young scientists, organized by the Clear Skies Foundation.

References

Antoci, V., Cunha, M. S., Bowman, D. M., et al., The first view of δ Scuti and γ Doradus stars with the TESS mission. 2019, *Monthly Notices of the RAS*, **490**, 4040, DOI:10.1093/mnras/stz2787

Campante, T. L., Schofield, M., Kuszlewicz, J. S., et al., The Asteroseismic Potential of TESS: Exoplanet-host Stars. 2016, *Astrophysical Journal*, **830**, 138, DOI:10.3847/0004-637X/830/2/138

Chisabi, M., Andrianomena, S., Enwelum, U., et al., Timing and noise analysis of five millisecond pulsars observed with MeerKAT. 2025, *Monthly Notices of the Royal Astronomical Society*, **537**, 2462, DOI:10.1093/mnras/staf100

Dzygunenko, A., Yatsiuk, M., Popenko, M., et al., New variable stars from TESS sector 86. 2026, *Journal of Physical Studies*, **30**, 1901, DOI:10.30970/jps.30.1901

Kostov, V. B., Powell, B. P., Fornear, A. U., et al., The TESS Ten Thousand Catalog: 10,001 Uniformly Vetted and Validated Eclipsing Binary Stars Detected in Full-frame Image Data by Machine Learning and Analyzed by Citizen Scientists. 2025, *The Astrophysical Journal Supplement Series*, **279**, 50, DOI:10.3847/1538-4365/ade2d8

Percy, J. R., Variable Star Research Projects for Outstanding Senior High School Students. 2006, *Journal of the American Association of Variable Star Observers*, **35**, 284

Percy, J. R., Variable Star Research Experiences for High School Students, Undergraduates, and Amateur Astronomers. 2008, in Astronomical Society of the Pacific Conference Series, Vol. **400**, *Preparing for the 2009 International Year of Astronomy: A Hands-On Symposium*, ed. M. G. Gibbs, J. Barnes, J. G. Manning, & B. Partridge, 363

Prša, A., Kochoska, A., Conroy, K. E., et al., TESS Eclipsing Binary Stars. I. Short-cadence Observations of 4584 Eclipsing Binaries in Sectors 1-26. 2022, *The Astrophysical Journal Supplement Series*, **258**, 22, DOI:10.3847/1538-4365/ac324a

Ricker, G. R., Winn, J. N., Vanderspek, R., et al., Transiting Exoplanet Survey Satellite (TESS). 2015, *Journal of Astronomical Telescopes, Instruments, and Systems*, **1**, 014003, DOI:10.1117/1.JATIS.1.1.014003

Twicken, J. 2019, Data Validation: Difference Imaging and Centroid Analysis, https://ntrs.nasa.gov/api/citations/20190029148/downloads/20190029148.pdf, [Online; accessed 10-December-2025]

Zhou, A.-Y., Variability Census of Legacy Catalogs. V. 11,820+ New δ Scuti and γ Doradus Stars. 2025, *Research Notes of the AAS*, **9**, 145, DOI:10.3847/2515-5172/ade301

A. Light curves of newly identified variable stars

All TESS light curves for the 191 newly identified variable stars are shown below. Each figure presents a grid of 24 light curves (8×3), labeled with TIC IDs above each panel. The numbers in the captions indicate the object index range corresponding to Table 1.

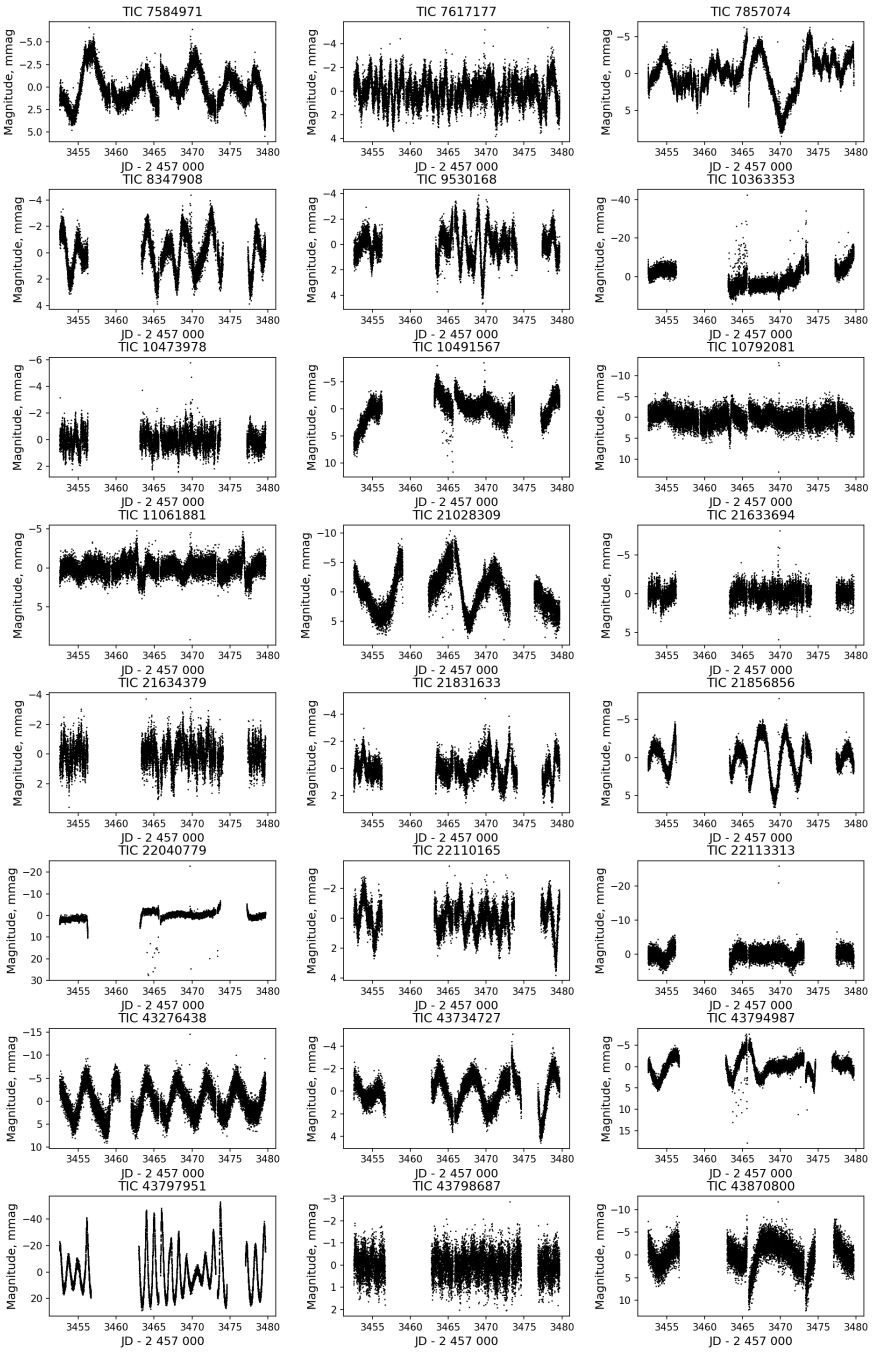

Figure 16. Grid of light curves for objects 1–24.

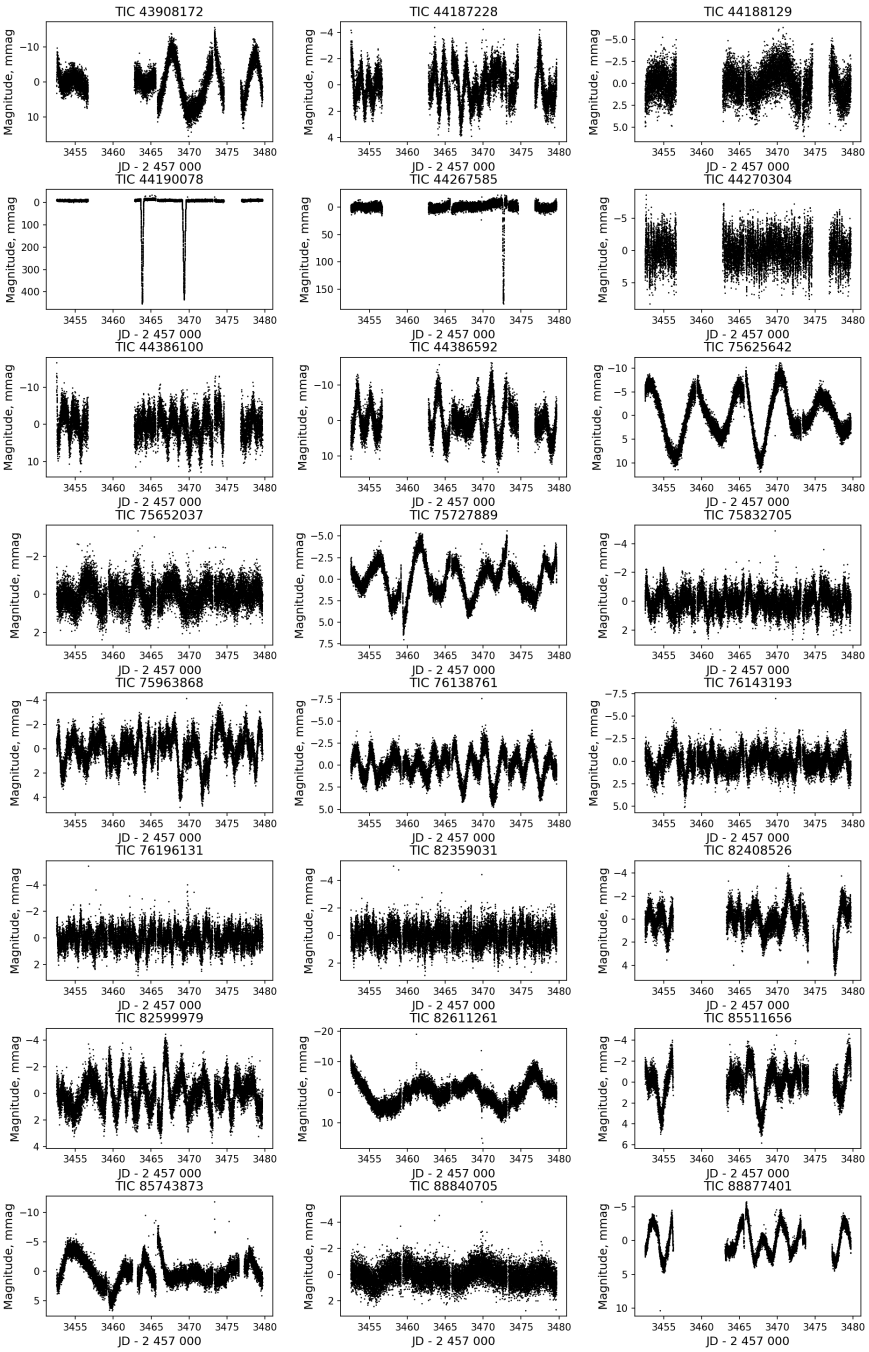

Figure 17. Grid of light curves for objects 25–48. Continued.

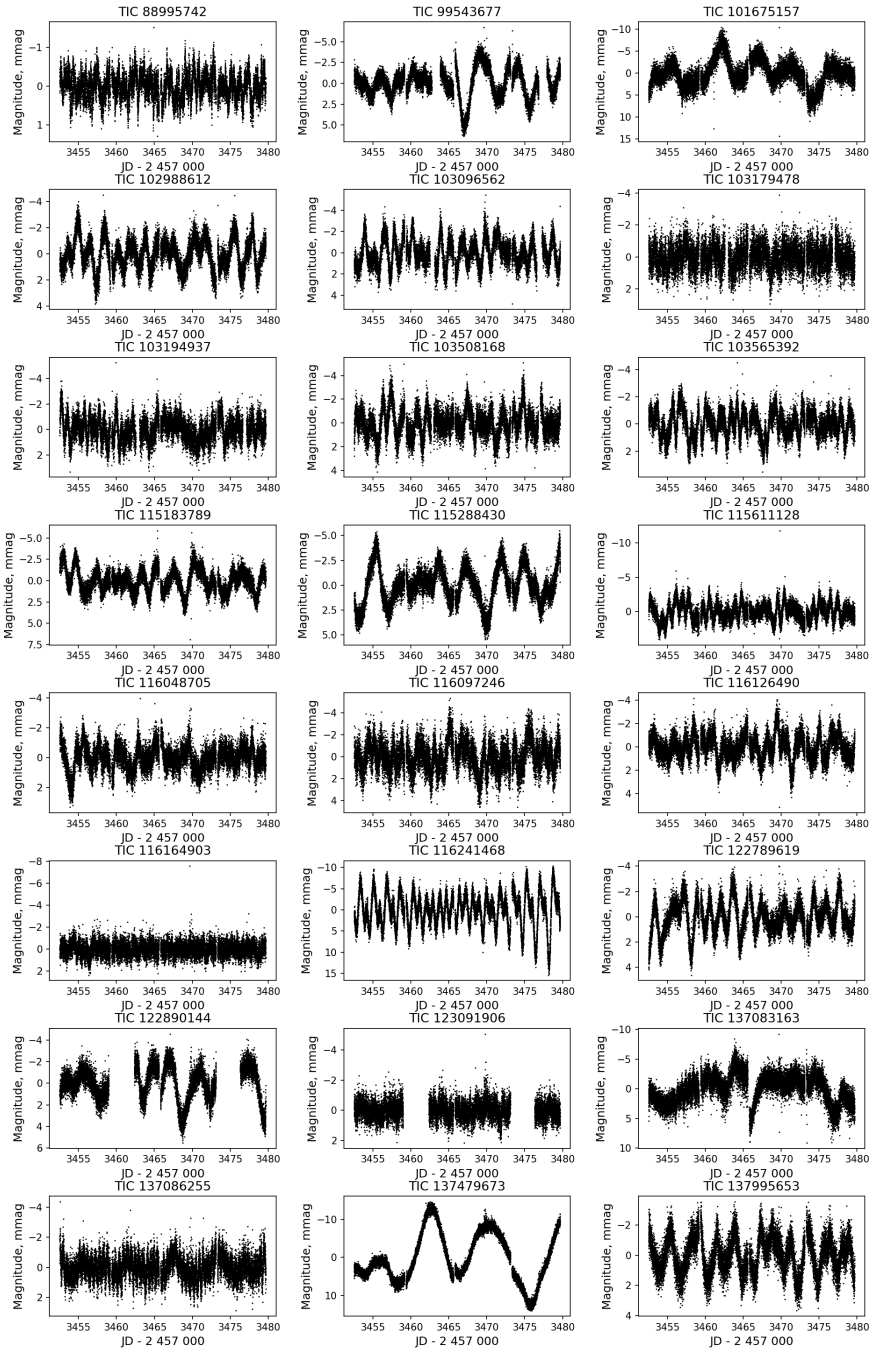

Figure 18. Grid of light curves for objects 49–72. Continued.

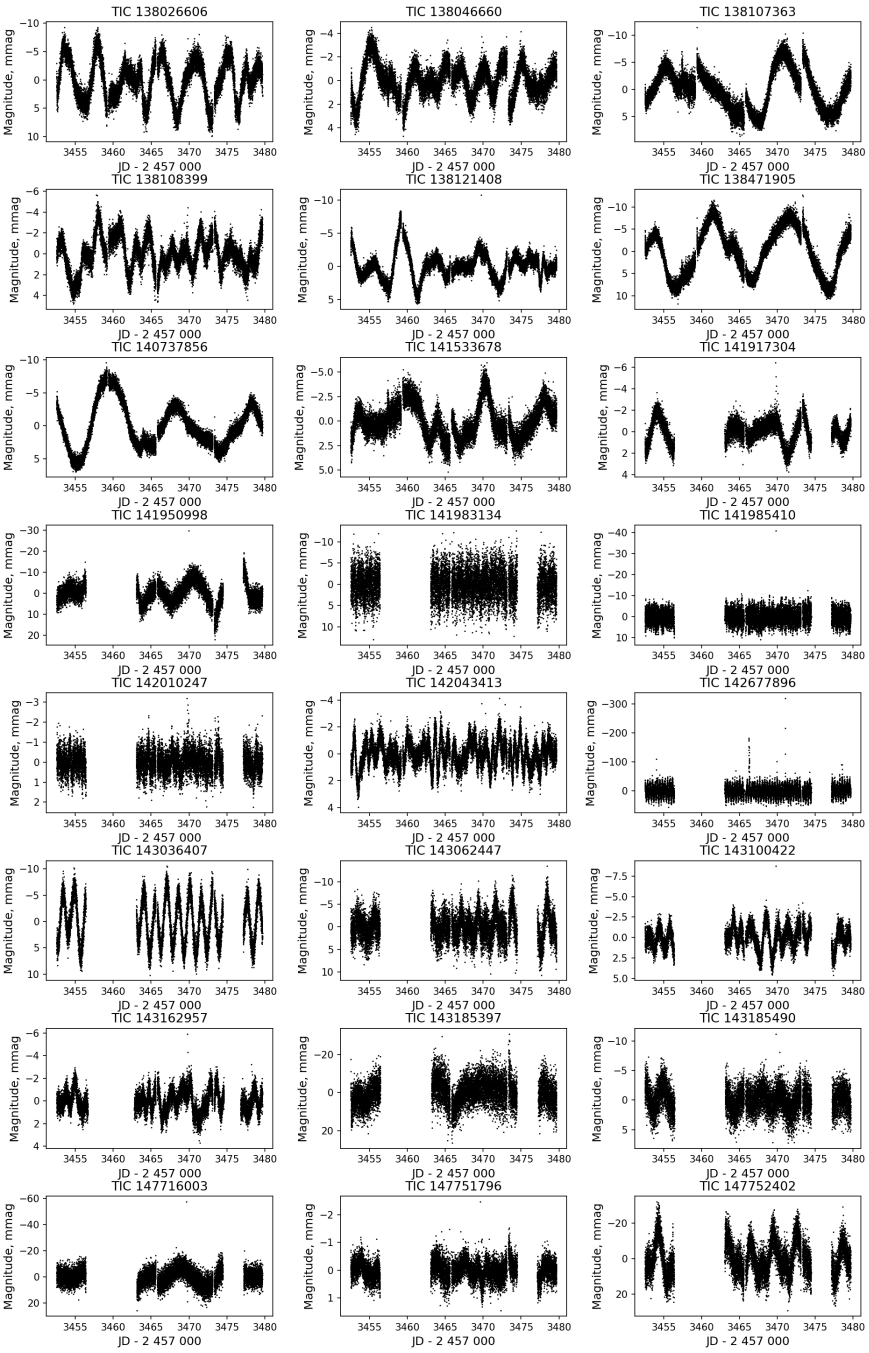

Figure 19. Grid of light curves for objects 73–96. Continued.

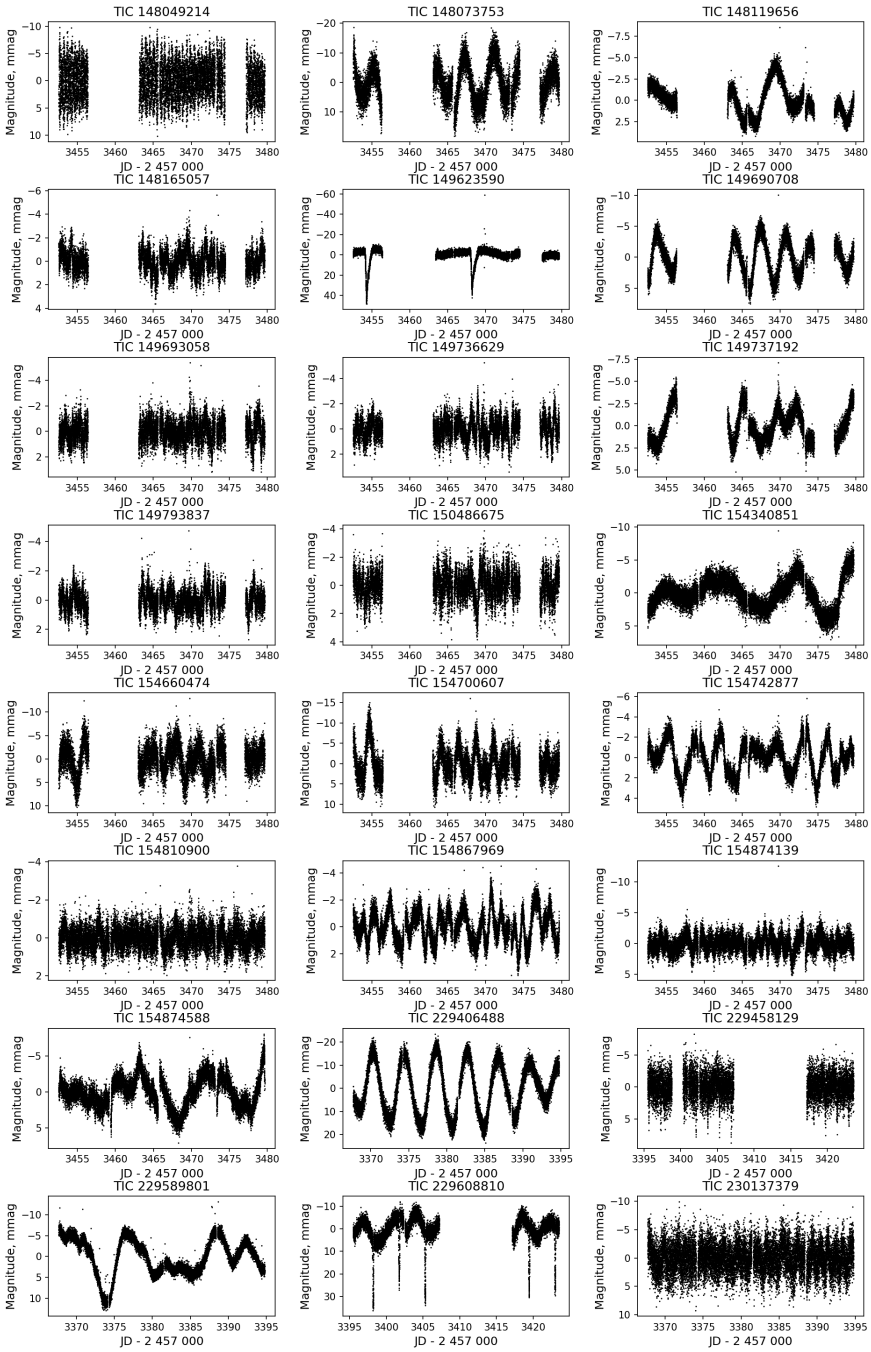

Figure 20. Grid of light curves for objects 97–120. Continued.

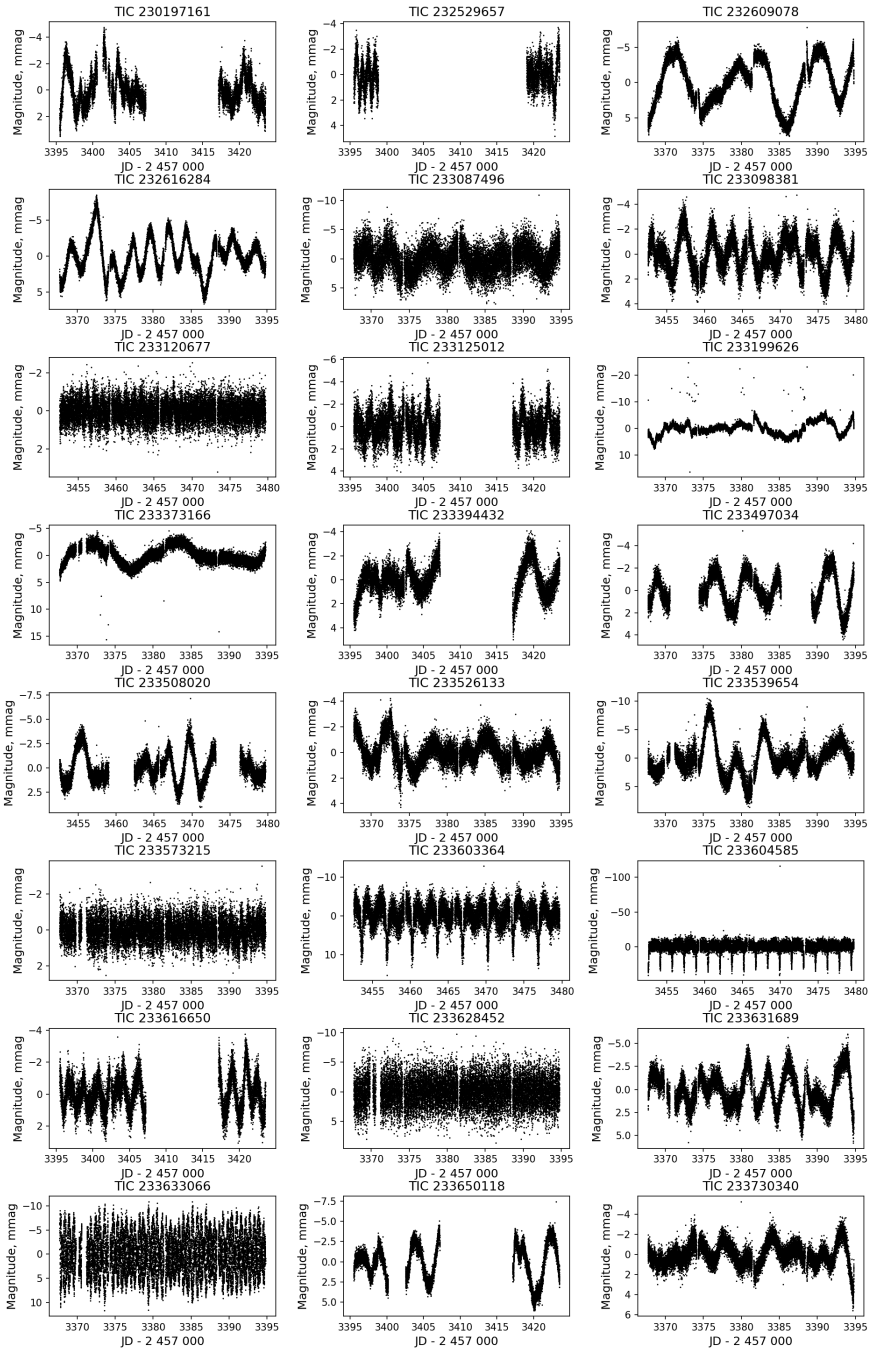

Figure 21. Grid of light curves for objects 121–144. Continued.

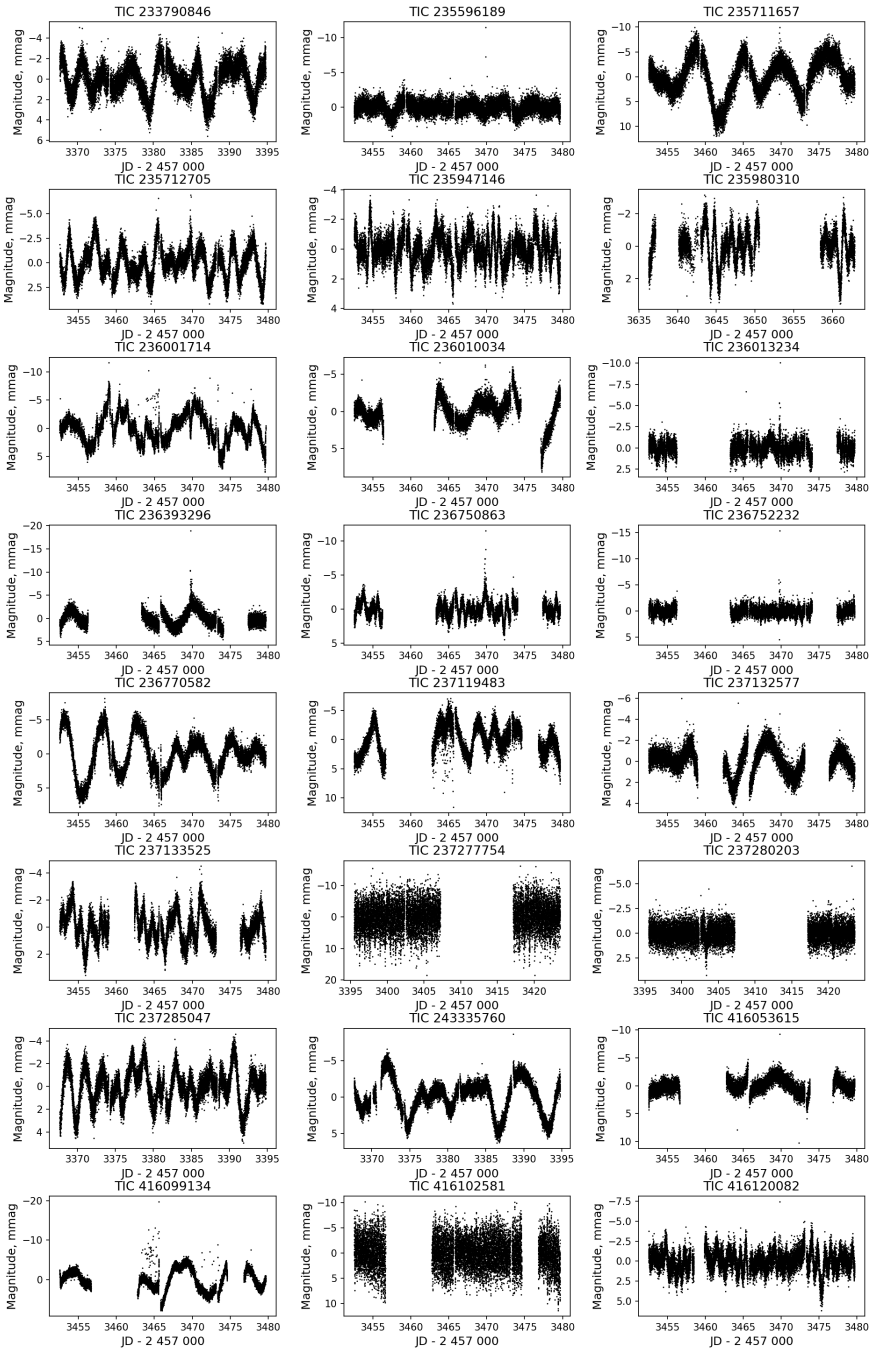

Figure 22. Grid of light curves for objects 145–168. Continued.

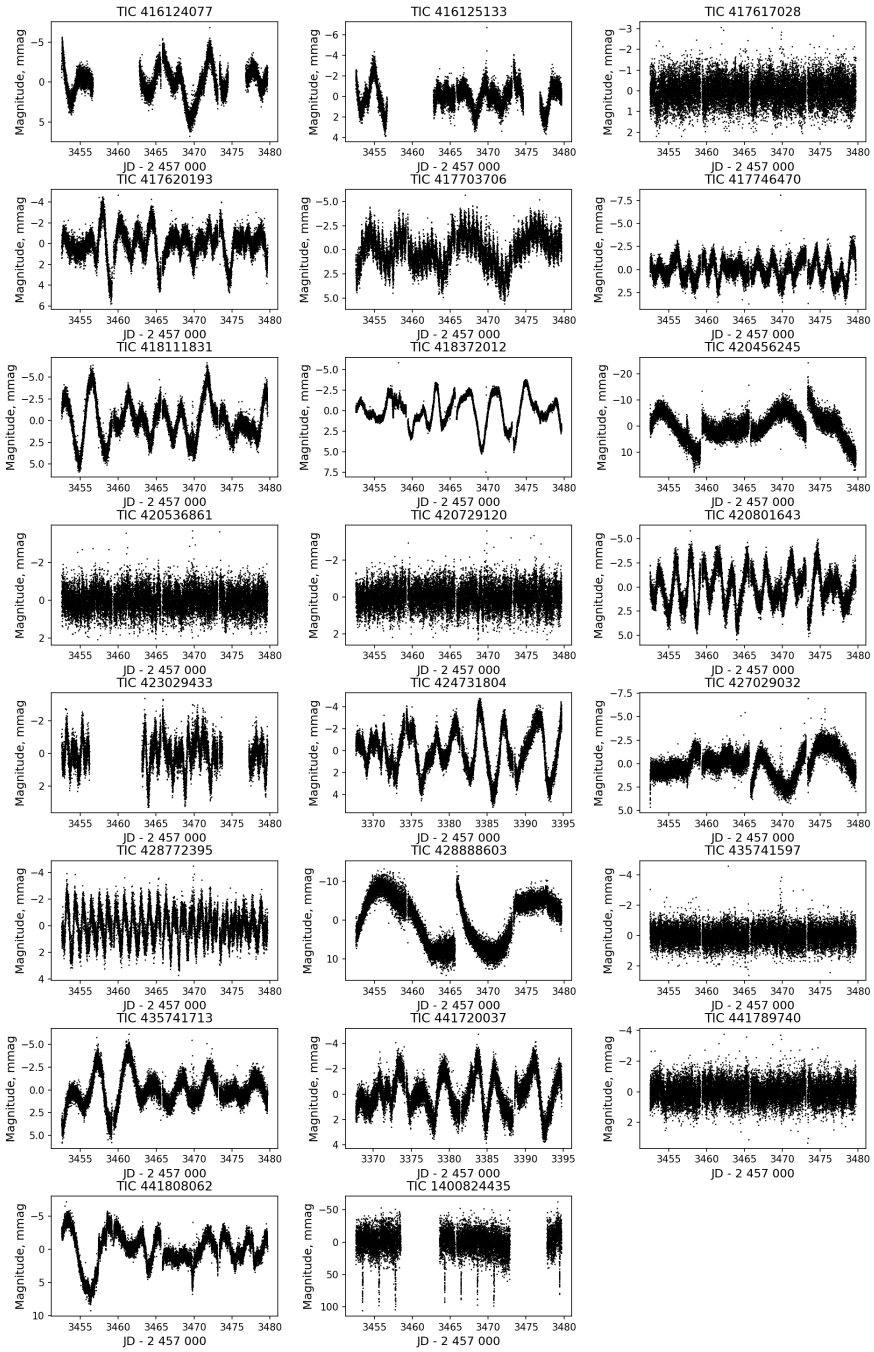

Figure 23. Grid of light curves for objects 169–191. Continued.

PRÁCE ASTRONOMICKÉHO OBSERVATÓRIA
NA SKALNATOM PLESE
LVI, číslo 2

Zostavovateľ:	RNDr. Richard Komžík, CSc.
Vedecký redaktor:	RNDr. Augustín Skopal, DrSc.
Vydal:	Astronomický ústav SAV, Tatranská Lomnica
IČO vydavateľa:	00 166 529
Periodicita:	3-krát ročne
ISSN (on-line verzia):	1336-0337
CODEN:	CAOPF8
Rok vydania:	2026
Počet strán:	82

Contributions of the Astronomical Observatory Skalnaté Pleso are processed using
LaTeX 2ε CAOSP DocumentClass file 3.10 ver. 2024.